Ultracold Thermal Atoms and Bose-Einstein Condensates Interacting with a Single Carbon Nanofiber

Dissertation

zur Erlangung des Grades eines Doktors
der Naturwissenschaften

der Mathematisch-Naturwissenschaftlichen Fakultät
der Eberhard Karls Universität Tübingen

vorgelegt von
Philipp Schneeweiß
aus Potsdam

2011

.

Tag der mündlichen Prüfung:	27. Januar 2011
Dekan:	Prof. Dr. Wolfgang Rosenstiel
1. Berichterstatter:	Prof. Dr. József Fortágh
2. Berichterstatter:	Prof. Dr. Claus Zimmermann

Abstract

The present thesis investigates the decay of ultracold atoms from a magnetic trap due to the interaction with a single carbon nanofiber. The latter is spatially overlapping with the atomic cloud. For both an ultracold thermal cloud and a Bose-Einstein condensate, the atomic loss has been measured for different interaction times and degrees of cloud-nanofiber overlap. Relevant theoretical concepts to analyze the measurements are derived and applied to the experimental results. For the thermal as well as the degenerate gas case, the atom loss is significantly faster than expected from the geometry of the nanofiber. The experimental data is consistent with an enhanced atom loss due to an attractive Casimir-Polder force between the nanofiber and the ultracold atoms. Using a power-law approximation, the Casimir-Polder potential of the nanofiber is quantitatively obtained by fitting the experimental data.

Kurzfassung

In der vorliegenden Arbeit wird der Verlust von ultrakalten Atomen aus einer magnetischen Falle aufgrund von Wechselwirkungen mit einer Kohlenstoff-Nanofaser untersucht. Die Nanofaser wird dabei mit der ultrakalten Wolke räumlich überlappt. Sowohl für eine ultrakalte thermische Wolke als auch für ein Bose-Einstein Kondensat ist der Verlust von Atomen für verschiedene Wechselwirkungszeiten und Überlapp-Parameter gemessen worden. Die relevanten theoretischen Konzepte für die Analyse der Messungen werden hergeleitet und auf die experimentellen Ergebnisse angewendet. Für beide Fälle, d.h. für das ultrakalte thermische Gas und für das Bose-Einstein Kondensat, läuft der Verlust der Atome signifikant schneller ab als aufgrund der Geometrie der Nanofaser erwartet. Die experimentellen Daten sind konsistent mit einem durch attraktive Casimir-Polder Kräfte zwischen Nanofaser und ultrakalten Atomen verstärkten Verlust. Das Casimir-Polder Potential der Nanofaser wurde dabei quantitativ, unter Annahme eines Potenzgesetzes für dessen Verlauf, bestimmt.

Contents

Chapter 1

Introduction

The effect of zero-point fluctuations of the electromagnetic field has many consequences such as the non-relativistic Lamb shift, spontaneous emission, and the anomalous magnetic moment of the electron [Mil94]. Another important vacuum fluctuation effect is dispersion forces whose best known manifestation is the van-der-Waals force, acting between individual atoms (molecules). This thesis presents the first experimental characterization of the dispersive properties of a single nanofiber using ultracold atoms.

Dispersion forces generally give rise to attractive or repulse potentials, acting on neutral atoms, molecules, and macroscopic bodies. The topic has attracted considerable attention in recent experimental and theoretical physics research [Kli09] for at least two reasons: the understanding of dispersion forces touches on the foundations of quantum electrodynamics. Moreover, as dispersion forces become significant for object separations on the order of a few micrometers and below, they are a central effect in several scientific fields, including cell and colloid physics, material science [Par06], and the research and technology of nanoobjects [Bhu04].

Exact measurements of Casimir- and Casimir-Polder (CP) forces[1] are important to test the different dispersion force theories. The first experiments on the Casimir force have been made in the 1950ies [Der57] using a glass plate and spherical lenses. The CP force has been first experimentally investigated by atomic beam deflection experiments in the 1970ies [Shi75]. Measurements were extended and improved by using Rydberg atoms (and their high polarizability) by Anderson et al. [And88]. The first experimental evidence for retardation effects in atom-surface interactions was obtained by Sukenik et al. [Suk93].

The tremendous progress in ultracold atom physics in the recent years has let to further improvements and extensions of high-precision measurements of CP forces. Since the first realization of a Bose-Einstein condensate (BEC) in 1995 [And95, Dav95a], ultracold atom physics in the proximity of surfaces has developed to an important branch within the field. Monitoring the center-of-mass oscillations of a

[1] In the following, these are the forces originating from the dispersive interaction between two macroscopic objects (Casimir force), and atoms and macroscopic objects (Casimir-Polder force). However, there is no unique nomenclature of dispersion force phenomena in the literature.

BEC in the proximity of a surface, the CP force could be measured with unpreceded precision [Har05] and CP temperature effects were demonstrated [Obr07a]. In the intermediate distance range, the CP potential has been measured using a BEC and an evanescent wave [Ben10]. A significant technological improvement in the study of atom-surface interactions has been made by the development of microtraps for atomic ensembles [Vul98, Den98, For98, Den99, M̈99a, Rei99, Ḧ01]. A breakthrough in the field was the creation of a Bose-Einstein condensate in a surface microtrap [Ott01, Hän01], advancing and extending ultracold surface measurements to degenerate gases [For02, Lin04, Wil06].

Since the advent of "atom chips" [Fol02, For07], one major trend in the field is to further miniaturize the atomic traps. The immense progress in the fabrication and research of nanostructures [Wol04] offers great possibilities at the interface between nanoscience and ultracold atom physics. The elaborated techniques of surface ultracold atom physics can, thus, be extended to study nanostructured objects. The interaction of neutral nanoobjects will be dominated by Casimir forces and has certainly to be taken into account when designing micro- and nanosized machines [Boe10].

The present thesis outlines the first measurements of the interaction between an individual, freestanding nanofiber and ultracold atoms. Experimental data has been obtained for both an ultracold thermal cloud and a Bose-Einstein condensate. The atomic ensembles are brought into overlap with a single nanofiber which is standing vertically on a substrate surface. The unpreceded control of the overlap between the ultracold atom cloud and the nanofiber allow to measure the CP potential of a single nanofiber, which, until now, was solely a topic of theoretical investigations.

1.1 Thesis Outline

In the following section (1.2), dispersion force theories as discussed in the literature are presented, compared, and their abilities and limitations are briefly reviewed. In particular, an overview about the Casimir-Polder force models of cylinders and nano-cylinders is given.

The measurements of the nanofiber-cloud interaction have been made with a new experimental setup, integrating established technology for BEC creation with nanotechnologically fabricated samples. In chapter 2, at first (2.1), the principle of magnetic trapping and the manipulation of an ultracold atomic cloud on an atom chip are explain. Then (2.2), the experimental apparatus is described, including details of the vacuum system, the macroscopic trapping electromagnets, the atom carrier chip, and the chip containing the single nanofiber. Furthermore, the laser system is explained, and the major steps of ultracold cloud preparation are outlined (2.3). The deceleration of center-of-mass oscillations of the cloud in the magnetic trap and the absolute positioning of the cloud with respect to the nanostructured surface are discussed in more detail.

The central experimental findings of the present thesis are given in chapter 3 for an ultracold thermal cloud (3.2) and a BEC (3.3). Both sections initially present

time-resolved loss measurements of ultracold atoms from the trap in dependence of interaction time with the nanofiber and the degree of overlap. Then, decay rates of the atomic ensembles are derived and discussed.

In chapter 4, the relevant theoretical concepts to analyze the measurements of the present thesis are given and applied to the experimental data. After the discussion of the CP potential of a nanofiber (4.1), loss mechanisms for magnetically trapped atoms are briefly reviewed (4.2). A model to describe the loss of thermal atoms due to the interaction with an immersed nanofiber is derived in Sec. 4.3 and applied to the respective measurements. In Sec. 4.4, the decay of a BEC due to absorptive interaction with a nanofiber is discussed theoretically and on the basis of the experimental findings. Finally, the results are summarized and reviewed in Sec. 4.5. In the appendix, the adhesion of atoms to the nanofiber and possible consequences for nearby atomic clouds are discussed.

1.2 Dispersion Forces

The van-der-Vaals force between two atoms can be understood in an intuitive picture: vacuum fluctuations lead to the induction of dipole moments in each atom, which are subject to mutual interaction [Pow93]. In case of the CP force, the induced dipole moment in the atom interacts with its image charge inside the macroscopic body. The attraction of two perfectly conducting plates (Casimir effect) can be understood considering the number of field modes in between and outside the two plates. In both cases, this is an infinite number. However, due to the constraints imposed by the plates, the difference of the integrals over all field modes inside and outside this cavity configuration is not zero but finite. The resulting attractive force per unit area is the Casimir force [Mil94].

1.2.1 Concepts

Dispersion forces are generally affected by the following physics:

- system geometry (atom-atom, atom-solid, etc.)
- conductivity of the interacting objects
- temperature (i.e. $T \neq 0\,\mathrm{K}$) of the interacting objects
- temperature of the environment
- temperature differences between the objects (i.e. non-equilibrium situations)
- the medium surrounding the objects
- ground or excited state of atoms/molecules
- retarded / non-retarded regime[2].

The first results on the theoretical description of dispersion forces was obtained by London in 1930. He considered the interaction of two neutral molecules. It was found that for small separations, the respective potential scales as $1/r^6$, with r being the distance between the molecules [Lon30]. Casimir and Polder showed in 1948 that the scaling behavior changes to $1/r^7$ at large separations due to retardation effects [Cas48b]. An extension of the London results from molecules to macroscopic bodies was performed by de Boer [DeB36] and Hamaker [Ham37], in which dispersion forces of point particles were integrated pairwise over the full macroscopic body. This technique is still a common method in colloid physics and referred to as the Hamaker approach [Gu99, Mon00, Par06]. However, experiments as well as macroscopic theories show that the superposition of individual atomic dispersion forces is only correct as long as the macroscopic bodies have a dielectric constant of close to one [Mil94]. In addition, retardation has to be included semi-empirically as, for example, suggested in Ref. [Ana95].

[2]Retardation refers to the finite time $t = s/c$ (c speed of light) for a cause to become effective in a distance s.

The first macroscopic theory of dispersion forces was given by Lifshitz [Lif56]. It correctly describes macroscopic bodies with arbitrary dielectric function, can reproduce retardation effects as discussed by Casimir and Polder [Cas48b], and (in the correct limit) reduces to the early result of Casimir for two perfectly conducting plates [Cas48a]. However, the original Lifshitz theory does not account for partly absorbing media and can have difficulties describing interacting objects at finite temperature [Mil94]. Main extensions and modifications to overcome these limitations have been made by Barash and Ginzburg [Bar75] as well as Schwinger [Sch78]. An extensive overview of generalized Lifshitz theory is given by Klimchitskaya et al. [Kli09]. Modern Lifshitz theory accounts well for many experimental situations. However, it breaks down for non-equilibrium situations. The latter insufficiency and, in special cases, the failure of Lifshitz theory for thermal equilibrium situations, has been studied in more detail by Buhmann and Scheel [Buh08] by means of macroscopic quantum electrodynamics. Such theories describe non-equilibrium situations correctly but require knowledge of the system's Dyadic Green's tensor which calls for a non-trivial calculation even in simple situations. Dispersion forces in the framework of macroscopic quantum electrodynamics are extensively reviewed in Ref. [Sch08].

1.2.2 Casimir-Polder Potential of (Nano)-Cylinders

The scaling behavior of dispersion forces varies strongly depending on the geometry of the interacting objects. For instance, the non-retarded (retarded) van-der-Waals potential between two atoms or molecules scales as $1/r^6$ ($1/r^7$) whereas the non-retarded (retarded) CP potential between an atom and a half space has a distance dependence of $1/d^3$ ($1/d^4$). Universal scaling laws for dispersion interactions are outlined in Ref. [Buh10] and a vast variety of object combinations is discussed in Ref. [Sch08]. A particular proposal on probing quantum-vacuum geometrical effects with cold atoms is given in Ref. [Dal08].

Casimir-Polder Potential of (Nano)-Cylinders

The theoretical investigation of CP forces of cylindrical objects includes a vast number of special cases. The resulting potentials U for an atom in a distance r to the cylinder can differ considerably. The cases considered in the literature include

- (perfectly) conducting and insulating cylinders
- bulk and graphene-like cylinders[3]
- cylindrical shells and full cylinders
- finite and infinite length of the cylinder
- thermal equilibrium and non-equilibrium situations

[3]For distances of the probe atom on the order of the inter-atomic spacing, the cylinder cannot be treated as a bulk material but the atomic lattice structure has to be taken into account.

- retarded and non-retarded regimes.

The first CP force study for a cylinder is done in the 1930ies [Zel35], assuming perfect conductance. This specific case of a perfectly conducting cylinder is under continuous theoretical investigation [DeR81, Gos98] up to the present day [Ebe07, Ebe09, Fin10]. In the non-retarded regime, the theories are consistent with each other. However, Refs. [Bar75, Fin10] showed that the assumption of a perfectly conducting cylinder for CP calculations is, in general, problematic. When retardation effects are included, the limits of large distance and large conductivity are not interchangeable anymore. In the references, it was pointed out that this leads to a contradiction to the central assumption of the model (perfect conductivity of the cylinder).

In addition to this large-distance discrepancy, describing the nanofiber of the present experiment as a perfect conductor is not a suitable model. Studies on the electronic properties of carbon nanotubes show that there can be significant deviation from perfect conductance [Ben95, Koz06, Fag07], which is obvious as semi-conducting nanotubes do exist. In general, dielectric materials can be described by a frequency-dependent tensor $\hat{\varepsilon}$, i.e. accounting individually for different orientations of the electric field [Jac62] in the medium. Moreover, $\hat{\varepsilon}$ can be complex-valued. Then, the real part describes the propagation and the complex part the absorption of electromagnetic waves, respectively. Both parts are inter-related by the Kramers-Kronig relation.

The particular dielectric behavior in the present experimental situation (see Sec. 4.1) makes it questionable to apply the established dispersion force theory of metallic cylinders [Mar82, Bar89, Bou02]. However, these publications can be useful for analyzing the nanofiber when the derivations are kept general and the metallic character of the cylinders is only considered in the choice of $\hat{\varepsilon}$. The dielectric response of the metal is typically described with the hydrodynamical type of dielectric functions [New70, Bou02].

Independent of the applied theory (Lifshitz, macroscopic QED, Hamaker), the particular form of $\hat{\varepsilon}$ only has influence on the CP potential scaling for intermediate and large distances of the atom with respect to the cylinder. For the dispersive interaction of an atom with a cylinder, essentially three distances play a role: the radius of the cylinder R, the distance $d_c = r - R$ between the atom and the cylinder surface, and the main transition wavelengths[4] λ (for ground state ^{87}Rb as used in the present experiment, the two main transitions are at 780 nm and 794 nm).

From the six possible relational combinations of the lengths R, d_c, and λ, only three play a role as it is always $R \ll \lambda$ in the present experiment. This accounts for the particular *nano*cylinder character. No matter which theory is applied, the potential $U(d_c)$ has to resemble a $1/d_c^3$ dependence for $d_c \ll R \ll \lambda$. This is the scaling behavior of the CP potential of an atom in front of a half space in the non-retarded regime [Mil94]. The dependence $U(d_c)$ gets much more complicated for intermediate and large distances between the atom and the nanofiber surface.

[4] In the literature, there is no consensus whether λ or $\lambda/(2\pi)$ is the relevant length scale. However, as the latter only serves to differentiate asymptotic limits, a factor of 2π is not crucial.

In these regimes, the CP potential depends on the interplay between the dielectric properties of the medium, the frequency and temperature dependent polarizability [Buh08] of the atom, the temperature of the cylinder, and the actual atom-surface distance d_c [Ell10]. Obviously, for $d_c \gg \lambda$, retardation has to be taken into account, too.

As outlined in Ref. [Gor06], the non-zero temperature of a dispersively interacting macroscopic body can potentially have three effects: an energetic level shift of the atom due to non-resonant quantum and thermal fluctuations, virtual dipole emission, and virtual dipole absorption. The latter two processes are resonant effects, referring to a coincidence in frequency between thermally excited surface modes of the macroscopic body and main transitions of the atom. However, the two resonant processes can be excluded for the present experimental situation. The virtual dipole emission plays no role as ground state atoms are used. The virtual dipole absorption could play a role but as $hc/\lambda \gg k_b T$ in the present experiment (λ of ^{87}Rb, temperature of the nanofiber $T \approx 300\,\mathrm{K}$), it has no contribution [Fer07].

The atomic level-shift due to non-resonant quantum and thermal fluctuations leads to a modified polarizability of the atom. Thus, finite temperature has to be accounted for by using the thermal instead of the ground state polarizability of the atom [Buh08] – in addition to the consideration of temperature in the common Matsubara sum[5]. However, with λ and T as above, the temperature-related deviation of the atomic polarizability from the ground state result is negligible [Buh08].

As outlined, several theoretical approaches for the description of CP forces are available. System properties like the geometry of the solid state object and its electrical properties have to be taken into account. The CP model which is finally used to describe the nanofiber used in the present experiment is explained in Sec. 4.1.

[5]The Matsubara sum [Kap06] determines the "sampling" of the solid's $\hat{\varepsilon}$ and the atom's polarizability at characteristic, temperature-dependent frequencies. These are the Matsubara frequencies, which are given by $\xi_l = 2\pi k_b T l/\hbar$, $l \in \mathbf{N}$.

Chapter 2

Technical Implementation

The measurement of the scattering of ultracold atoms on a single nanofiber as presented in this thesis have been made with a new experimental setup. The latter is integrating established atom chip technology for BEC creation with nanotechnologically fabricated samples. In this chapter, all relevant steps for the (technical) implementation of the experiment are outlined.

To begin with (Sec. 2.1), the trapping of paramagnetic atoms in magnetic fields is briefly reviewed. Subsequently, the magnetic field configurations relevant for the storage of atomic ensembles in the present experiment are given. In Sec. 2.2, the experimental apparatus developed for the ultracold atom-nanofiber experiment is explained. This includes a discussion of the vacuum system, the macroscopic electromagnets, the atom carrier microchip, the nanostructured chip (including the single nanofiber), and, finally, the laser system. The major steps of ultracold cloud preparation are outlined in Sec. 2.3. The deceleration of center-of-mass oscillations of the cloud in the magnetic trap and the absolute positioning of the cloud with respect to the nanostructured surface are discussed in more detail.

2.1 Magnetic Trapping of Ultracold Atoms

2.1.1 Principle of Magnetic Trapping

The storage of ultracold atomic ensembles in small traps and the precise positioning of these traps with respect to nanostructured surfaces has vast importance for the present experiment.

A suitable technique in this respect is the trapping of paramagnetic atoms in a magnetic field[1] $\vec{B}(\vec{r})$. The finite magnetic moment $\vec{\mu}$ of paramagnetic atoms originates

[1]Following common use, the magnetic induction $\vec{B}$ is referred to as "magnetic field". The relation between the magnetic field $\vec{H}$ and the induction $\vec{B}$ in vacuum is given by $\vec{B} = \mu_0 \vec{H}$, $\mu_0 = 4\pi \times 10^{-7} N/A^2$.

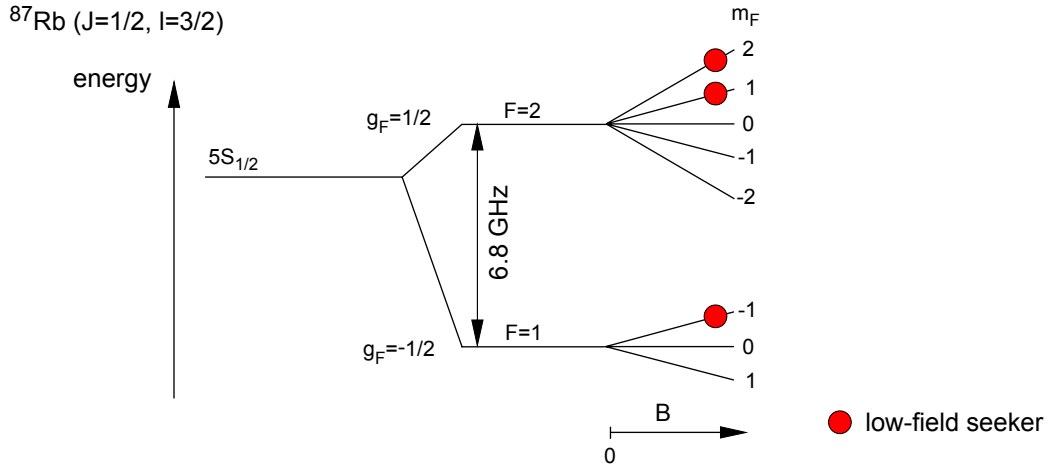

Figure 2.1: Level scheme of the ^{87}Rb ground state. The energetic level $5S_{1/2}$ splits into two levels due to hyperfine coupling of the combined spin-angular momentum $\vec{J} = \vec{S} + \vec{L}$ with the spin of the atomic core $\vec{F}$. The resulting levels $F = 1$ and $F = 2$ experience further energetic splitting in the case of an externally applied magnetic field. Due to the Zeeman effect, the levels associated with the spin projections m_F are modified depending on g_F and m_F.

from the total atomic spin $\vec{F}$ and is given by

$$\vec{\mu}_F = -g_F \frac{\mu_B}{\hbar} \vec{F} \tag{2.1}$$

with g_F the Landé factor, μ_B the Bohr magneton, and $\hbar = h/(2\pi)$ the reduced Planck constant. The total atomic spin $\vec{F}$ is the vector sum of the electron spin $\vec{S}$, the electron angular momentum $\vec{L}$, and the spin of the atomic core $\vec{I}$. In an external magnetic field, paramagnetic atoms are exposed to a potential of the form

$$U = -\vec{\mu}_F \cdot \vec{B}. \tag{2.2}$$

The magnetic moment μ_F can, generally, have positive as well as negative sign. As there cannot be a local maximum of the magnetic field in free space [Win84], magnetic field minima remain to be used as a magnetic trap. Considering Eq. 2.2, μ_F has to have negative sign, such that for a local minimum of the B field, U is a trapping potential.

In addition to a local minimum of the magnetic field and a suitable spin state of the atoms, the adiabacity of the atomic motion in the trap is important to maintain in the trapped spin state. The relevant criterion is [For07]

$$\omega_L \ll \frac{1}{\omega_L} \frac{d\omega_L}{dt}, \quad \omega_L = \frac{g_F \mu_B |\vec{B}|}{\hbar} \tag{2.3}$$

with ω_L being the Larmor frequency. If the inequality in 2.3 holds, the magnetic moments of the atoms can adiabatically adept the direction of atomic precession to the local magnetic field vector in the trap. Then, the magnetic potential can then

be expressed as[2]

$$U = g_F \mu_B m_F |\vec{B}|. \tag{2.4}$$

In combination, the signs of g_F and m_F (the projection of the total spin onto the quantization axis) have to be such that the atoms are low-field seeking, i.e.

$$g_F \cdot m_F > 0. \tag{2.5}$$

The ground state level structure of ^{87}Rb is shown in Fig. 2.1. As visible from the Zeeman-split levels on the right side of the illustration, the suitable spin configurations for trapping are $F = 1, m_F = -1$ as well as $F = 2, m_F = 1$ and $m_F = 2$.

As each atom is moving within the trap, the magnetic field vector at the position of the atom changes. If the magnetic field changes too rapidly, i.e. such that 2.3 is violated, the spin state m_F is no good quantum number anymore and might be changed during atomic motion. Low-field seeking could thus be swapped into high-field seeking atoms and, consequently, would get lost from the trap. These losses are called Majorana losses [Suk97].

For the design of a magnetic trap, 2.3 implies that $|\vec{B}(\vec{r})|$ should be finite and differentiable. As a (counter-)example, the field of two coils operated in anti-Helmholtz configuration produces a spherical quadrupole field which goes to zero in the trap center. At $r = 0$, the derivative of $|\vec{B}(\vec{r})|$ is not defined[3]. This trap shape results in spin flips, in particular, for very cold atomic clouds which characteristically have a high atom occupation around $r = 0$. To prevent these losses, the magnetic field has to be finite in the minimum of the trap. In the present experiment, this offset field in the minimum is, for macroscopic trapping, created by a Ioffe wire [For98]. It is mounted slightly displaced from the center of the transfer coils (see Sec. 2.2.2). On the carrier chip (see Sec. 2.2.3), the transport wires generate a magnetic field component along the linear quadrupole axis, which results in a finite value for the magnetic field modulus along the symmetry axis of the modified quadrupole.

2.1.2 On-Chip Magnetic Waveguide

Two-Wire Trap

The magnetic trap used for the ultracold cloud-nanofiber interaction experiment is formed by a combination of on-chip and macroscopic wires (see Sec. 2.2.3 and 2.3). To estimate the accessible trap parameters, the magnetic fields of two infinitely thin wires separated by a distance d_w are discussed. The situation is sketched in Fig. 2.2 (a).

The field of a wire carrying the current I in the $+z$ direction (out of the plane of

[2]Only the case of moderate magnetic fields is considered (Zeeman case), which is an exact description for all field strengths applied in the experiment.

[3]This is related to the fact that the function $|x|$ is not differentiable at $x = 0$.

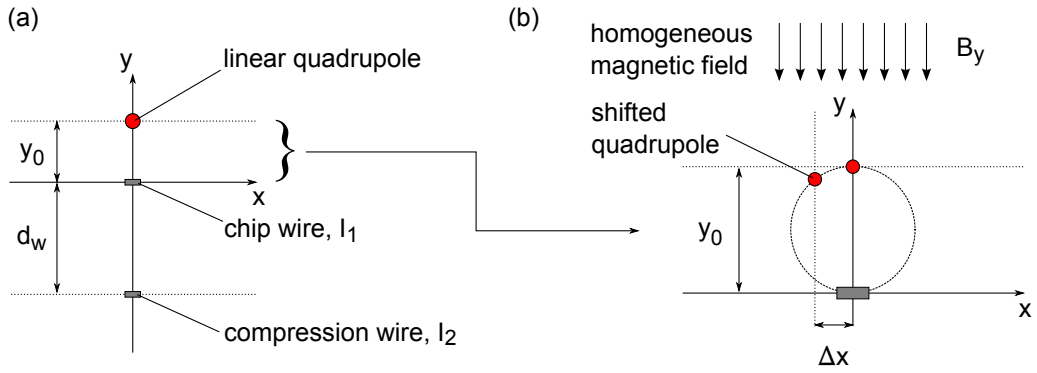

Figure 2.2: Two wires separated by a distance d_w carry the counter-propagating currents I_1 and I_2 (shown in (a)). The resulting magnetic fields provide a linear confinement for low-field-seeking atoms at $(0, y_0)$, which, to first order, can be approximated as a linear magnetic quadrupole. To shift the quadrupole in the x-direction, a homogeneous field is applied in y-direction (b).

paper in Fig. 2.2) is given by

$$\vec{B}(\vec{r}) = \frac{I\mu_0}{2\pi(x^2+y^2)} \begin{pmatrix} -y \\ x \\ 0 \end{pmatrix}. \tag{2.6}$$

With the superposed fields of two wires, a linear confinement for the atoms can be achieved, which, in first-order approximation, has the form of a magnetic linear quadrupole. Using the coordinate system given in Fig. 2.2 (a), a minimum of the magnetic field modulus $|\vec{B}|$ in the x-y-plane can be created at $(0, y_0)$. For two wires separated by d_w with currents I_1 and I_2, the separation y_0 between the minimum and the upper wire in Fig. 2.2 is given by

$$y_0 = -\frac{d_w \cdot I_1}{I_1 + I_2}. \tag{2.7}$$

For the cases $(I_1 > 0, -I_2 > I_1)$ as well as $(I_1 < 0, -I_2 < I_1)$, it follows that $y_0 > 0$. Assuming $(I_1 > 0, -I_2 > I_1)$, the gradient $b = \partial B/\partial r$, $r = \sqrt{x^2+y^2}$ at the minimum of the trap is given by

$$b = \frac{(I_1+I_2)^3\mu_0}{2d_w^2 I_1 I_2 \pi}. \tag{2.8}$$

In the linear magnetic quadrupole as described, atoms are exposed to a potential $U(r) \propto |r|$, i.e. with $U(r=0) = 0$ [For07]. To prevent Majorana losses, an offset field B_{off} is added in the z-direction, transforming the linear quadrupole into a waveguide, suitable to transport atoms. As a consequence of the offset field, the magnetic field modulus at $(0, y_0)$ is not zero but has a finite value B_{off}. Around the minimum of $|\vec{B}(r)|$, the potential for atoms in the waveguide can be approximated to have

harmonic shape. For an atom with the magnetic moment μ and the mass m, the radial[4] oscillation frequency $\omega = 2\pi\nu$ for a motion along the radial direction of the waveguide is given by [For07]

$$\omega = b \cdot \left(\frac{\mu}{m B_{\text{off}}} \right)^{1/2}. \tag{2.9}$$

Some currents and frequencies typical for the present experiment are summarized in Tab. 2.2. As a waveguide is translational symmetric, additional confinement for the atoms in the z-direction is necessary to form a 3D trap. Details concerning axial confinement are outlined in Sec. 2.2.3. The curvature of the potential in the z-direction results in a small correction for the radial trapping frequencies $\omega_{r,0}$, given by [Gün03]

$$\omega_r = \sqrt{\omega_{r,0}^2 - \omega_a^2}. \tag{2.10}$$

For typical axial frequencies ω_a in the experiment, it is on the order of a few percent. In total, the potential for an atom in the on-chip trap can be well approximated as

$$U(x,y,z) = \frac{m}{2} \left(\omega_r^2 (x - x_0)^2 + \omega_r^2 (y - y_0)^2 + \omega_a^2 (z - z_0)^2 \right) \tag{2.11}$$

around the potential minimum at (x_0, y_0, z_0)[5].

Displaced Two-Wire Trap

To let ultracold atoms interact with nanostructures, a full 3D positioning of the magnetic trap is necessary. A detailed treatment of the navigation of the ultracold cloud in the proximity of the nanostructures is given in Ref. [Gie10]. The displacement of the trap in the x-direction (see Fig. 2.2 (b)) is achieved by a bias field perpendicular to the wires forming the waveguide. Its effect is largest, when it is parallel to the y-direction in Fig. 2.2 (b) and there is zero trap shift in the x-direction for a field parallel to the x-axis. For small displacements in x-direction ($\Delta x \ll y_0$), the trap shift by a homogeneous magnetic field $B_y \cdot (0, -1, 0)$ parallel to the y-direction is described by [Gün03]

$$\Delta x = -\frac{B_y}{b}. \tag{2.12}$$

The field configurations described in this section allow the realization of magnetic atom traps as required for the ultracold atom-nanofiber interaction experiment. By adjusting the currents in the relevant wires, the position of the trap as well as the trap frequencies can be tailor-made to the experimental needs.

[4]For this and the following chapters, the term *radial* refers to quantities connected to the plane which is perpendicular to the waveguide wire axes. Quantities connected to the direction parallel to the waveguide wires (here z) are denoted as *axial*.

[5]For the discussed example, it is $x_0 = 0$, y_0 is given by Eq. 2.7, and z_0 is not defined.

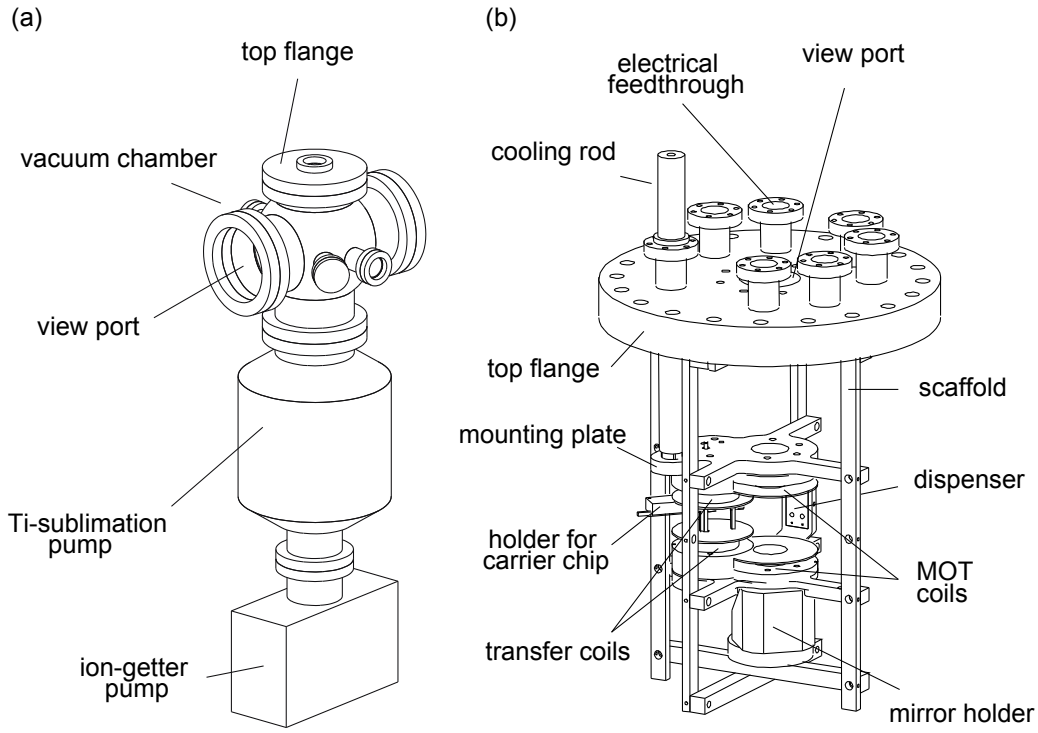

Figure 2.3: Overview of the vacuum system (a) and vacuum chamber interior (b). The main vacuum chamber has several flanges to connect feed throughs, windows, and pumps. To achieve UHV, all flanges are in CF technology. The figure has been reproduced from Ref. [For03a].

2.2 Setup

The purpose of the experimental apparatus is to facilitate the investigation of ultracold atomic ensembles in the proximity of nanometer-structured objects. A high degree of control of the atomic cloud's position with respect to the nanostructures is important for all measurements. To create the ultracold clouds, an ultra-high vacuum (UHV) chamber with very specific in-vacuum setup is needed. As source for the atoms serves a dispenser[6], providing atomic Rubidium. For atom trapping, cooling, manipulation, and detection, several lasers as well as coils and (microscopic) wires are needed.

2.2.1 Vacuum System

To minimize (background) gas collisions which result in heating and atom loss from the trap, ultracold atomic clouds and BECs have to be handled under UHV conditions inside a vacuum chamber. The maximum allowed background gas pressure depends on how long the ultracold ensemble is exposed to background gas collisions.

[6]Model RB/NF/3.4/12 FT10+ 10, SAES Getters, Lainate, Italy.

This, in turn, depends on the time required for cloud preparation, transport, and the actual time for measuring effects on the atoms. In the present experiment, the clouds are exposed for more than 60 s between the initial atom capture in the MOT and the cloud detection. For these exposure times, the background gas pressure in the chamber has to be typically in the low 10^{-11} mbar range or below for atom losses to be negligible.

To reach UHV pressures, a careful choice of materials in the chamber as well as suitable pumping technology is necessary. A schematic drawing of the vacuum system is shown in Fig. 2.3 (a). The central stainless steel vacuum chamber has several CF flanges to connect thermal and electrical feed throughs (CF16), windows, pumps, and pressure gauges. The top flange (CF160) carries the macroscopic trapping coils and wires, the dispensers, a cooling rod, a mirror holder, and the atom chip (Fig. 2.3 (b)). The windows of the chamber have an anti-reflection coating at 780 nm, which is the approximate operation wavelength of all applied lasers of the experiment.

All parts of the vacuum chamber interior are made of low-outgasing materials to facilitate creating an UHV. Before the assembly, the parts are cleaned in an ultrasonic bath, consecutively with three different cleaning solutions. The first step of cleaning involves 15 min ultra-sonic bath in Tickopur detergent[7]. Then, the parts are cleaned for 15 min in acetone and an additional 15 min in isopropyl. Using powder-free latex gloves, the parts are assembled and mounted at the top flange of the chamber. This careful handling minimizes the contamination of the parts with substances from the human skin.

After the completion of the assembly, the chamber is closed, wrapped with aluminum foil, and heated up to 200 °C. While heating, the chamber is first evacuated with a pre-pump[8] and then additionally with a turbo-molecular pump[9]. At around 5×10^{-6} mbar, an ion-getter pump[10] (see Fig. 2.3 (a)) is switched on to increase the total pumping power. In the following days, the dispenser sources, the rods of the titanium pump, and the pressure gauge[11] are cleaned by applying high currents several times.

After six days, the chamber temperature is lowered over one day to room temperature, and the turbo-molecular pump is disconnected from the chamber with an UHV valve at around 1×10^{-9} mbar. The body of the titanium sublimation pump is filled with liquid nitrogen to maximize its pumping efficiency. The titanium rods are then operated several times at $40 - 60$ A for up to 60 s. The operation of the rods is repeated several times per week, yielding pressures in the low 10^{-11} mbar range. The pressure in the chamber improves with every month. For the present experiments, the vacuum in the liquid nitrogen cooled, passive chamber (i.e. without dispenser sources or wires switched on) is measured to be 1×10^{-12} mbar, which is the lower sensitivity limit of the pressure gauge.

[7]Tickopur RW 77, Dr. H. Stamm, Berlin, Germany.
[8]Duo Line, Pfeiffer Vacuum, Asslar, Germany.
[9]TMU 071 P, Pfeiffer Vacuum, Asslar, Germany.
[10]Starcell VacIon Plus 75, Varian, Darmstadt, Germany.
[11]Sensor IE 514 connected to Ionivac IM520, Oerlikon Leybold Vacuum, Köln, Germany.

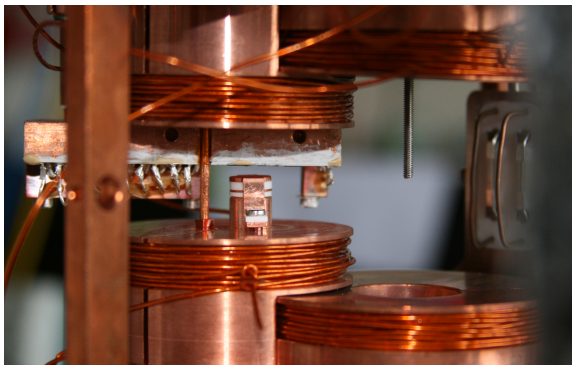

Figure 2.4: Photograph showing the MOT coils, transfer coils, the dispensers, the fully contacted chip on the respective holder, the Ioffe wire, and parts of the scaffold. For a technical drawing, see Fig. 2.3. The ion detector, mounted on the lower transfer coil, is operational but not used in the present experiment. The alignment tool, hanging from the upper MOT coil, is removed before the final assembly.

In operation, the pressure rises up to 1×10^{-11} mbar due to (intentional) outgasing of the ^{87}Rb dispensers and possible outgasing from the current carrying wires due to ohmic heating. A lifetime measurement with a 100 μK cold cloud in the spherical quadrupole trap formed by the MOT coils revealed that 80% of the initial atom number is still in the trap after 50 s of hold time. This is sufficient for the present experiment.

2.2.2 Macroscopic Electromagnets

Most holding constructions as well as the macroscopic linear wires and coils are made of oxygen-free high conductivity (OFHC) copper, which shows very low outgasing. The wires for the MOT and the transfer coils are Kapton- insulated[12] copper wires. Electrically insulating mounting constructions are made of Macor[13], a special UHV ceramic.

A detailed technical drawing of the chamber interior is depicted in Fig. 2.3 (b). A scaffold of four vertical copper bars is connected to the top flange of the vacuum chamber. This construction holds an upper and a lower mounting plate in place as well as two additional crossed copper bars at the bottom of the scaffold. The mounting plates carry the dispenser holder, the MOT- and the transfer coils, the Ioffe wire, and the atom chip holder. Besides the windings necessary to create the magnetic trapping fields, the transfer coils carry additional five windings of thin Kapton wire, serving as radio-frequency (RF) antenna for evaporative cooling. The two crossed bars at the bottom of the construction hold a mirror, which reflects the vertical MOT beams.

The upper mounting plate is connected to a 15 mm diameter copper rod, which leads out of the vacuum chamber. It thermally couples all ohmic heaters (coils,

[12]Wire model KAP2, MDC Vacuum Limited, Sussex, United Kingdom.
[13]Macor Machineable Glass Ceramic, Goodfellow, Bad Nauheim, Germany.

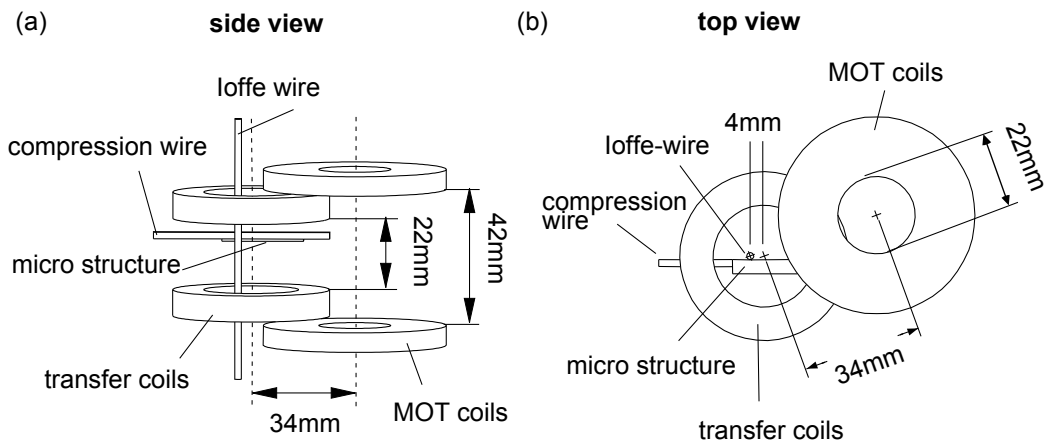

Figure 2.5: Schematic side- (a) and bottom view (b) of the macroscopic trapping electromagnets. Only the currents carrying parts and their respective measures are shown. The optical access is slightly different, due to the finite thickness of the holding constructions. The figure has been reproduced from Ref. [For03a].

linear conductors, dispensers) to a cooling system outside the chamber. A heat management for the electromagnets is important for three reasons: First, an ever increasing temperature of the conductors would encourage outgasing of the wires and lead to a worse vacuum. Second, the resistance of normal conductors increases with temperature. If the current in the wire is kept constant, a higher voltage has to be applied, leading to even stronger ohmic heating. Ultimately, wires can burn, which is a particular danger for the thin chip wires. The third aspect of heat management concerns thermal expansion of the parts in the vacuum chamber. In the present experiment, atoms are positioned in the proximity of (nanostructured) surfaces with a position uncertainty of less than $1\,\mu$m. As the thermal expansion coefficient of copper is $16.5\,\mu\mathrm{m}/(\mathrm{m}\cdot\mathrm{K})$ and the expanding parts have a length on the order of 10 cm, the temperature of the holding constructions should change less than 1 K during the experiment.

This is achieved by a constant cooling via the cooling rod and a long warm-up time (approximately 12 h) of the setup before the measurements. The cooling is provided by a Peltier element[14] which is mounted at the upper end of the rod, constantly operated with 5 A, and cooled with a permanent water flow at 10 °C. A sensor at the top of the cooling rod allows to monitor temperature changes and indicates when the system is in thermal equilibrium. After a sufficient warm-up time of the setup, the sensor shows temperature changes not more than 1 °C.

The particular geometry of the electromagnets in the chamber is shown schematically in Fig. 2.5. The drawings and measurements refer to the current carrying parts only, i.e. the only parts relevant for the calculation of the accessible magnetic field configurations. To estimate optical access and thermal properties of the system, the finite thickness of the wire holders has to be taken into account. A photograph

[14]QC-127-1.4-8.5MD, Conrad, Hirschau, Germany.

	MOT coils	transfer coils
inner diameter [mm]	22	31
outer diameter [mm]	56	48
thickness [mm]	6	8
free distance between coils [mm]	42	22
number of windings per coil	130	80
conductor cross section [mm]	0.6	0.6
resistance [Ohm]	1.2	0.8
axial gradient [G /(cm·A)]	15	19.3
maximal continuous current [A]	3	3

Table 2.1: Characteristics of the MOT and transfer coils. The given measures refer to the current carrying parts (not holders), allowing the calculation of accessible magnetic field configurations.

of the macroscopic electromagnets used in the experiment is shown in Fig. 2.4. The technical details of the coils are summarized in Tab. 2.1. In addition to the in-vacuum coils, the chamber is equipped with, in total, four macroscopic coils mounted on the view ports which provide the optical access in the horizontal plane. These electromagnets typically serve to apply an offset to the fields generated with the coils from inside the chamber.

The design of the MOT coils is restricted by three main criteria: sufficient optical access for MOT laser beams, sufficient magnetic gradients, and the option to further transfer trapped atoms to other magnetic traps. The latter is achieved in combination with the transfer coils. Their symmetry axis is shifted by 34 mm with respect to the axis of the MOT coils. In particular, the coil arrangement is chosen such that atoms stored in the field of the transfer coils are not in the path of the MOT laser beams anymore.

This allows the additional installation of holders and electromagnets. In the present experiment, a Ioffe wire and the holder for the atom chip are built between the transfer coils. The Ioffe wire is shifted by 4 mm from the transfer coil's symmetry axis, measured from the center of the wire. Its diameter is 1.5 mm and the operation current is up to 15 A. The wire is made of OFHC copper and has no insulating Kapton layer. It is fixed in the chamber with Macor holders. The purpose of the Ioffe wire is twofold: First, to create a trap with non-zero magnetic field modulus at the trap minimum to prevent Majorana losses [Suk97] (see also Sec. 2.1). Second, to shift the atoms from the symmetry axis of the transfer coils towards the atom chip, to enable the handover of the atoms to the on-chip traps.

2.2.3 Carrier Chip

The carrier chip is one of the key elements in the present experiment. Paramagnetic atoms like ^{87}Rb can be stored in magnetic fields as outlined in Sec. 2.1. As the field-

generating conductors on a chip are manufactured lithographically, their layout can be controlled with an accuracy better than 1 μm. In combination with stable, low noise current drivers[15], magnetic traps can be, in principle, created with a position uncertainty lower than 10 nm [Hom05].

An atom chip with full 3D cloud positioning capability has been introduced and fully characterized in Ref. [Gün03], and is used in the present experiment. The layout of this chip is shown in Fig. 2.6. Gold wires are lithographically created on both sides of a 250 μm thick substrate of aluminum oxide. A layer of a few nanometers of a tungsten titanium alloy serves as the adhesion agent between the chip surface and the gold wires. The upper side carries the so-called quadrupole wires (QP1-QP3), which are used to create a radial confinement for the atoms (for the definition of radial and axial direction, see Sec. 2.1.2). They are 100 μm wide, have a height of 6 μm, and their mutual distance between the wire centers is 750 μm. The maximally applicable current is about 1 A for 15 s.

The back side of the carrier chip has a set of wires (T1 to T8), which are perpendicular to the quadrupole wires. These so-called transport wires allow the positioning of the cloud in the axial direction, and provide axial confinement. The spacing between two mutual wires is 650 μm (center to center), the lateral dimensions are the same as for the wires on the top side of the chip. However, the maximally applicable current is lower than for the quadrupole wires as the transport wires are much longer. In the present experiment, the current in the transport wires never exceeds 0.6 A.

The radial confinement of the atoms is achieved using QP2 (see Fig. 2.6) as in Ref. [Gün03]. However, in contrast to the reference, the wires QP1 and QP3 are not used. Instead, the central chip wire QP2 is operated in combination with a 2 mm $\times$ 2 mm compression wire, leading to higher trap frequencies. The latter massive OFHC copper wire has a quadratic cross section, is glued below the chip, oriented parallel to QP2, and its center is vertically displaced by $d_w = 1.87$ mm with respect to the center of QP2. The value for d_w is a result of a measurement of trap frequencies and offset fields for different currents in the compression and the QP2 wire. Some typical currents and respective trap parameters as used in the experiment are summarized in Tab. 2.2.

With the help of the transport wires, the cloud is confined axially and experiences a non-zero offset field in the trap center. The trapping wires are always operated as one or two sets of two wires. For example, in Fig. 2.6 (b), the loading position for atoms from the Ioffe trap is marked with a black circle. It is axially located above T3 and exactly above QP2 in terms of radial position. The trap at this axial position is created by a current of the same magnitude and direction flowing in the wires T1 and T5. To shift the cloud towards an axial position above T4, the current in the T1 and T5 wires is lowered and, at the same time, the current in the T2 and T6 wires is increased. The currents in the wires T1/T5 and T2/T6 are ramped such, that the offset field (and consequently the trap frequencies) stays constant.

Limited by the ohmic heating of the transport wires, the maximum operated current

[15] In this experiment, models BCS 1/20, 3/12, 3/15, 5/12, 10/4, and 15/2 by Highfinesse, Tübingen, Germany.

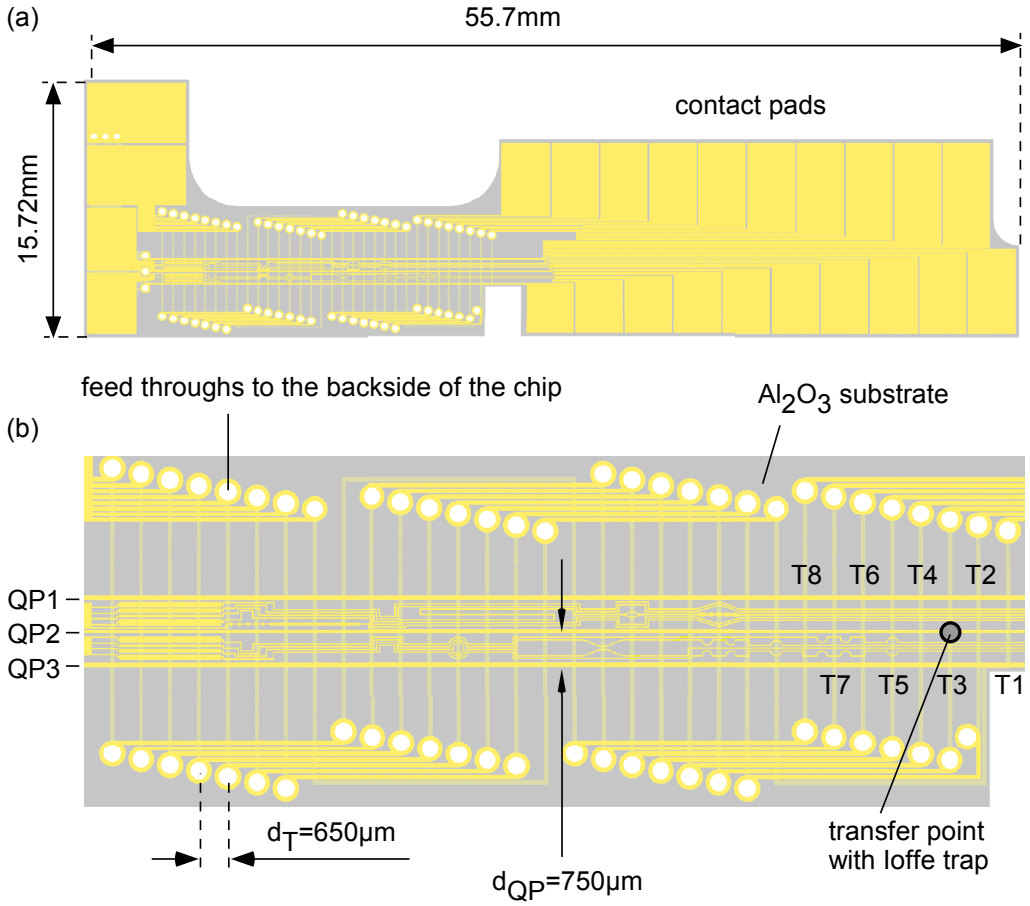

Figure 2.6: Layout of the complete carrier chip (a) and close-up of the wire geometry relevant for generating the trapping fields (b). As visible in (a), the complete chip extends several centimeters, mainly due to the space needed for the contact pads. It is designed in two layers, the upper layers carries the quadrupole wires (QP1 - QP3), the contact pads, and parts of the transport wires. The lower side contains the essential sections of the transport wires (T1 - T8), which, in the figure, run vertically. These sets of wires are shown in detail in (b), the wires on the chip top side in bold yellow and on the bottom side in light yellow. The complex routing of the transport wires is to avoid crossing with other wires, which would otherwise lead to a short circuit. The figure has been reproduced from Ref. [Gün03].

stage on the chip	$I_c[A]$	$I_{QP2}[A]$	$b[G/cm]$	$\nu_r[Hz]$	$y_0[\mu m]$
initial transport	5.4	-0.9	104.1	131.8	380
main cooling	5.4	-0.5	241.9	308.0	194
over the nanochip	2.62	-0.4	58.0	72.2	342

Table 2.2: Typical currents I_c and I_{QP2} in the compression and the central quadrupole wire as well as resulting trap parameters. The gradients b are deduced from a measurement, the corresponding trap position y_0 above the carrier surface as well as the radial trap frequencies ν_r at $B_{\text{off}} = 1\,\text{G}$ are calculated according to Sec. 2.1.2. The reduction of the radial frequency due to an axial gradient from the transport wires is taken into account with $\nu_a = 16\,\text{Hz}$.

in these conductors is 0.6 A. This results in an offset field of approximately 0.66 G at the minimum of the trap. To minimize Majorana losses, this field is increased with the help of the coils mounted outside the vacuum chamber to approximately 1 G. The axial confinement created by the transport wires results in an axial trapping frequency of 16 Hz, which is a typical value in the entire experiment.

2.2.4 Nanostructured Chip

From the virtually infinite number of available types of nanostructures [Bhu04], vertically aligned multi-wall nanofibers made of carbon have been chosen for the present experiment. These structures are comparatively easy to fabricate and offer good spatial access for the atoms as they protrude several micrometers away from the substrate. The subsequent section discusses the fabrication process of the nanofibers, followed by a characterization of the structures. Then, the integration of the nanostructured chip with the experiment is explained.

Fabrication of Nanofibers

The fabrication of the nanofibers is done in two steps, first, the patterning of a substrate with catalyst material for the nanofiber growth and second, the actual growth process. The production closely follows the lines of Refs. [Ren99, Mer00] and was realized in the group of Prof. D. Kern, Institute of Applied Physics, University of Tübingen. The chips have been fabricated by G. Visanescu. The production process as well as the characterization of the structures are discussed in detail in Ref. [Vis10].

To begin with, a 250 μm thick substrate of silicon is thermally oxidized at 1050 °C (see Fig. 2.7 (a)). After 20 min, a 7.4 nm oxide layer covers the substrate. The latter is coated with a 2.5% concentration of polymethyl methacrylate (PMMA) photo resist by spin coating. An electron beam lithography system allows patterning the prepared substrate with nanometer resolution. Three different structures are written on the chip, a 0.5 mm × 1.5 mm *carpet* of nanofibes, a 1 mm × 1.5 mm array of periodic lines, and a 1.25 mm × 0.5 mm structure containing single, freestanding nanofibers. For details of the written structures, see Sec. 2.2.4. All patterns are written as an

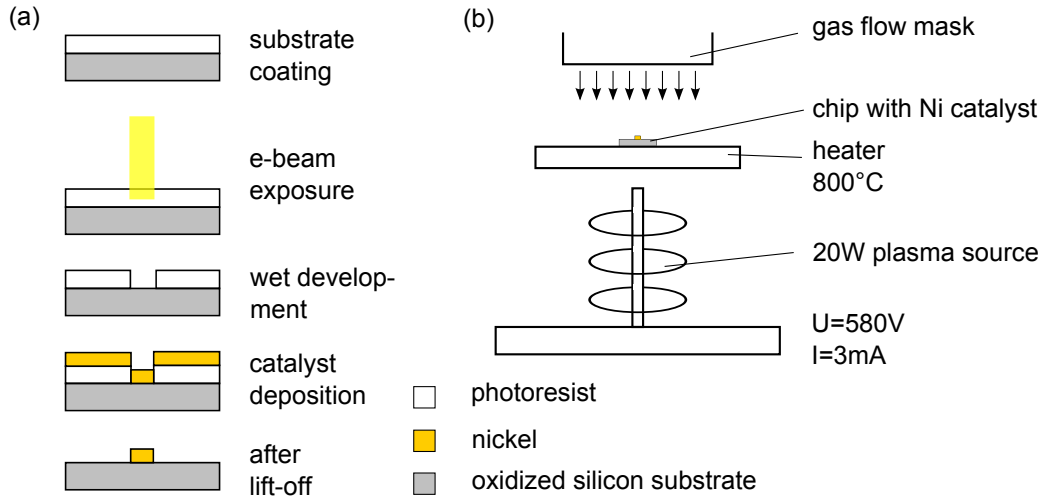

Figure 2.7: Steps of sample preparation (a) and sketch of the PECVD system for the nanofiber growth (b). A silicon substrate is oxidized and coated with photo resist. An electron beam lithography system allows patterning of the substrate with nanometer resolution. After the development of the sample, a nickel layer is deposited. A lift-off step leaves only the patterned nickel dots on the sample, the latter catalyzing nanofiber growth. For the actual growth process, the sample is heated and subjected to a plasma-enhanced flow of acetylene and ammonia.

array of 180 ± 20 nm diameter dots, which are seperated 250 nm $\times$ 250 nm in the case of the carpet and 250 nm $\times$ 4 μm for the nanofiber lines (measured center to center).

After developing the sample with a mixture of methyl isobutyl ketone (MIBK) and isopropanol (IPA), a 3.6 nm nickel layer is sputtered on the chip. This material acts as a catalyst for the nanofiber growth. After lifting off the remaining PMMA with acetone, only the nickel dots remain. They define the position of nanofiber growth. The diameter of the dots influences the diameter of the nanofiber.

The nanofibers are grown by plasma-enhanced chemical vapor deposition (PECVD). A schematic drawing of the PECVD system[16] is shown in Fig. 2.7 (b). The nano-patterned chip is mounted on a heater, which is operated at 800 °C. For 35 min, a gaseous mixture of acetylene (30 sscm[17]) and ammonia (150 sscm) streams towards the chip from the flow mask. A 20 W DC plasma enhances the growth process.

Nickel belongs to the so-called tip growth catalyst materials. During the PECVD process, the nickel dot is raised up with the tip of the nanofiber [Sin99]. The gas flow reduces the size of the catalyst particle until no material is left. Then, the growth process stops and further gas flow leads to a reduction of the nanofiber height. The PECVD process for the nanochips in the present experiment has been adapted such that no nickel is left at the tip of the fiber.

[16]Model Black Magic, Aixtron AG, Herzogenrath, Germany.
[17]standard cubic centimeters per minute.

SEM Characterization of the Nanochip

The nanochip is based on a 3.5 mm × 3.85 mm silicon substrate of 250 μm thickness. These dimensions provide enough space to fabricate many different nanostructures on the chip. An overview of the chip taken with a Scanning Electron Microscope (SEM) is given in Fig. 2.8 (a). The extended nanocarpet and the periodic lines of nanofibers are not further considered.

Single, vertically standing carbon nanofibers are placed within a larger nanostructured area as shown schematically in Fig. 2.8 (e). The position of the nanofiber used for the scattering measurement is marked in red. The carpet-like areas as well as rectangularly arranged lines of nanofibers serve for navigation purposes, to finally localize the single nanofiber with the ultracold atoms. The rectangles surrounding the single nanofibers are 150 μm × 50 μm in size and shown in detail in (b), (f), and (g) in Fig. 2.8. The heights of the fibers in the rectangles varies strongly and is, on average, approximately 10 μm.

The Figs. 2.8 (c) and (d) show a close-up of the nanofiber used for the scattering measurement. The images are taken under a 20° tilt angle, making the fiber appear shorter. It has a height of 10.25 μm, its diameter varies from top to bottom from approximately 40 nm to 275 nm. A complete analysis of the nanofiber diameter, taking into account the finite SEM electron beam diameter and a sub-optimal focus while imaging, is provided in Sec. 3.1.

As visible from the SEM close-up in Fig. 2.8 (d), the nanofiber used for the scattering experiment does not contain any remaining nickel at the tip as anticipated from the etching times in the fabrication process.

2.2.5 Nanochip and Carrier Chip Assembly

Mounting the nanochip onto the carrier chip requires great care. Under an optical microscope (see Fig. 2.9), the nanochip is placed by hand above the QP2 wire. The central thin line of the structure shown in Fig. 2.8 (e) should be parallel to the QP2 wire. The lateral positioning deviation should be as small as possible, such that the structures of interest are still within reach of the magnetic traps created by the carrier chip. As visible from Fig. 2.9, the deviation is at most 50 μm.

To fix the nanochip, the commonly used ceramics glue[18] is not suitable. It is very crumbly which can easily lead to a destruction of the nanostructured surface by loose glue particles. Instead, an electrically insulating UHV epoxy glue[19] is taken for the chip assembly. The nanochip is put flat on the carrier and, after alignment, glue is added from above the chip. Hence, the distance between the two chips is minimized and amounts to at most 15 μm as checked with the microscope. It is important to keep this spacing as small as possible as the magnetic traps get more and more shallow when created further apart from the current-carrying wires. The maximum azimuth angle between QP2 and the symmetry line of the nanochip is 2 °.

[18] Cotronics 920, Polytec PT, Waldbronn, Germany.
[19] Epo-Tek H77, Polytec PT, Waldbronn, Germany.

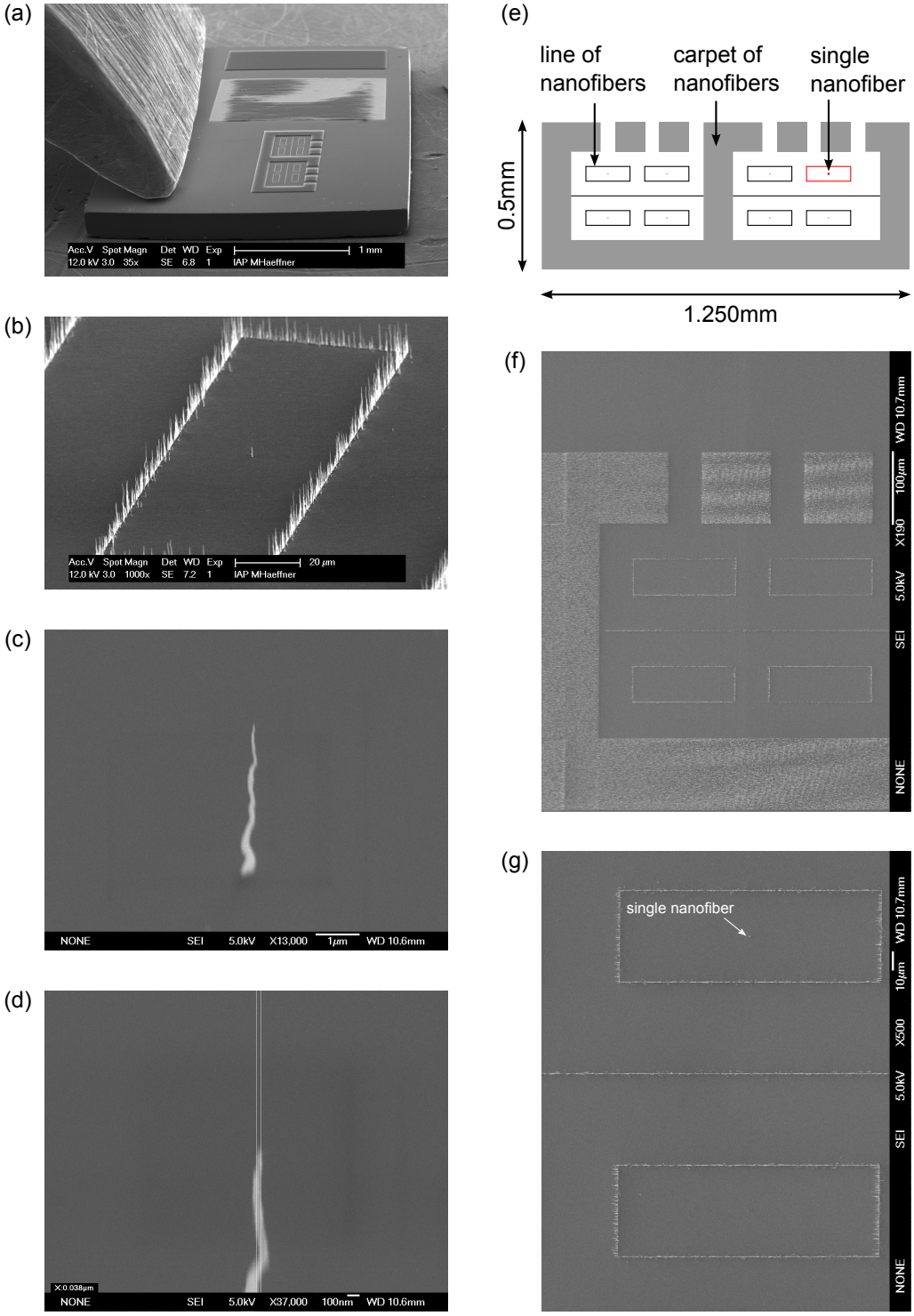

Figure 2.8: SEM images of the nanochip, shown in full in (a). The single nanofibers are surrounded by larger patterns drawn schematically in (e). Subfigures (b), (f), and (g) show the rectangular line structures, centered around the single fibers. Subfigures (c) and (d) provide a close-up of the nanofiber used for scattering.

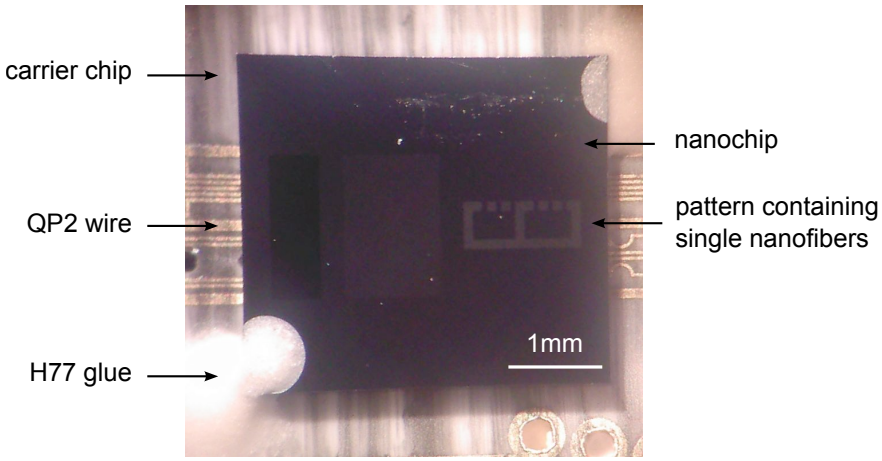

Figure 2.9: The nanochip is centered and fixed above the QP2 wire of the carrier chip. The electrically insulating epoxy glue drops attaching the nanochip (H77) appear in white in the lower left and upper right corner. The amount of glue does not influence the optical access to the chip.

A misalignment is not yet resolved in the ultracold atom-based measurement of the nanochip's topography.

Before the nanochip is mounted onto the carrier, the latter is put on a holder and fixed with H77 glue. Both chips, the holder, the electrical contacting, and the compression wire are shown in Fig. 2.10. The contacting of the carrier chip is solved with a small holder for the Kapton wires close to the contact pads and electrically conducting UHV epoxy glue[20]. On the Kapton wires, the insulation is removed at the tip of the wire and then glued to the contact pad. The advantages of this contacting solution are a high meachnical flexibility of the contacts as well as the absence of any ceramics glue. The non-rigid construction of the contacting is particularly suited to survive the baking of the UHV chamber. However, both epoxy glues have the disadvantage that the need to be baked before they solidify.

2.2.6 Laser System

For ultracold cloud preparation, manipulation, and detection the laser system plays an essential role. To fulfill their tasks, the light of three master lasers[21] has to be frequency-stabilized with MHz accuracy and the (amplified) laser power fluctuations have to be made as small as possible. Furthermore, the light beams have to maintain their polarization and all lasers have to be switchable with microsecond timing.

[20] Epo-Tek H20E, Polytec PT, Waldbronn, Germany.

[21] Two master lasers are home-made grating-stabilized diode lasers [Ric95], using HL7851G diodes by Hitachi, Berkshire, United Kingdom. The cooling light comes from an integrated system including a tapered amplifier, model TA pro by Toptica, Graefelfing, Germany.

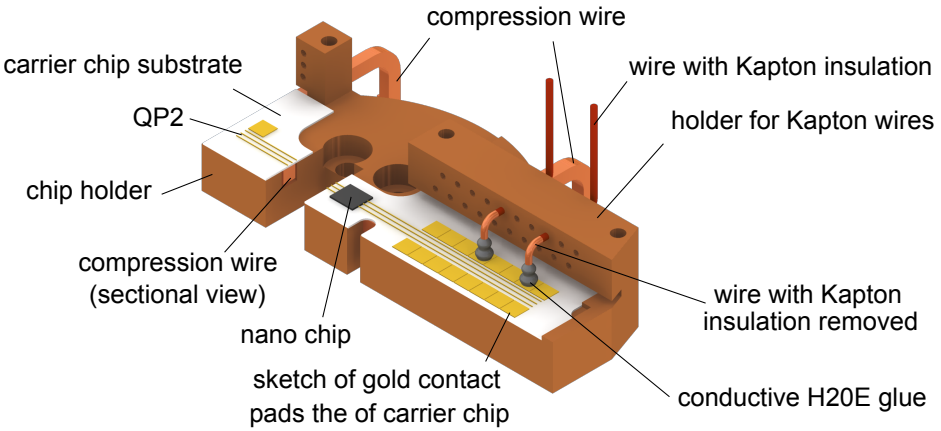

Figure 2.10: The chip holder with compression wire, carrier- and nanochip, and the electrical contacting is shown. For every contact pad, a Kapton wire is plunged through a hole in the wire holder, pruned of its insulation, and connected to the pad with conductive glue.

Lasers and Laser-Stabilization

Different techniques are used to laser cool [Hän75] and trap the ^{87}Rb atoms. After gaseous ^{87}Rb is released from the dispenser, it is captured in a MOT [Raa87]. In terms of lasers, this requires a cooling and a repumping laser. Subsequently, optical molasses are applied to the cloud [Let88, Dal89] followed by a few milliseconds of optical pumping to prepare the atoms for magnetic trapping. After several steps in purely magnetic traps, the cloud is finally detected by resonant absorption imaging. The involved atomic transitions are shown in Fig. 2.11. An in-depth discussion of the experimental cycle including details of the mentioned methods follows in Sec. 2.3.

All optical manipulations of the atoms are realized within the D2-line of ^{87}Rb. The values for the level spacing shown in Fig. 2.11 originate from Ref. [Ste09]. The D2-line is the atomic transition from the $5S_{1/2}$ to the $5P_{3/2}$ level and corresponds to a wavelength of around 780 nm. The reference laser (see also Fig. 2.12) is locked to the $F = 2 \rightarrow F' = 3$ transition by polarization spectroscopy [Wie76]. To know exactly where to lock the laser, a saturation spectroscopy is also connected [Dem03].

While experimenting, a faint but clearly discernible beating is observed on all spectra, including the reference spectrum. The frequency of the beat can be varied by changing the scanning frequency of the function generator driving the piezo element of the laser. The source of the problem is found to be residual 50 Hz power grid noise of the laser drivers[22]. Repeating with 50 Hz, the frequency of the laser light is modulated by at least 1 MHz as measured with a beating of two spectroscopy-locked lasers. Such a frequency deviation is not negligible compared to the width of the hyperfine transitions (≈ 5 MHz) and prevents the setup from having a shot-to-shot atom number fluctuation smaller than 10%. In the present experiment, the 50 Hz problem is solved by supplying the laser driver solely from a large battery. Stimulated by the outlined observations, the manufacturer developed a new version of the

[22]Model LCS 02/6, Highfinesse, Tübingen, Germany.

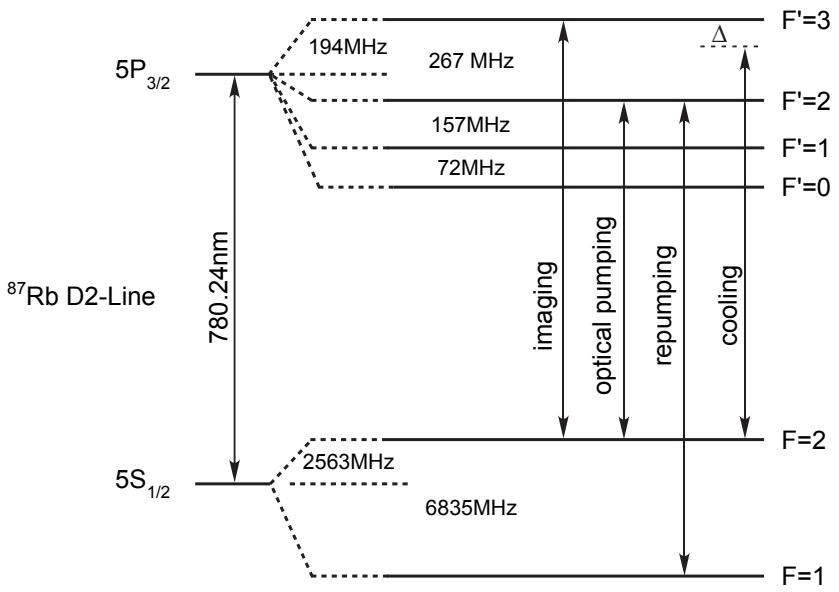

Figure 2.11: All steps of optical manipulation of the ^{87}Rb atoms in the experiment happen within the depicted D2-line. This set of transitions corresponds to wavelengths around $780\,\mathrm{nm}$. Depending on purpose, the lasers are stabilized to different hyperfine transitions or have an adjusted detuning from the resonances. The hyperfine states are denoted with F and F', respectively. The second-strongest transition (D1 line, not shown) is at approximately $794\,\mathrm{nm}$.

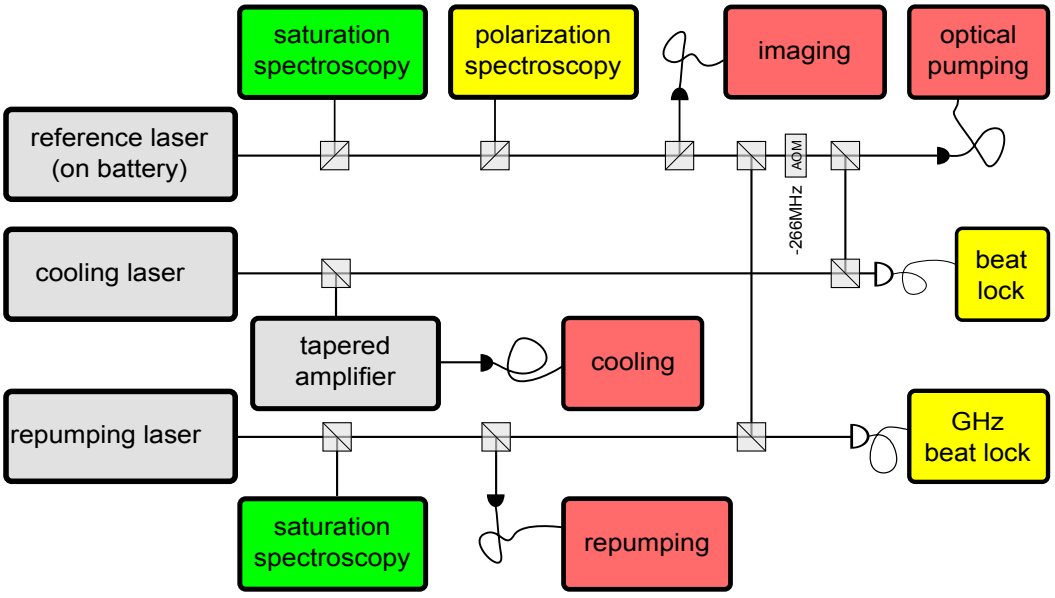

Figure 2.12: To generate tailor-made light for the experiment (red), different lasers (grey) are needed. To check and adjust frequencies, the reference and the repumping laser are connected to a saturation spectroscopy (green). The actual locking (yellow) is realized by polarization spectroscopy in the case of the reference laser, and by referenced beat locks for the cooling and the repumping laser. Imaging and optical pumping light is generated from the reference laser using AOMs.

laser driver with even improved current stability.

From the well-stabilized reference laser, the light for imaging and for optical pumping is deduced using acousto-optical modulators (AOMs). The characterization of the atomic ensembles solely relies on absorption imaging, which is explained in detail in Ref. [Ket99]. The imaging light needs to be resonant and quickly switchable, i.e. in less than 100 μs. This is achieved using two AOMs, one shifting the light 80 MHz up in frequency and a second one, shifting the light back to resonance (not shown in Fig. 2.12). The imaging light is spatially filtered in a single-mode fiber, has a final $1/e^2$ diameter of 10.9 mm and a power of 800 μW. The optical pumping light is converted from the reference light by an 266 MHz AOM, shifting it to the $F = 2 \rightarrow F' = 2$ transition. After filtering with a single-mode fiber and a telescope, the optical pumping beam has a $1/e^2$ diameter of 21.6 mm and a power of 115 μW. Additional apertures cut the Gaussian beam profile to a nearly homogeneous circular intensity distribution with 25.4 mm diameter. The beam is collinear with the vertical MOT beams and enters the chamber from the top.

The cooling light is generated in an integrated tapered amplifier system. It is frequency-stabilized by a beat lock, allowing adjustable detuning from the $F = 2 \rightarrow F' = 3$ resonance. Moreover, this locking technique suppresses possible 50 Hz noise (see above) in the cooling laser, even if the respective driver has no modifications. After spatial filtering in a fiber, the beam is widened with two telescopes to a $1/e^2$ diameter of 34.6 mm. A 25.4 mm aperture reshapes the cooling laser beam profile to a disk-like distribution of nearly constant intensity. This reshaped cooling beam has a power of 82.6 mW in total and is divided into six MOT laser beams. In the MOT phase, the laser is red-detuned by 23 MHz whereas in the molasses phase it has a red-detuning of 60 MHz.

GHz-Beat-Lock of the Repumping Laser

Particular attention has been paid to the stabilization of the repumping laser. Its purpose is to re-pump atoms from the $F = 1$ state back to the cooling cycle ($F = 2 \rightarrow \approx F' = 3$). It has a decisive influence on the MOT atom number and temperature, and, consequently, all following steps. A change in the lock point by 1 MHz can already be seen in the MOT fluorescence.

The GHz beat lock implementation (see Fig. 2.13 (a)) of the present experiment uses an ultra-fast photo diode[23] voltage-supplied by a GHz-capable bias-tee[24]. The signal is enhanced by two amplifiers[25] and fed into a frequency mixer[26]. The local oscillator for mixing is a signal generator[27], which allows down-conversion of the GHz signal to the few 100 MHz range over a wide spectrum and with very low frequency noise. A radio-frequency amplifier[28] finally tailors the signal to use established beat lock

[23]Model G4176-03, Hamamatsu Photonics, Herrsching, Germany.
[24]Model 5547, Picosecond Pulse Labs, Boulder, USA.
[25]Model ZX60-14012L+, Minicircuits, New York, USA.
[26]Model ZX05-153+, Minicircuits, New York, USA.
[27]Model SMR20, Rohde and Schwarz, Munich, Germany.
[28]Model ZHL-3A, Minicircuits, New York, USA.

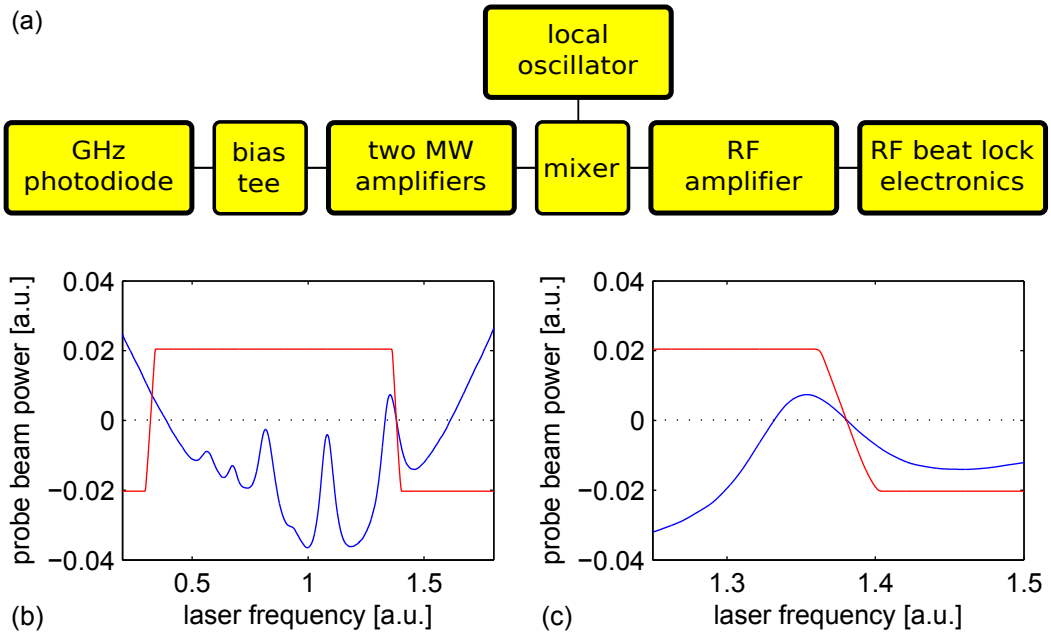

Figure 2.13: A schematic view of the GHz Beat Lock is given in (a). The measured repumping spectrum ($F = 1 \rightarrow F'$, shown in full in (b)) is plotted as blue line. The beat signal is drawn as red curve. Subfigure (c) contains a close-up of the spectrum and the beat signal around the $F = 1 \rightarrow F' = 2$ transition. A feedback circuit tries to regulate the beat signal to zero. Consequently, the laser is locked to the zero-crossing frequency of the falling beat signal slope. The shown lock point is used for the measurements and experimentally found for the best atom number - temperature ratio in the magnetic trap. Interestingly, the optimal performance is achieved for a slight blue detuning from the $F = 1 \rightarrow F' = 2$ transition.

electronics.

For the repumper stabilization, the local oscillator runs at 6422 MHz. The down-converted beating signal is stabilized at 157 MHz, which results in the lock point shown in Fig. 2.13 (b) and, zoomed, in (c). The latter is found experimentally, yielding the best ratio of atom number and temperature in the magnetic trap. The repumping light injects a slave laser[29] to amplify the light. After spatial filtering with a single-mode fiber, the beam is widened two times to a $1/e^2$ diameter of 17.3 mm. An aperture reshapes the Gaussian beam profile to a disk-like distribution of nearly constant intensity. This disk has a diameter of 25.4 mm and a total power of 16.1 mW (i.e. before the distribution among the six MOT laser beams).

Compared to the common saturation spectroscopy, stabilizing the repumping laser with a GHz beat lock to the reference laser is widely independent of the impinging power on the photo diode and has additional advantages. It relies only on the relative frequency of the lasers, allows arbitrary lock points (e.g. also on the peak of the $F = 1 \rightarrow F' = 2$ resonance), and, with the current implementation, extends the beat lock technique to GHz detunings. If the frequency of the reference laser is fixed

[29]Home-made diode laser, using the GH07895A6C diode by Sharp Electronics (Europe), Hamburg, Germany.

and given, the frequency of the stabilized lasers is then known in absolute numbers[30]. The GHz beating system is designed to work up to at least 10 GHz in terms of choice of components. The frequency resolution can be improved significantly over 1 MHz as obtained in this experiment, using a better spectrum analyzer and a sub-MHz reference laser stabilization.

2.3 Preparation of the Measurement

This section presents the main steps of the operation of the experimental setup, including a flow diagram of the experimental cycle. In particular, the deceleration of in-trap oscillations and the determination of the nanochip surface position by spatially resolved atom loss measurements are explained.

2.3.1 Experimental Cycle

An overview about the 80 s experimental cycle is given in Fig. 2.14. Initially, rubidium is released from a dispenser source (operated with 7 A for 14 s) and the isotope ^{87}Rb is captured in a magneto-optical trap (MOT) [Hän75, Raa87]. All relevant optical transitions are shown in Fig. 2.11. Applied laser powers, detunings, and beam diameters are summarized in Sec. 2.2.6. The current for the MOT in the respective coils is 1.07 A. The coils are generally operated in anti-Helmholtz configuration, i.e. with counter propagating currents in the upper and lower coil. The resulting gradient in the direction parallel to the symmetry axis of the coil is two times as large as in the direction perpendicular to it. At the end of the 20 s MOT period, 300×10^6 atoms at 130 μK are trapped and subsequently exposed to 5 ms of polarization-gradient cooling [Let88, Dal89]. Then, the atoms are optically pumped into the $F = 2, m_F = 2$ state (500 μs) and loaded into a purely magnetic spherical quadrupole trap. For optical pumping, the MOT coils are operate in Helmholtz mode (i.e. generating a homogeneous magnetic field, defining the quantization axis) whereas for the magnetic storage, it is switched back to the anti-Helmholtz configuration, now running at 3 A. The further transfer of the atomic ensemble towards the carrier chip is achieved solely by manipulating magnetic fields in a suitable manner. After the last step before activating the microscopic chip wires, i.e. after evaporative cooling [Dav95b, Ket96, Lui96] in the Ioffe trap formed by the Ioffe wire and the transfer coils, 7×10^6 atoms at 7 μK are available.

The transfer of the atoms from the Ioffe trap to a chip is explained in detail in Refs. [For03b, For03a, Ott03a]. The manipulation of atomic ensembles on the particular carrier chip used in the experiment (for layout, see Fig. 2.6) is studied extensively in Ref. [Gün03]. Besides the cloud manipulation directly needed to perform the scattering measurements (see Sec. 3.2), the center-of-mass oscillations of the

[30] As the beat signal is connected to the absolute value of the frequency difference, i.e. $|\nu_2 - \nu_1|$, another method is needed to find out which laser has the larger frequency. For GHz detunings, this is e.g. easily done with a wavelength meter.

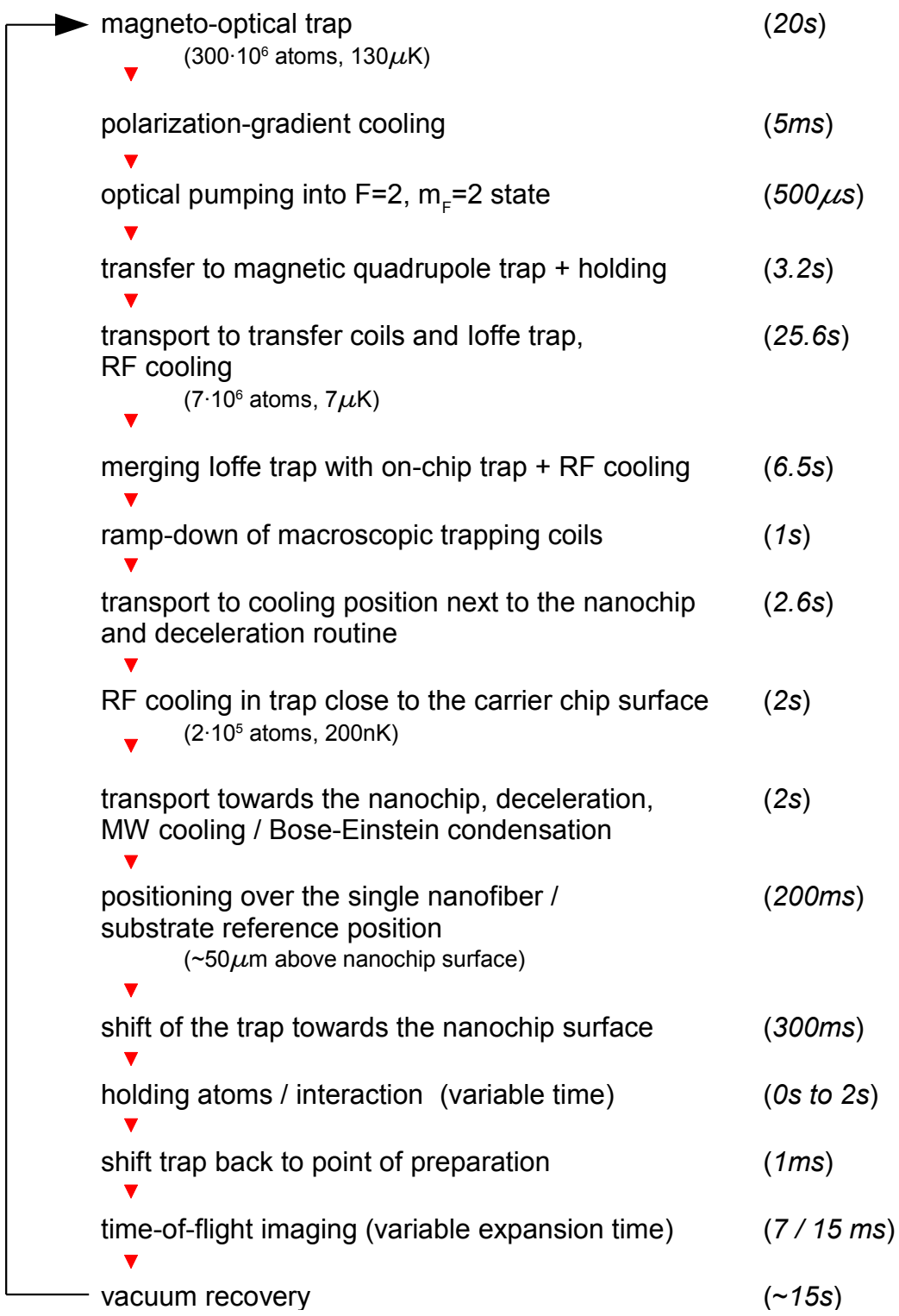

Figure 2.14: Flow chart of the experimental cycle (in total, 80 s). The duration of individual steps is printed italic.

atoms have to be damped out and the distance between the cloud and the nanochip surface has to be calibrated. These two important aspects of cloud control are discussed in detail in the following sections.

2.3.2 Center-of-Mass Oscillations

Each transport step of the atomic ensemble exposes the cloud to acceleration and deceleration processes. Due to the inertia of the cloud and the lack of friction in the magnetic potential, even if the magnetic trap has stopped, the cloud still moves and performs center-of-mass oscillations in the trap. For the scattering measurements, such oscillations are not desirable for at least two reasons. First, while preparing the cloud by evaporative cooling, center-of-mass oscillations limit the cooling efficiency. For colder and therefore smaller clouds, the effect gets more pronounced. Secondly, for the scattering measurements, the overlap between the atomic cloud and the nanofiber should be well adjustable and not varying over time. Therefore, center-of-mass oscillations should be reduced to a minimum.

For thermal clouds, one option to reduce the oscillation amplitude is to simply hold the cloud for many oscillation periods. Due to thermalization of the cloud, a damping is indeed visible. However, the kinetic energy of the center-of-mass oscillations is converted into higher thermal energy, i.e. the cloud heats up. If the oscillations are in phase for different experimental runs[31], oscillations can be strongly reduced by a suitable shift of the trap center. First, for a constant position of the magnetic field minimum, the oscillation amplitude, phase and frequency of the cloud are measured. Then, a deceleration routine can be implemented, which instantaneously shifts the trap center to the center-of-mass position of the cloud at one of the turning points of the undesired oscillation.

The effect of a suitable deceleration routine is visualized in Fig. 2.15. The plot shows the axial position of the cloud center-of-mass for different imaging times[32]. All positions are measured with 15 ms TOF. The reason for monitoring oscillation in TOF and not in-situ in the trap lies in a magnification of the oscillation amplitude by a factor of $\sqrt{1+\omega_a^2 t_{\mathrm{TOF}}^2}$ [G05]. Here, $\omega_a/(2\pi)$ is the axial trap frequency and t_{TOF} the time-of-flight duration, thus, the resolution of the measurement increases with t_{TOF}. The blue crosses in Fig. 2.15 show the free evolution of the cloud for 400 ms. The axial trap frequency of $\nu_a = \omega_a/(2\pi) = 16\,\mathrm{Hz}$, corresponding to oscillation periods of 62.5 ms is clearly visible in the data[33]. The in-trap oscillation amplitude before

[31] In the context of center-of-mass oscillations, the phase refers to the φ in $\sin(\omega t+\varphi)$, the latter term describing the center-of-mass position of the cloud. For a well-thermalized experimental setup, the phase of the axial oscillations stays constant over a few days. In contrast, measurements show that the phase of the radial oscillations behaves randomly. The reason for the latter has not yet been clearly identified.

[32] For both the free evolution and the decelerated motion, actual measurements are only taken in the time intervals from $0-100$ ms and $300-400$ ms but not between 100 ms and 300 ms. This data acquisition scheme reduces the number of points to be measured while maintaining a low error on the determined frequency and phase.

[33] The actual determination of the trap frequencies includes a similar oscillation measurement but with much higher resolution.

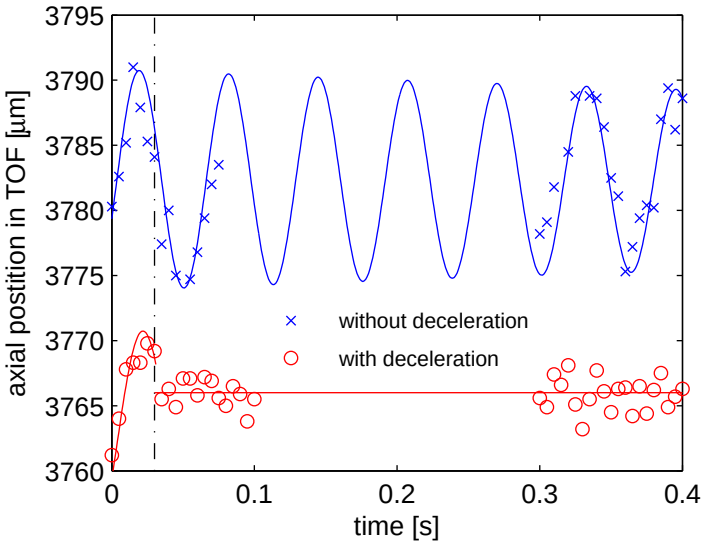

Figure 2.15: After a transport of the cloud by shifting the magnetic field minimum, the trap center stays at rest for $t \geq 0\,\mathrm{ms}$. The blue crosses show the axial center-of-mass position of the cloud against hold time for a free evolution of the cloud. An oscillation is clearly visible over the total time of the measurement. The curve marked with red circles shows the effect of the deceleration routine, applied at $30\,\mathrm{ms}$ (indicated by the vertical dash-dotted black line). Initially, up to $30\,\mathrm{ms}$, an in-trap motion of the cloud is visible. Then, the trap center is shifted such that the motion is stopped. For all times $t \geq 30\,\mathrm{ms}$, the cloud stays at rest at $\approx 3767\,\mu\mathrm{m}$. For visibility, the axial positions of the two data sets have been manually shifted with respect to each other by $20\,\mu\mathrm{m}$.

the deceleration can be counted back to $\approx 5\,\mu\mathrm{m}$. Taking into account the phase shift and amplitude enhancement due to the TOF imaging [GÖ5], a deceleration routine is programmed as outlined. The result is displayed as red circles in Fig. 2.15. In the first $30\,\mathrm{ms}$, a center-of-mass motion is still visible. Then, a trap shift is performed (indicated by a vertical dash-dotted line) and the cloud remains at rest at a position corresponding to about $3767\,\mu\mathrm{m}$ on the camera used for imaging. Even using the TOF magnification, the axial oscillations have been reduced below the fit-enhanced spatial resolution of the imaging system (the latter is approximately $6\,\mu\mathrm{m}$). The width of the position noise indicates an oscillation amplitude of below $1\,\mu\mathrm{m}$.

Although this method for cloud deceleration is a powerful tool to stop axial oscillations, it has an inherent drawback. The optimal position for the instantaneous trap shift is generally not the desired final position of the cloud. This is of small importance for evaporative cooling (as for this process, it does not exactly matter where the cloud is positioned) but can be problematic for the positioning of the cloud at the nanofiber. As a consequence, the cloud has to be decelerated in the proximity of the desired final position and, with an additional very slow shift of the trap center, the cloud has then to be moved to its final destination. However, this shift unavoidably results in small oscillations again.

As the phase of the radial oscillations is not constant from one experimental run

to another, these oscillations can generally not be decelerated by a shift of the trap center. The shift parameters change for each cycle. However, the radial oscillation amplitudes are much smaller than the axial ones due to the stronger radial confinement. They can be damped out by holding the cloud sufficiently long for thermalization to take place. The slight increase in cloud temperature can be compensated with additional evaporative cooling.

This trade-off works well for thermal clouds. However, for a BEC, damping center-of-mass oscillations by simply holding the cloud in the trap is very inefficient [Ott03b]. After 1 s storage time, axial oscillations of a BEC are still visible in the measurements. To circumvent this poor damping behavior, the BEC is created in very close proximity of the nanofiber to limit transport distances. The last steps of positioning are done by very slow shifts of the magnetic potential, i.e. the cloud is not shifted more than a few tens of micrometers within a few hundred milliseconds.

Overall, for the measurement with the thermal cloud as well as with the BEC, the amplitude of the center-of-mass oscillations have been reduced to a fraction of the extent of the cloud. For the thermal measurement, a radial oscillation cannot be resolved. The amplitude of the axial motion is below $\sigma_a/10$ (typically, $\sigma_a \approx 27\,\mu$m) of the Gaussian spatial distribution (see Eq. 4.18). In the case of the BEC, the radial motion is also not resolvable. However, axial osciallations are present, the amplitude is about $6\,\mu$m in the trap. At an axial Thomas-Fermi-radius $r_{\mathrm{TF,a}}$ of $16\,\mu$m (calculated for 10^4 atoms in a 16 Hz trap), this comparatively large oscillation amplitude corresponds to, at most, a 14% change in the condensate density. Moreover, for a partial overlap with the nanofiber, a damping of the BEC oscillations is visible and, in turn, the density variation of the BEC at the nanofiber due to oscillations will become smaller over time. In principle, taking atom loss into account, the reduction of in-trap condensate oscillation amplitudes by friction from a nanostructured surface can be a new method to damp BEC motion.

2.3.3 Surface Gauging

In addition to the deceleration of oscillations, the absolute positioning of the atoms with respect to the nanochip surface is an important aspect of cloud preparation. The distance d between the center-of-mass position of the non-oscillating cloud and the chip surface (see Fig. 3.1) is a crucial parameter to determine the nanofiber-cloud overlap. The latter is a central figure for the evaluation of both the ultracold thermal cloud and the BEC measurement.

In the context of ultracold atom experiments, the absolute determination of the distance between a cloud and a surface is still a challenge. In particular, this is true if the method should yield d with an accuracy better than $1\,\mu$m as it is desirable for the present experiment. This value for the latter accuracy goal becomes clear, considering the length of the nanofiber used for the measurements being approximately $10\,\mu$m. The knowledge of the trapping currents allows, in principle, to calculate the trap minimum relative to the plane of the wires (see Sec. 2.1.2). The effect of gravitation, i.e. a shift of the harmonic trap center, can simply be taken

into account by overlapping the magnetic potential with the gravitational potential for atoms with mass m. For gravitation along the y axis, the potential energy of the gravitational field is given by $m \cdot g \cdot y$, $g = 9.81\,\mathrm{m/s^2}$ being the respective acceleration. However, as the present experiment uses combined chips [GÖ5], i.e. a nanochip glued by hand on top of a carrier chip, solely relying on ab-initio calculations is not sufficient to determine the absolute cloud-nanochip surface distance[34]. Besides the question of the actual nanochip placement, it has to be noted that there is a difference between the "hard" surface position[35] and the opening position of the magnetic trap due to the attractive CP potential from the surface [Lin04, Har05, Obr07a]. The latter phenomenon can be understood, considering a $(x - x_0)^2$ potential with minimum at x_0 (the harmonic magnetic trap) overlapped with a $-1/x^4$ potential (retarded CP potential of a half space, see Sec. 1.2). With decreasing x_0, i.e. when the magnetic trap approaches the surface (origin of the CP forces), the $-1/x^4$ term becomes increasingly dominant. This lowers the trap depth and finally makes the trap vanishing (trap opening). In the following, it is always referred to the "hard" surface position because the position of magnetic trap opening is not unique and varies for different trap frequencies.

A direct way to measure the cloud-surface distance is suggested in Ref. [Sch03], using a surface reflection of the atom's absorption imaging shadow. However, as visible from Fig. 2.9, the nanochip used in the present experiment appears black and shows poor reflection properties. In addition, the nanochip is not a flat surface but carries extended structures which introduce fringes in the imaging. The direct use of interference fringes from the edge of the chip (as e.g. done in Ref. [Kas10]) does not provide the required accuracy. An evaluation of images from the experiment showed that the fringes have a position jitter of several micrometers.

To determine the absolute distance between the cloud and the nanochip surface, spatially resolved losses of atoms from the magnetic trap are measured in the proximity of the surface [Lin04]. The data is taken in a region without nanostructures, i.e. at the position marked with the green arrow in Fig. 3.2. For the thermal cloud as well as the BEC measurement, the atomic ensemble is prepared in a distance of approximately $50\,\mu$m away from the nanochip surface, where there is no interaction. Here, the trap frequencies are $(50, 50, 16)\,$Hz. The BEC contains approximately 10^4 atoms, the ultracold thermal cloud initially has a temperature of 80 nK and contains about 1.5×10^5 atoms. The trap frequencies increase with decreasing trap-nanochip separation and approach $(80, 80, 16)\,$Hz at nanochip surface. For the measurement, the current in the QP2 wire of the carrier chip is lowered within 300 ms and the trap is shifted towards the nanochip surface. The amount of trap displacement is known from the current ratio between compression wire and QP2. After displacing the trap

[34] Even if the thickness $d_{\mathrm{nanosubst}}$ of the nanochip substrate is known, the surface position of this chip is not necessarily simply $d_{\mathrm{nanosubst}}$ away from the carrier chip surface. A small gap between nano- and carrier chip due to imperfect glueing can shift the surface position by several micrometer (for chip assembly, see Sec. 2.2.5).

[35] The "hard" surface position refers to the position in the proximity of the surface at which atoms would get lost from a magnetic trap if there was no CP potential. In particular, this is the position, where the repulsive atom-atom interaction (e.g. Lennard-Jones interaction) becomes dominant.

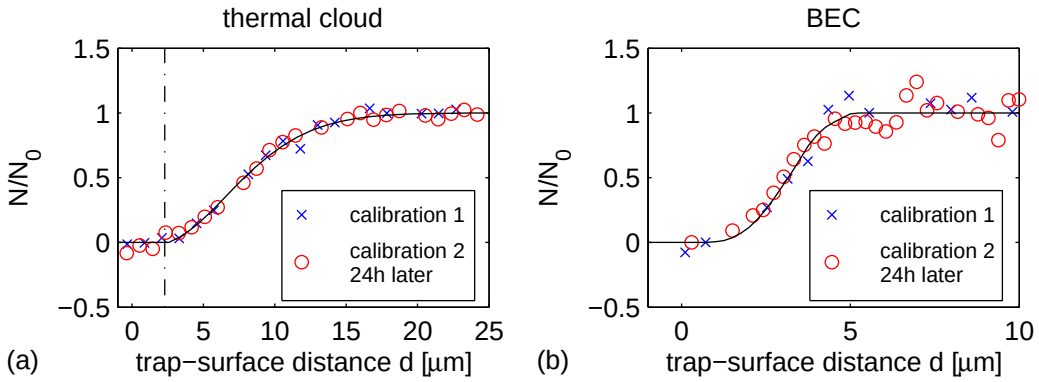

Figure 2.16: Determination of the nanochip surface with a $80\,\mathrm{nK}$ thermal cloud (a) and a Bose-Einstein condensate (b). Both sub-figures show the spatially resolved relative number of residual atoms N/N_0 in the magnetic trap close to the surface. Using the final fit results, the distances on the abscissa have been rescaled such that $0\,\mu\mathrm{m}$ corresponds to the "hard" surface of the nanochip. The vertical dash-dotted black line in (a) indicates the position where the trap depth used in Eq. 2.15 reduces to zero. As expected from the density profiles of the respective clouds, the loss happens over much larger distances in the case of the thermal cloud compared to the BEC. In (a) and (b), the red circles and blue crosses correspond, respectively, to two measurements taken with a delay of $24\,\mathrm{h}$, showing the absence of a surface drift. The fit functions are explained in the text.

a certain distance towards the nanochip surface, there is no surface interaction time but the cloud is immediately moved back to the point of preparation. The latter step is done in only 1 ms to minimize further loss between the actual surface interaction and the measurement of the atom number. At the point of preparation, the cloud is imaged with 7 ms TOF. This procedure is repeated for many cloud-surface distances d.

Typical measurement results are shown in Fig. 2.16 (a) for a thermal cloud and in (b) for a BEC. In both cases the relative number of remaining atoms in the trap N/N_0 reduces as the trap approaches the nanochip surface. This effect is known in the literature as surface evaporation [Rei99, Har03, Lin04, Pas04, Hun10]. Taking changes of the trap frequencies (see Eq. 2.9), the resulting adiabatic compression, and the surface Casimir-Polder potential into account (see Sec. 1.2), the atom losses can be accurately modeled [Gie10]. The attractive CP potential of the nanochip surfaces can, in the retarded limit $d \gg \lambda = 780/794\,\mathrm{nm}$, be described by [Suk93, Lin04]

$$U(d) = -\frac{C_4}{d^4}. \tag{2.13}$$

To quantify the particular ^{87}Rb - nanochip surface interaction, the coefficient C_4 is determined for the combination of silicon[36] and ^{87}Rb in the ground state. Using

[36]The nanochip substrate is made of silicon and, during the nanofiber production, covered with a 7.4 nm oxide layer. Due to the small amount of material compared to the rest of the substrate, the influence of SiO_2 for the CP potential is negligible [Cou96].

surface dispersion force theory [Dzy61, Ant04], the coefficient is calculated using tabulated properties of Si and ^{87}Rb [Lid07, Mar94, Der99], yielding $C_4 = 1.217 \times 10^{-55}\,\mathrm{Jm}^4$.

The sum of the harmonic magnetic trapping potential (see Sec. 2.1.2) and the CP potential from Eq. 2.13 gives the total potential for atoms in the proximity of the surface for the present experiment. Not explicitly accounting for any cloud dynamics, for a thermal gas, the fraction $F = N/N_0$ of remaining atoms in the trap can be described by [Lin04]

$$F = 1 - \exp(-\eta(d)) \tag{2.14}$$

$$\eta(d) = U_0(d)/(k_b T) \tag{2.15}$$

with $U_0(d)$ being the reduced depth of the magnetic potential due to the surface CP force and $k_b T$ the thermal energy of the cloud. As the atomic ensemble is not held at the surface, the model has been simplified compared to the original Ref. [Lin04], ignoring time-dependent evaporation. Using a 3D particle dynamics simulation for the total potential, it was confirmed that the time-independent Eq. 2.15 reproduces the simulated atom number decay reasonably well for parameters used in the experiment. The model has been fitted to the experimental data in Fig. 2.16 (a), approximating very well the outcome of the loss measurement. However, for an optimal matching of the model, a slight deviation between measured and fitted cloud temperature had to be taken into account. Minimizing the position offset between measurement and simulation yields the absolute position of the nanochip surface with respect to the plane of the carrier chip wires. For the thermal cloud scattering measurement, the nanochip surfaces is $265.4 \pm 0.5\,\mu$m away from the carrier chip.

To describe the BEC data from Fig. 2.16 (b), the Gross-Pitaevskii equation [Dal99] is simulated in one dimension for a BEC with 10^4 atoms in the combined CP-magnetic potential[37]. This data (the solid black line in Fig. 2.16 (b)) has been used to fit the measurements and shows very good agreement. As in the case of the thermal cloud, the BEC fit yields the absolute position of the nanochip surface with respect to the plane of the carrier chip. For the BEC scattering measurement, it is $263.35 \pm 0.5\,\mu$m.

The discrepancy between the surface positions determined with the thermal cloud and the BEC does not originate from errors in the model or uncertainties in the position-resolved loss data. The thermal and the BEC scattering measurements as well as their respective calibrations have been made with a time lag of one month. It is not surprising that the nanochip surface has shifted by a few micrometers over this time. Between the two experiments, the setup including the thermo-regulation of the chamber interior has been switched on and off several times.

To estimate the surface drift over the time of one complete scattering measurement (lasting one to two days), Fig. 2.16 (a) and (b) have to be considered individually. Both subfigures include two measurements which are taken with a delay of 24 h. They have been recorded shortly before and after the acquisition of the scattering data sets presented in this thesis. In the thermal cloud as well as in the BEC case, a

[37] The simulation is provided by Prof. Th. Judd, Institute of Physics, University of Tübingen.

drift in the absolute position of nanochip surface cannot be resolved and is certainly less than 500 nm. This result underlines the quality of the heat management of the chamber interior outlined in Sec. 2.2.2.

Chapter 3

Measurements

This chapter contains the main data sets acquired for the present thesis. The careful preparations outlined in Sec. 2.3 facilitate measuring the time-resolved, inelastic scattering of an ultracold thermal atom cloud and a BEC overlapping with one single, free-standing nanofiber. The experimental situation is sketched in Fig. 3.1.

To begin with, the relevant locations for the measurements are shown on SEM images of the nanochip (Sec. 3.1). Moreover, the geometry of the single nanofiber used for the scattering experiments is presented in detail. The first of two main parts of this chapter (Sec. 3.2) presents time-resolved loss measurements of ultracold thermal clouds partly overlapping with a single nanofiber. The second major part (Sec. 3.3) contains similar measurements with a Bose-Einstein condensate.

3.1 Measurement Positions and Shape of the Nanofiber

The particular positions on the nanochip, at which all inelastic scattering measurements are performed, are marked with two arrows in Fig. 3.2. The red arrow points to the location of the single, freestanding nanofiber used for the measurement sketched in Fig. 3.1. The green arrow indicates the position for the reference measurement. At both positions, patch potentials [McG04, Obr07b] play a negligibly role as discussed in Sec. A.1. The position of the single nanofiber has been found by laterally resolved loss measurements with a BEC, explained in detail in Ref. [Gie10]. For sufficiently cold thermal clouds as well as for BECs, there is no interaction with the surrounding lines of nanofibers when the atomic ensembles are at the position marked with the red arrow[1].

The nanofiber standing at the latter location is shown on SEM images in Fig. 3.1 (b) (as well as in Fig. 2.8 (c) and (d)). To be able to differentiate geometry from Casimir-

[1] It is $r_{\mathrm{TF,\,a}} < \sigma_a \ll 150/2\,\mu\mathrm{m}$ and $r_{\mathrm{TF,\,r}} < \sigma_r \ll 50/2\,\mu\mathrm{m}$ for typical values ($r_{\mathrm{TF,\,a}} = 16\,\mu\mathrm{m}$, $\sigma_a = 27\,\mu\mathrm{m}$, $r_{\mathrm{TF,\,r}} = 3.2\,\mu\mathrm{m}$, and $\sigma_r = 5.5\,\mu\mathrm{m}$). The quantities $r_{\mathrm{TF,\,a}}$ ($r_{\mathrm{TF,\,r}}$) and σ_a (σ_r) are the typical axial (radial) extents of the BEC and the thermal cloud, respectively. For definitions, see chapter 4.

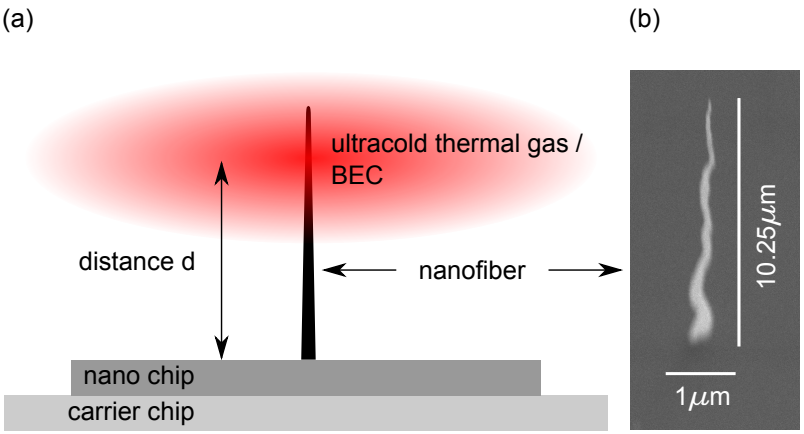

Figure 3.1: The experimental situation for the two scattering experiments, one involving ultracold thermal atoms and one involving a BEC, is sketched in (a). The cloud is positioned at an adjustable distance d from the nanochip surface. This changes, at the same time, the spatial overlap between the cloud and the nanofiber. In (b), an SEM image shows the nanofiber used for the scattering measurements.

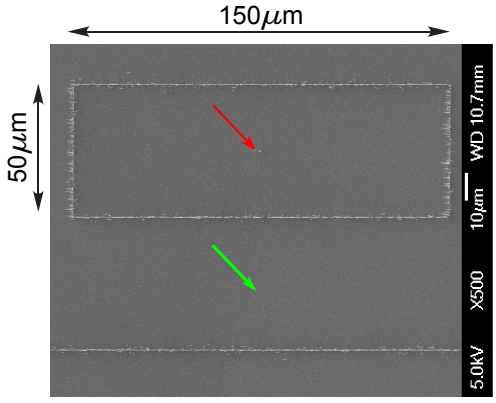

Figure 3.2: For the scattering measurements on a single nanofiber, the ultracold thermal cloud or the BEC are placed symmetrically inside the shown rectangular pattern of nanofibers. At this particular position on the nanochip (marked with a red arrow) stands the nanofiber used for all scattering measurements. The geometry of this nanofiber is shown in detail in Fig. 3.3. The reference measurements over the substrate are performed $50\,\mu\mathrm{m}$ away from the nanofiber, i.e. at the position marked with the green arrow.

Polder effects, the exact shape of this particular nanofiber used in the measurements is determined by an in-depth analysis of respective SEM pictures. All images have been taken under a 20° tilt angle with respect to the surface normal, making the fiber appear shorter. The true height h_{NF} is 10.25 μm, and the diameter varies from approximately 40 nm at the top to 275 nm at the bottom. As in the SEM pictures the nanofiber is not perfectly in the focus everywhere, the fiber silhouette is slightly washed out. This prevents a direct measurement of the nanofiber diameter with the desired accuracy. Using a fit, the imaging blur can be distinguished from the actual geometry of the nanofiber. The exact shape is shown in Fig. 3.3. It has been extracted from Fig. 2.8 (c), fitting each horizontal pixel line of the image with a convolution of a Gaussian and a box function.

Another aspect of imaging is, that only a two-dimensional projection of the fiber geometry (SEM image from one azimuthal angle only) is available. A shape variation of the nanofiber perpendicular to the imaging plane has not been measured. However, from the production process, the lateral extent of the fiber is assumed to vary isotropically. After all, the analysis of the SEM images allows one to determine the lateral extent of the fiber with a resolution of about 10 nm. Moreover, a possible thermal oscillation of the nanofiber, which would effectively let its diameter appear larger in the SEM images and the measurements, can be neglected. Following the calculations in Ref. [Kri98], the tip oscillation amplitude of the nanofiber used in the present experiment is estimated to be at most 5 nm. The uncertainties in the determination of the nanofiber geometry as well as oscillation effects are sufficiently small to be able to reliably infer the dispersive properties of the nanofiber.

3.2 Decay Dynamics of the Thermal Cloud

The experimental situation for the inelastic scattering measurement is sketched in Fig. 3.1 (a). As in the surface calibration measurements (see Sec. 2.3.3), a thermal cloud is prepared $\approx 50\,\mu$m away from the nanochip (trap frequencies $(50, 50, 16)$ Hz). This distance is sufficient to avoid interaction with the surface and the nanofiber. For the thermal cloud scattering experiment, an atomic ensemble at 100 nK, containing approximately 1.6×10^5 atoms, is prepared. The trap frequencies increase to $(80, 80, 16)$ Hz in the very proximity of the surface. The extent of the cloud is $\sigma_a = 27\,\mu$m and $\sigma_r = 5.5\,\mu$m at the surface (σ_a and σ_r are defined according to Eq. 4.12). At 100 nK, the characteristic atomic speed σ_v according to Eq. 4.13 is 3 mm/s.

3.2.1 Time-Resolved Atom Loss

To start the scattering measurement, the atomic cloud is brought into overlap with the nanofiber by shifting the trap center vertically towards the nanochip (see Fig. 3.1 (a)). After 300 ms of transport, the cloud stops at an adjustable distance d away from the nanochip surface. The corresponding approach velocities limit the stopping position overshoot to at most 300 nm, minimizing uncontrolled interaction.

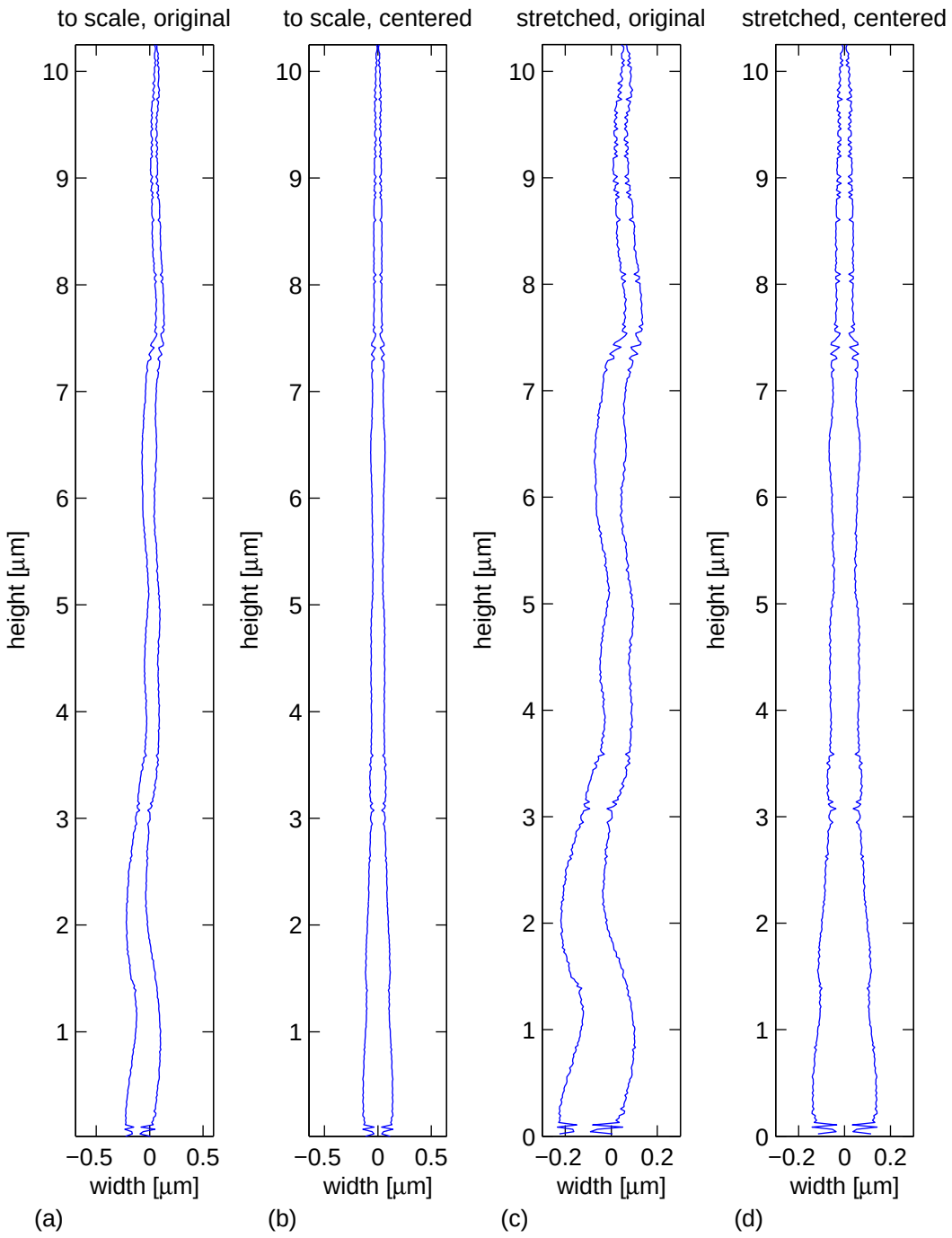

Figure 3.3: The exact geometry of the nanofiber used for the scattering measurements has been determined from the SEM image shown in Fig. 2.8 (c). A convolution of a Gaussian and a box function is fitted to each horizontal line of pixels. Thus, broadening due to a sub-optimal SEM focussing and the actual lateral extent of the nanofiber (plotted in this figure) can be differentiated. Subfigures (a) and (b) show the nanofiber silhouette with equal axis ratio, in (c) and (d) the abscissa is stretched to improve detail visibility. In (b) and (d), the slightly wavy line character of the fiber has been corrected.

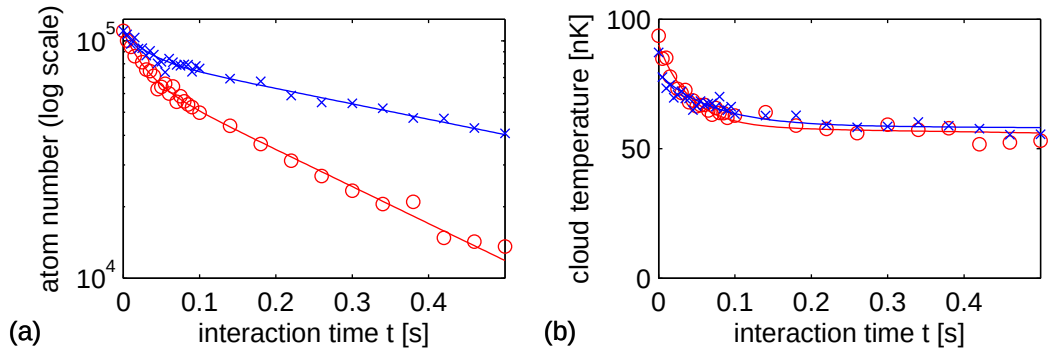

Figure 3.4: A representative example dataset, showing number of remaining atoms in the trap against interaction time ((a), semi-logarithmic plot). In (b), the corresponding cloud temperature is shown. The distance d between the trap center and the nanochip surface is $7.6\,\mu$m for the measurements in this figure. The data marked with red circles is taken with a cloud, partially overlapping with the nanofiber. The data points shown as blue crosses are a reference measurement over the plain substrate. A significantly faster decay of the in-trap atom number (a) in the case of an interaction with the nanofiber is clearly visible. The atom number is fitted with a double-exponential decay, the temperature with an offset exponential function. For both the nanofiber and the reference measurement, the temperature (b), first, decreases due surface evaporation. After approximately $150\,\mathrm{ms}$, the clouds equilibrate at $60\,\mathrm{nK}$.

At d, the atoms are held for interaction time t, and then, the trap is moved back to the point of preparation in 1 ms. Consecutively, the cloud expands for 7 ms TOF and is detected by absorption imaging. The measurement is repeated for different interaction times and, subsequently, for different trap-surface separations d. The latter allows studying different degrees of overlap between the atomic cloud and the nanofiber. The measurement outcome for one example distance $d = 7.6\,\mu$m is shown in Fig. 3.4.

In (a), the number of detected atoms N against interaction time t for the nanofiber case is semi-logarithmically plotted with red circles. The atom number drops rapidly in the beginning of the measurement. The loss slows down towards the maximally recorded interaction time of, for this overlap, 0.5 s. For comparison, Fig. 3.4 contains data of a similar atom scattering measurement conducted over the plain substrate (blue crosses). As the cloud is partially overlapping with the nanochip, there is a finite atom loss also in the case of the reference measurement. The trap-surface distance is, again, $d = 7.6\,\mu$m. A significantly higher loss for the situation with the nanofiber is clearly visible.

The cloud temperatures evolve in a similar way for the nanofiber and the reference measurement (see Fig. 3.4 (b)). A temperature reduction[2] due to surface evaporation is visible in the first 150 ms. At times $t > 150\,\mathrm{ms}$, the cloud equilibrates at 60 nK for both the nanofiber and the substrate measurement. The data is fitted with a

[2]As the loss of atoms to the surface can be on a time scale much shorter than the thermalization time, the cloud temperature is not always well defined. In this regime, the given temperature value can be regarded as a qualitative indicator for the extent of the cloud.

single exponential function and an offset, the latter corresponding to the equilibrium temperature T_{eq}.

The evolution of the temperature as well as the behavior $N(t)$ shown in Fig. 3.4 (a) suggest a particular model to fit the atomic decay. As visible in the semi-logarithmic plot, the number of atoms in the trap against interaction time can be well approximated as a double-exponential decay[3]. The fit functions shown in Fig. 3.4 (a) are of the form

$$N(t) = \left(N_1 e^{-\gamma_1 t} + N_2\right) \times e^{-\gamma_2 t} \tag{3.1}$$

with N_1 and N_2 being atom numbers, and γ_1 and γ_2 being decay rates. This fit function is, in addition, subject to important constraints:

$$\frac{1}{0.5\,\mathrm{s}} \leq \gamma_1 \leq \frac{1}{5\,\mathrm{ms}} \tag{3.2}$$

$$\frac{1}{20\,\mathrm{s}} \leq \gamma_2 \leq \frac{1}{5\,\mathrm{ms}} \tag{3.3}$$

$$\gamma_1/\gamma_2 \leq 20 \tag{3.4}$$

$$N_1(\gamma_1 - \gamma_2) \geq 0. \tag{3.5}$$

The relations 3.2 and 3.3 account for unphysically fast decay rates as well as a technical limit for the fit routine when approximating a constant atom number, i.e. an infinitely slow decay. The constraint 3.4 prevents unphysically fast transitions from decay rate γ_1 to γ_2, i.e. a kink in the fit. To ensure that a possible single-exponential decay behavior is always solely described by the γ_2 term, the fit is further constraint by relation 3.5.

The functional dependence of $N(t)$ in Eq. 3.1 and the constraints determine the physical meaning of the two decay rates. While γ_1 accounts for the decay at small interaction times, γ_2 describes the loss of atoms at large time scales. Taking into account the thermalization visible in Fig. 3.4 (b), γ_1 consequently approximates the regime of surface evaporation and γ_2 accounts for the characteristic atom number decay at small temperature change. The fit values for the example curves in Fig. 3.4 (a) are

$$\begin{aligned} \text{nanofiber} &: N_1 = 37391,\ N_2 = 71428,\ \gamma_1 = 35.0\,/\mathrm{s},\ \gamma_2 = 3.6\,/\mathrm{s} \\ \text{reference / substrate} &: N_1 = 23738,\ N_2 = 84886,\ \gamma_1 = 29.8\,/\mathrm{s},\ \gamma_2 = 1.5\,/\mathrm{s}, \end{aligned}$$

confirming quantitatively that atoms get lost faster for the situation with the nanofiber.

[3]The double-exponential decay is an empirical approach to model the experimental data. Other models have been studied as well, in particular a fit function of the form $\dot{N} = -\gamma(t)N,\ \gamma(t) = \gamma_0 \exp(-\gamma_k t),\ N(0) = N_0$. The idea is that the decay rate depends on the momentary overlap of the cloud and the scatterers. As evaporation reduces the cloud size and, thus, the overlap, the decay rate will decrease with time. Therefore, γ is not constant but time-dependent and has empirically been chosen to be single-exponential. For approximating the data, this approach performs similarly well as the double-exponential decay, having one fit variable less than the latter. However, as questions remain unanswered concerning the exact interpretation of the variables, it was not further considered.

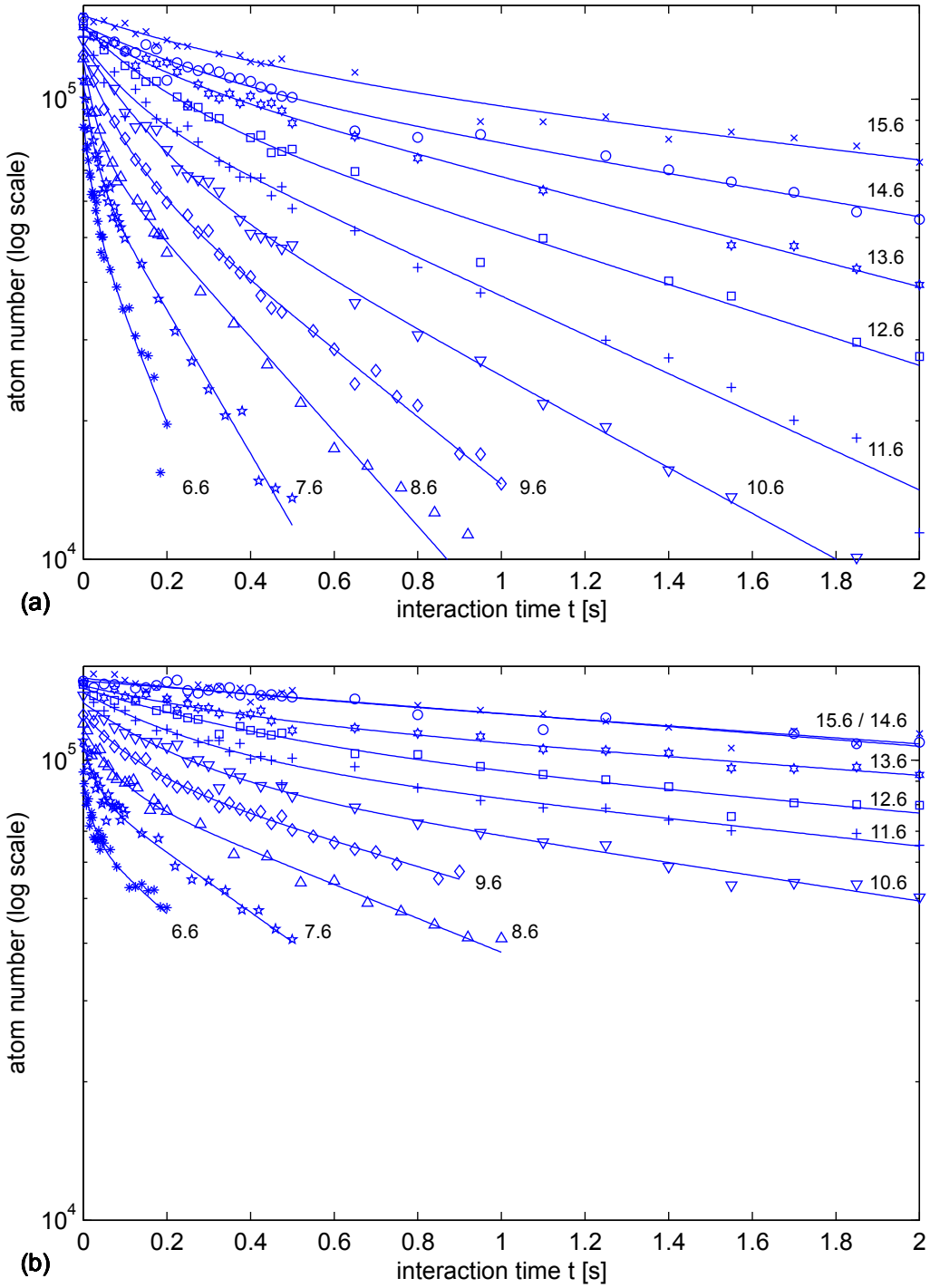

Figure 3.5: Ultracold thermal cloud scattering data plotted semi-logarithmically for the nanofiber (a) and the substrate (b). The trap-surface distance d for each curve is given in micrometers. As expected, with increasing overlap between cloud and scatterer (nanofiber and/or surface), the losses increase. A faster decay for the case with the nanofiber is always visible. Note that (a) and (b) have the same axis scaling.

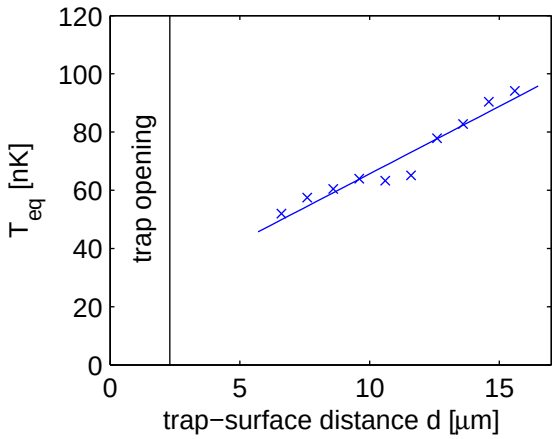

Figure 3.6: Distance-dependent equilibrium temperatures T_{eq} for the measurements presented in Fig. 3.5 against trap-surface distance d. The estimation of equilibrium temperatures T_{eq} is illustrated in Fig. 3.4. For decreasing d, T_{eq} decreases. This can be understood in the framework of surface evaporative cooling. The data has been fitted with a linear function $T_{\mathrm{eq}}(d)$. The solid vertical black line indicates the opening of the magnetic trap due to attractive Casimir-Polder forces from the substrate.

Data sets have been acquired for ten cloud-surface separations (6.6 μm to 16.6 μm) corresponding to ten different degrees of overlap between the cloud and the nanofiber. For each of theses measurements, reference decay curves have been taken for the same nanochip-cloud separation above the plain substrate. The complete atom number dataset is shown in Fig. 3.5. Subfigure (a) contains the measurements on the nanofiber. In (b), the reference data is plotted with the same axis scaling. The curves of slowest decay in (a) and (b) have been measured at a trap-surface distance of 15.6 μm, the steepest curves are taken for $d = 6.6\,\mu$m. The trap-surface distance d for each curve in Fig. 3.5 (a) and (b) is specified next to the data points in units of micrometers. The data shows a very well ordered behavior: For increasing overlap between the cloud and the scatterers (nanofiber and/or surface), the decay gets monotonically faster. All curves are fitted with Eq. 3.1, taking into account the discussed constraints.

The equilibrium temperatures T_{eq} (see Fig. 3.4 (b)) obtained for the thermal scattering measurements are summarized in Fig. 3.6, averaging the obtained temperatures for nanofiber and reference measurement[4]. For decreasing trap-surface separation, T_{eq} decreases, which is consistent in the framework of surface evaporation. As the "evaporation knife", i.e. the surface of the substrate, cuts more deeply into the cloud, the resulting temperature decreases. As there is no elaborated theory on sur-

[4]The deviation in T_{eq} is in the largest case 15% and typically below 5%.

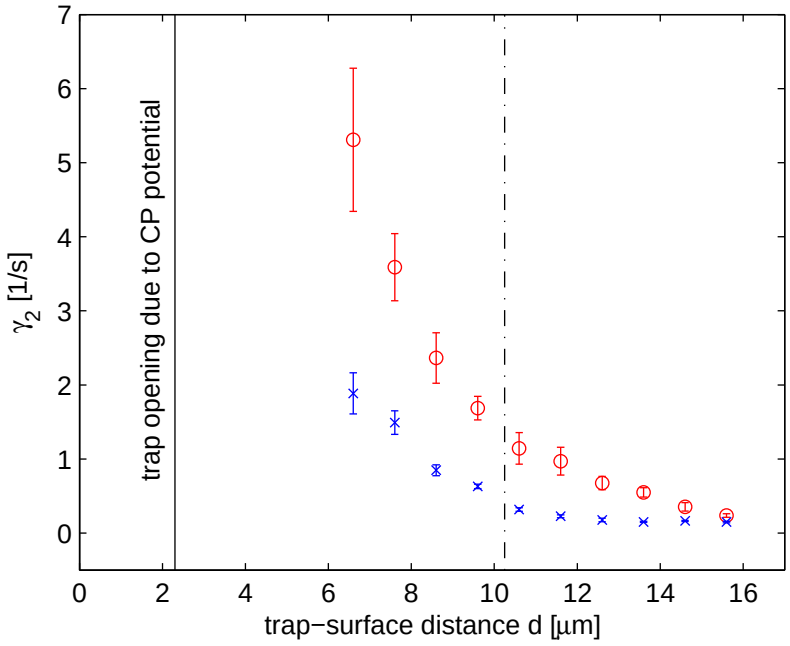

Figure 3.7: Inelastic scattering rates γ_2 of a thermal cloud overlapping with a nanofiber (red circles) and interacting solely with the substrate (blue crosses). The dash-dotted vertical black line indicates the height of the nanofiber. The magnetic trap opening due to CP forces from the substrate is indicated with the solid vertical black line. As the cloud has a finite width, losses already occur even if the trap center has not yet reached the nanofiber or the surface. For the nanofiber as well as the substrate case, the scattering rates increase with decreasing trap-surface separation. The rates measured for the nanofiber are always significantly higher than the reference. No data has been taken for trap surface separations below $6.6\,\mu$m as the atoms get lost too fast to quantify the decay.

face evaporation[5], the temperatures are simply fit with a linear function, yielding

$$T_{\mathrm{eq}}(d) = d \cdot 4.64 \times 10^{-3}\,\mathrm{K/m} - 21.5 \times 10^{-9}\,\mathrm{K}. \tag{3.6}$$

3.2.2 Inelastic Scattering Rates

The knowledge about the particular decay dynamics of an ultracold atomic ensemble allows to learn about the ensemble itself as well as the (possibly external) cause of the loss process [Bur97]. In the present analysis, the goal is to qualitatively understand the loss data set. A quantitative discussion is given in Sec. 4.3.3.

For the further evaluation of the scattering data, only the near-equilibrium situation described by the loss rates γ_2 will be considered. Not only the actual values of γ_2

[5]There is a well-developed theory on evaporation in energy-space, i.e. for RF or MW cooling [Dav95b, Ket96, Lui96]. However, surface cooling is an evaporative process in position space (involving several energies at the same time) which prevents a direct application of the existing theory.

are obtained from a fit but also the error of this decay rate. For a value resulting from a constraint fit as it is the case for γ_2, this is not trivial as e.g. a covariance matrix analysis does not take into account constraint violations correctly. To get an error estimate for γ_2, a Monte-Carlo simulation is used [Pre92]. Once a fit for a measured decay curve has been obtained (respecting the constraints), the standard deviation σ_N of the measured atom number from the fit can be calculated. For the scattering measurements, σ_N is typically below 5%, which is an exceptionally low value and an indicator for the very good stability of the setup. Using this standard deviation, a virtual measurement sample can be generated (corresponding quantities x are marked as $\mathring{x}$), randomly distributed around the obtained fit. The width of the spread of the virtual data points around the fit function is exactly chosen to be the standard deviation σ_N, obtained from the original data. The generated virtual sample undergoes a usual constrained fit with Eq. 3.1, yielding fit parameters $\mathring{N}_1$, $\mathring{N}_2$, $\mathring{\gamma}_1$, $\mathring{\gamma}_2$ for the virtual sample. This procedure is repeated over many (for the present analysis 50) virtual samples and a statistic is made over the obtained (virtual) $\mathring{\gamma}_2$ values. The standard deviation $\sigma_{\mathring{\gamma}_2}$ of this distribution is a measure for the uncertainty of the real-data fit value γ_2 for one measured decay curve [Pre92]. In the following, the error of γ_2 is calculated as $2 \cdot \sigma_{\mathring{\gamma}_2}$, corresponding to the 95% confidence interval.

The decay parameters γ_2 and respective errors have been extracted from the data in Fig. 3.5 and plotted against the trap-surface separation d. The results for the nanofiber are given as red circles in Fig. 3.7, blue crosses show the substrate results for reference. The height of the nanofiber is indicated by the dash-dotted vertical line, and the position of trap opening due to substrate surface CP forces is marked with a solid vertical line. For decreasing d, i.e. with increasing overlap between the cloud and the scatterers (nanofiber and/or substrate), the scattering rates increase. As visible from the figure, even for trap-surface separations larger than the height of the nanofiber, there is a significant contribution from the substrate. Therefore, the obtained γ_2 for the nanofiber measurements always contain a loss contribution originating from the cloud-substrate interaction. However, the losses measured at the nanofiber are for all values of d clearly larger than their counterparts measured above the plain substrate surface. Thus, the presence of the nanofiber clearly has an effect on the atom loss from the magnetic trap and will be discussed quantitatively in Sec. 4.3.

3.3 Decay Dynamics of the Bose-Einstein Condensate

In addition to scattering measurements involving an ultracold thermal cloud, experiments have been made to study the interaction of a Bose-Einstein condensate, partially overlapping with a single, free-standing nanofiber. As in the thermal case, the BEC scattering data is obtained on the specific nanofiber discussed in Sec. 3.1. The degenerate quantum gas is prepared approximately 50 μm away from the chip surface and typically consists of about 10^4 atoms. In the proximity of the sur-

face, the frequencies of the magnetic trap are $(80, 80, 16)$ Hz, resulting in typical Thomas-Fermi radii r_{TF} (see Eq. 4.47) of $(3.2, 3.2, 16)\,\mu$m, respectively. The chemical potential μ is 14 nK, the healing length results to $\xi = 440$ nm, and the speed of sound is $\bar{v}_s = 0.8$ mm/s (for the definition of these quantities, see Sec. 4.4.2). Details to the cloud preparation are summarized in Sec. 2.3.

3.3.1 Time-Resolved Atom Loss

To begin the BEC-nanofiber interaction experiment, the magnetic trap containing the condensed atoms is shifted towards the surface in 300 ms. At a specific trap-surface separation d (see Fig. 3.1 (a)), corresponding to a particular relative overlap between the BEC and the nanofiber, the cloud is held for variable interaction times t. Consecutively, the trap is shifted back to the point of cloud preparation within 1 ms, and the number of remaining atoms in the trap is measured after 7 ms TOF.

An example dataset of the number of remaining atoms in the trap against interaction time is shown in Fig. 3.8. Subfigure (a) has linear axis scaling, in (b), the ordinate is scaled logarithmically. As a guidance for the eye, a dotted horizontal line indicates a level of 500 atoms. Below this threshold, the number of atoms in the trap cannot be reliably determined from the absorption images. The data is taken at a trap-surface distance $d = 8.65\,\mu$m for both the nanofiber case (shown as red circles) and the reference case measured over the plain substrate (shown as blue crosses). Considering the height of the nanofiber ($10.25\,\mu$m) and the radial extent of the cloud ($r_{\mathrm{TF,r}} = 3.2\,\mu$m), the qualitative behavior of the decay in Fig. 3.8 is easily understood. For a trap-surface distance d of $8.65\,\mu$m, the cloud is solely overlapping with the nanofiber but sufficiently far away from the substrate to show respective interaction. Consequently, there is a significant decay for the measurement involving the nanofiber but nearly no atom losses are observed in the reference measurement.

As discussed in Secs. 4.4.1 and 4.4.2, the microscopic modeling of the atom loss from a BEC due to the presence of a nanofiber is a non-trivial task. However, the particular form of the atomic decay suggests an empirical approach to fit the measurements. As visible in the semi-logarithmic plot (Fig. 3.8 (b)), a single-exponential decay constitutes a reasonable fit function[6]. Thus, for the degenerate atomic cloud, the dependence $N(t)$, i.e. the number of remaining atoms in the trap against interaction time, is assumed to be

$$N(t) = N_0 \exp(-\gamma t) \tag{3.7}$$

with N_0 being the initial atom number and γ the single-exponential decay rate. The dependence in Eq. 3.7 is fitted to the experimental data without any constraints. The results for the nanofiber as well as the reference case are shown in Fig. 3.8 as solid red and blue lines, respectively. The fit parameters for the exemplary decay at

[6] An application of the thermal cloud fit function (Eq. 3.1) to the BEC data is no reasonable option: both the (surface evaporative) cooling as well as the equilibrium temperature found for the thermal cloud have no correspondence in the BEC case.

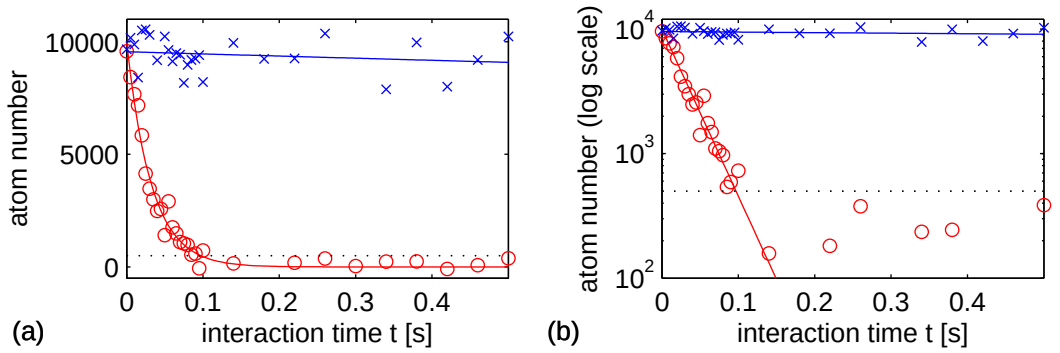

Figure 3.8: A representative example dataset of the time-resolved, totally inelastic scattering measurement of a BEC, partially overlapping with a single carbon nanofiber. For both the nanofiber results (red circles) and the reference measurement over the plain substrate (blue crosses), the trap-surface separation d is $8.65\,\mu$m. The figure plots the number of remaining atoms in the magnetic trap against interaction time. In (a), the axis scaling is linear, whereas in (b), the data is shown with semi-logarithmic scaling. The significantly faster decay in the nanofiber case is clearly visible. As expected from a comparison of the radial Thomas-Fermi radius of the BEC ($r_{\mathrm{TF,r}} = 3.2\,\mu$m) and the trap-surface separation, there is nearly no loss for the reference measurement over the plain substrate. The data is fitted with a single-exponential decay. The results are shown as red and blue solid lines. As guide for the eye, dotted lines indicate the level of 500 atoms. Below this threshold, the determination of the atom number is not reliable anymore when using the imaging system of the present experiment.

$d = 8.65\,\mu$m are found to be

$$\begin{aligned} \text{nanofiber} &: N_0 = 9965,\ \gamma = 31\,/\mathrm{s} \\ \text{reference / substrate} &: N_0 = 9555,\ \gamma = 0.1\,/\mathrm{s}. \end{aligned}$$

The much faster decay in the case of the nanofiber is also quantitatively manifest as the nanofiber rate exceeds the reference signal by two orders of magnitude. For the BEC measurement, errors for the decay rate can be directly obtained from a covariance matrix analysis of the fit.

3.3.2 Inelastic Scattering Rates

Datasets as shown in Fig. 3.8 have been taken for 20 different trap-surface distances d. In total, this corresponds to 1200 tuples $\{N, t\}$, 600 for the nanofiber and 600 for the reference measurement, respectively. For convenience, it is abstained from plotting the complete dataset. Instead, all decays are fitted with Eq. 3.7 and the resulting values for the decay rate γ are plotted against the trap-surface distance d in Fig. 3.9. The position of the trap opening due to attractive substrate surface CP forces is indicated by a solid vertical black line. The dash-dotted vertical black line indicates the position of the tip of the nanofiber. The scattering rates γ for the measurements involving the nanofiber are shown as red circles, and the respective

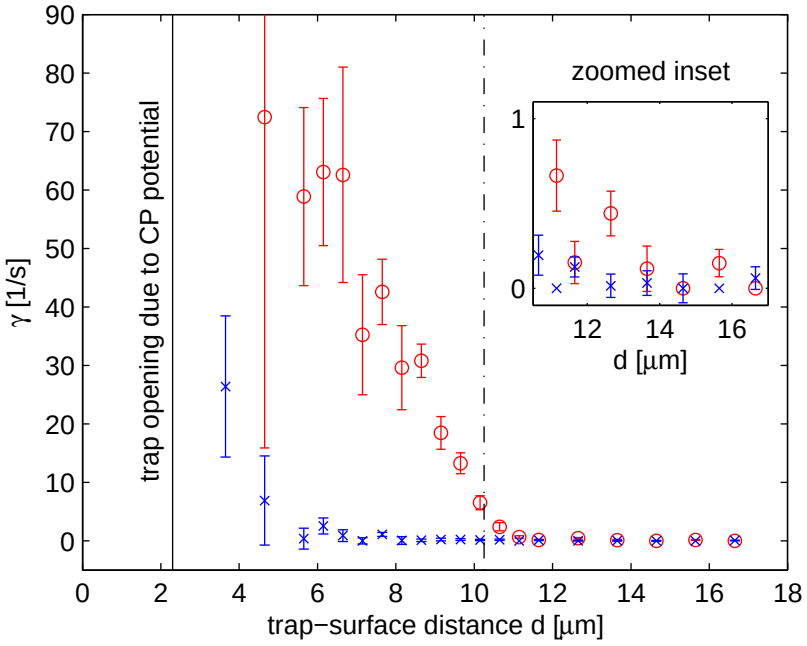

Figure 3.9: Totally inelastic scattering of a Bose-Einstein condensate, partially overlapping with a nanofiber. The rates γ for the loss of atoms from the trap against the trap-surface separation d are shown for nanofiber case (red circles) and the reference measurement (blue crosses). A solid vertical black line indicates the opening of the magnetic trap due to CP forces from the substrate. The dash-dotted vertical black line indicates the position of the tip of the nanofiber. For decreasing d, the overlap between the BEC and the scatterers (nanofiber and/or substrate) increases, which leads to increasing γ. For the nanofiber, a clear onset of scattering below $d \approx 13.5\,\mu$m (shown in particular in the zoomed inset) is clearly visible. These observations are comprehensible considering the BEC's Thomas-Fermi radius $r_{\mathrm{TF,r}} = 3.2\,\mu$m as well as the height of the nanofiber ($10.25\,\mu$m). There is no significant loss of atoms to the substrate until the cloud is effected by the trap opening towards the substrate surface, as visible from the reference data. The measurements illustrate the high degree of control of the BEC-nanofiber interaction achieved in the present experiment.

reference rates obtained over the plain substrate are plotted as blue crosses.

For decreasing trap-surface distance, i.e. for an increasing overlap of the cloud with the scatterers (nanofiber and/or substrate), γ increases. However, in contrast to the measurements with an ultracold thermal gas (see Fig. 3.7), for the BEC, a sharp onset of atom loss is visible. This becomes clear from the well-localized Thomas-Fermi density distribution of the BEC as compared to the largely spread Gaussian distribution of a thermal cloud (see chapter 4). Discussing first the nanofiber case, there is no visible atom loss for d larger than approximately $13.5\,\mu$m. Between $10\,\mu$m and $13.5\,\mu$m, the decay rate is very small and therefore shown as a zoomed inset in Fig. 3.9. The onset behavior can be understood, considering the radial extent of the atom cloud. As the radial Thomas-Fermi radius $r_{\mathrm{TF,r}}$ of the BEC is approximately $3.2\,\mu$m, losses are expected to start at $d < h_{\mathrm{NF}} + r_{\mathrm{TF,r}} = (10.25 + 3.2)\,\mu\mathrm{m} = 13.45\,\mu\mathrm{m}$ which is in agreement with the measurements.

The reference scattering rates, measured over the plain substrate, are close to zero for all values of d larger than $5.5\,\mu$m. Considering, again, the radial Thomas-Fermi radius $r_{\mathrm{TF,r}} = 3.2\,\mu$m of the BEC, in this region of d, very low values of γ are expected as there is no overlap between the cloud and the substrate. At $d = 2.3\,\mu$m, the magnetic trap opens due do CP forces from the substrate. If the magnetic trap approaches respective distances, i.e. d smaller than approximately $(2.3 + 3.2)\,\mu\mathrm{m} = 5.5\,\mu$m, atoms get lost to the surface and the reference value of γ increases.

The analysis of the BEC scattering data with a single-exponential fit function provides an intuitive picture of the experiment. Due to the small spatial extent of the BEC compared to the thermal cloud, in the degenerate case, an interaction of the atomic ensemble solely with the nanofiber and not with the substrate is experimentally accessible. The observed onset of losses is in very good agreement with the expected behavior from the nanofiber geometry and the shape of the ultracold cloud. A quantitative evaluation of the BEC loss data is given in Sec. 4.4.3.

Chapter 4

Theory, Evaluation, and Discussion

This part of the thesis focuses on the quantitative description of the decay data given in chapter 3. The presented theoretical approaches allow to connect the geometric and dispersive properties of the nanofiber to the experimentally obtained decay curves.

In Sec. 4.1, the Casimir-Polder potential of the nanofiber with the geometry as given in Sec. 3.1 is discussed. Then, general loss mechanisms of thermal and BEC atoms from magnetics traps are briefly reviewed in Sec. 4.2. In Sec. 4.3, a microscopic theory of the loss of thermal atoms due to the presence of an immersed nanofiber is outlined. This theory is applied to the experimental data, yielding a Casimir-Polder coefficient for the nanofiber. The decay of a BEC overlapping with a nanofiber is theoretically discussed in Sec. 4.4. The experimentally obtained decay data is quantitatively described by an Casimir-Polder-enhanced scattering radius of the nanofiber. Finally, the results for the thermal cloud and the BEC are discussed in Sec. 4.5.

4.1 Casimir-Polder Potential of a Nanofiber

The measurements presented in chapter 3 do not directly position-resolve the CP potential[1] but account for nanofiber CP effects on atoms distributed over a larger volume (i.e. at many positions at the same time). Nonetheless, the measurements presented in this thesis allow more than a qualitative description of the CP potential of the nanofiber. In the following, model functions for the radial dependence $U(r)$ for the nanofiber's CP potential are discussed. They are important to make the connection between the atom loss from chapter 3 and the dispersive properties of the nanofiber.

[1] If the CP potential of the nanofiber is described by a function $U(\vec{r})$, the particular dependence on $\vec{r}$ is not directly resolved within the framework of this thesis.

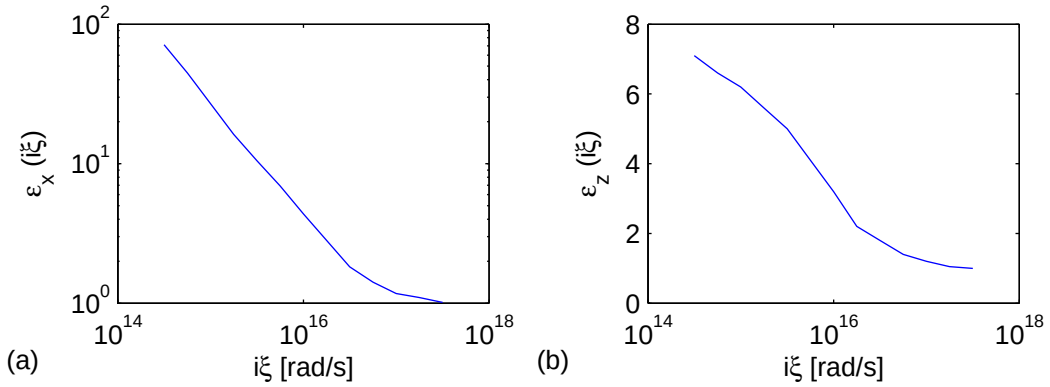

Figure 4.1: Dielectric function $\varepsilon_x(i\xi)$ of uniaxial crystal graphite against frequency for the electric field vector within the hexagonal layer (a) and perpendicular to it, $\varepsilon_z(i\xi)$, in (b). As it is clear from the geometry of a nanotube, ε is highly anisotropic. The figure has been reproduced from Ref. [Bla05].

4.1.1 Dielectric Properties

Independent of the applied theoretical dispersion force framework (see Sec. 1.2), the calculation of the CP potential of a dielectric object requires the knowledge of the object's frequency-dependent dielectric tensor. The exact dielectric behavior of the nanofiber used in the present experiment is not known, as the fiber is an assembly of several multi-wall nanotubes of unknown chirality.

According to Blagov et al. [Bla05], the highly anisotropic dielectric behavior of uniaxial crystal graphite [Ven75] is a suitable approximation for multi-wall nanotubes. The large aspect ratio of nanotubes (length vs. diameter) shall influence the tubes' dielectric properties. The dielectric tensor can be reduced to two frequency-dependent dielectric functions $\varepsilon(i\xi)$: One accounts for electric field vectors orientated parallel to the long axis of the nanofiber, the other for fields perpendicular to the axis. Given along the so-called imaginary frequency axis[2], $\varepsilon(i\xi)$ for uniaxial crystal graphite is provided in Ref. [Bla05] and reproduced in Fig. 4.1. Both dielectric functions, the one for the electric field vector within the hexagonal layer (a) and perpendicular to it (b) in Fig. 4.1, are obtained from experimental data.

As the nanofiber used in the present experiment consists of a bundle of multi-wall nanotubes, the dielectric behavior can differ from Fig. 4.1. However, the deviation is assumed to be small. A comparison shows that the frequency-dependent dielectric functions $\varepsilon(i\xi)$ of multi-wall nanotubes and respective bundles are all within the same order of magnitude. Casimir-Polder results obtained from the different dielectric functions are largely independent of the respective details. Thus, to model the nanofiber in the present experiment, the $\varepsilon(i\xi)$ from Ref. [Bla05] can be regarded as

[2]The designation as "imaginary frequency axis" is common in the literature but easily misleading. It would be more intuitive to speak of exponential than imaginary frequencies, as they pertain to the ways in which spontaneous charge fluctuations decay for an exponential frequency range. The dielectric functions given in dependence of these exponential frequencies are smoothed and without the spikes of absorption and dispersion of real frequency oscillations [Par06].

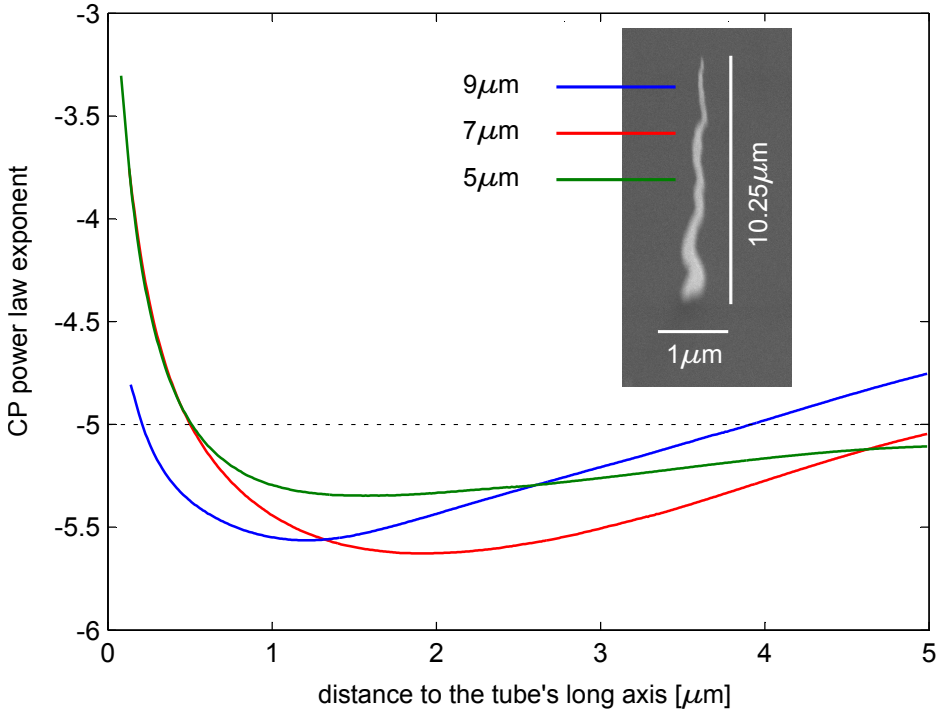

Figure 4.2: Power law exponent of the Casimir-Polder potential of a finite-size nanofiber against the distance between the ^{87}Rb atom and the long symmetry axis of the nanofiber. The three curves (green, red, blue) show the radial dependence of the exponent in planes displaced $5\,\mu$m, $7\,\mu$m, and $9\,\mu$m from the plane of the substrate, respectively (see inset). Finite-size effects of the nanofiber as well as the increasing influence of retardation for large distances are clearly visible. The first phenomenon can be seen for the blue curve which shows a significant deviation from the expected $1/d^3$ scaling for very small atom-nanofiber separations. The local minima of all three power law exponent curves are connected to retardation effects. They are weakening the CP potential for distances larger than the characteristic transition wavelength.

a reliable basis for CP calculation, well approximating the dielectric properties of the nanofiber.

4.1.2 Hybrid Hamaker - Casimir-Polder Approach

Both Lifshitz theory as well as macroscopic QED (see Sec. 1.2) are neither available for cylinders of finite length nor for objects shaped approximately as a truncated cone as it is the case for the nanofiber (compare Fig. 3.3). As the measurements within the present experiment are mainly performed at the tip of a nanofiber, it would be desirable to consider this particular geometry. In a theoretical approach by Prof. Th. Judd, Institute of Physics, University of Tübingen, the true shape of the used nanofiber, shown in the SEM inset in Fig. 4.2, is taken into account [Jud10b]. The dispersive interaction between an atom and the nanofiber is calculated by breaking the latter into small blocks and summing over all these elements, i.e. adapting the original idea of Hamaker [Ham37]. Each block is characterized by the angle-dependent dielectric bulk-material behavior as outlined in Sec. 4.1.1. Retardation is

taken into account by fourth order perturbation theory as in Ref. [Cas48b]. Moreover, the ansatz considers temperature effects by sampling atom and nanofiber properties exactly at the Matsubara frequencies (see Sec. 1.2).

The results of this hybrid approach are summarized in Fig. 4.2, showing the numerically obtained power law exponent of the CP potential against of the distance between a ^{87}Rb atom and the long symmetry axis of the nanofiber. The dielectric properties of the nanofiber are adapted from Ref. [Bla05] and shown in Fig. 4.1. Calculations have been done for three different planes, displaced from the substrate by $5\,\mu$m (green curve), $7\,\mu$m (red curve), and $9\,\mu$m (blue curve) (see inset in Fig. 4.2). The dependence of the exponent on the atom-nanofiber separation for the three planes will, first, differ due to the varying nanofiber diameter, and second, due to the distance to the tip of the fiber. The influence of the latter finite size effect is, for example, visible in Fig. 4.2 for small distances between the atom and the nanofiber: while the green and the red curve approach the $1/d^3$ result for atoms in front of an infinite plane surface (non-retarded case, see Sec. 1.2), the blue curve, calculated close to the tip of the fiber shows a different behavior. The initial decrease and subsequent increase of all three curves is connected to the increasing influence of retardation effects for larger distances between the atom and the nanofiber. The wavelengths relevant for the transition from the non-retarded to the retarded regime are 780/794 nm for ^{87}Rb as assumed in the calculation.

The hybrid approach is suitable to do ab-initio calculations of the CP potential of the nanofiber. To approximate the experimental findings, it is desirable to have a simple power law for the CP potential, in particular, describing the potential correctly for atoms in a few hundred nanometer distance to the nanofiber. Moreover, the approximation should be applicable for different degrees of overlap between the nanofiber and the atom cloud, i.e. accounting for all contributing radial CP potential slopes. Considering the results summarized in Fig. 4.2, a potential of the form

$$U(r) = -\frac{C_5}{r^5}, \tag{4.1}$$

i.e. using a r^{-5} power law, appears to be a good compromise between complexity and accuracy. Note that r is the radial distance of the atom to the long symmetry axis of the nanofiber. However, it is clear from the discussion (this section and Sec. 1.2) that this model can only be regarded as a first approximation to the problem.

4.2 Atom Loss From a Magnetic Trap

Before making the connection between the dispersive nanofiber properties and the decay behavior of ultracold clouds, the loss of atoms from magnetic traps is briefly reviewed. To begin with, an overview of general loss mechanisms is given. Then, the atomic cloud decay due to the interaction with nanowires in the close proximity of the atoms is discussed.

4.2.1 Mechanisms

The literature considers the loss of atoms from a trap in various contexts. There are two obvious ways how atoms can get lost from a magnetic trap. This is either by a flip of the atomic spin into a non-trapped state, or by evaporation or tunneling due to insufficient (externally lowered) trap depth. Surely, both mechanisms can also contribute at the same time. The first effect applies, for example, to Majorana spin flips [Suk97], the deliberate induction of spin flips to out-couple atoms from a BEC to generate an atom laser [Hol96, Blo99, Hai05], and spin-flips in the proximity of solid-state bodies due to Johnson noise [Hen99, Sch99, Rek04, Sch05, Vog06].

Insufficient trap depth is the dominant loss process, e.g., for a BEC in a very shallow magnetic or optical trap [Gri00] and for the atomic cloud under the influence of trap-opening Casimir-Polder forces [Rei99, Har03, Lin04, Pas04, Hun10]. The loss of atoms due to background gas collisions is also due to a limited trap depth as the momentum transfer by thermal atoms is very large. The same applies to BEC-ion experiments, where a comparably hot ion transfers sufficient momentum to remove atoms from the trap [Zip10]. Furthermore, there can be additional (external) magnetic or optical potentials with different minima positions than the potential used for trapping. This can result in atom loss. One example for undesired magnetic fields are the so-called patch potentials which are discussed in detail in Sec. A.1.

Both loss mechanisms at the same time can occur when three-body collisions [Bur97, Cra07] are dominant, i.e. for very high atomic densities. When atoms (temporally) form a molecule due to the collision, the released binding energy can lead to a large momentum transfer and remove atoms from the trap. Moreover, the molecule can have a high-field-seeking spin state which also leads to atom loss from the trap.

4.2.2 Atom Loss and Nanowires / Nanocylinders

In Ref. [Fer07], an ultracold atom cloud is theoretically studied in a trap in the very proximity of a current-carrying single-wall carbon nanotube. The loss of atoms is discussed in the framework of thermally induced spin flips from the nanotube and in the context of CP forces. For the considered (9, 0) nanotube [Dre01], the spin-flip limited lifetime of atoms in the trap exceeds 1 s for trapping distances larger than 20 nm. As the fraction of atoms separated less than 20 nm from the nanofiber is negligible in the present experiment, spin flips shall play a minor role for the loss of atoms form the magnetic trap and will not be taken into account for the analysis of the BEC scattering measurements. This is done despite that the nanofiber in the present experiments differs from a (9, 0) nanotube. However, a rapid decrease of induced spin-flip rates with increasing atom-surface separation should be the case for any type of nanofiber.

In contrast to spin flips, the atom losses arising from CP forces are not negligible in Ref. [Fer07] and will be crucial for the analysis of the ultracold gas scattering data outlined in chapter 3 of this thesis. However, the suggested loss model from Ref. [Fer07] is not applicable to the present experimental situation. In the refer-

ence, the magnetic trap is assumed to be displaced from the minimum of the CP potential, leading to a lowering of magnetic trapping potential by CP forces as the trap approaches the nanofiber. Using the reduced trap depth, a tunneling lifetime is calculated in the WKB approximation. For the present scattering measurements, the minimum of the CP potential, i.e. the nanofiber, is located exactly in the center of the magnetic trap. The combined magnetic and CP potential has no local minimum as it is the case in Ref. [Fer07]. As a consequence, no trap depth is defined and, thus, the WKB calculation is not applicable.

In Ref. [Fin10], Fink et al. theoretically discuss the s-wave scattering of a polarizable atom on an absorbing nanowire. The authors take CP forces into account, in particular, assuming the nanowire to be a perfectly conducting cylinder. Following the lines of Ref. [Ebe07], only the non-retarded regime is taken into account. Fink et al. derive elastic scattering amplitudes and differential elastic scattering cross-sections. These results describe scattering in the sense of spatial redistribution of atoms. They easily can be adapted to find the (total) absorption cross section using the optical theorem in 2D [Ver84]. However, the elastic result from Ref. [Fin10] as well as the derived absorptive quantities diverge for $k \to 0$, i.e. for vanishing incoming velocity of the considered matter wave. This limitation prevents to directly apply the theory from Fink et al. to the present experimental situation.

4.3 Loss of Thermal Atoms on a Nanofiber: Theory and Application to Data

In the first central measurement presented in this thesis, an ultracold thermal atomic ensemble is partially overlapped with a vertically standing nanofiber. The number of remaining atoms in the trap is then measured in dependence of interaction time and relative overlap (see Sec. 3.2). To deduce geometric and dispersive properties of the nanofiber from these measurements, a microscopic theory of the totally inelastic scattering of ultracold thermal atoms is presented in the following.

4.3.1 Capture Radius of a (Nano)-Cylinder

The connection between the experimentally determined scattering rates, and geometric and CP properties of the fiber is made in two steps: First, the capture radius $R(v)$ of an attractive central potential is calculated. Second, the flow of atoms Φ through the (effective, capture-enhanced) nanofiber surface is derived. This atom flow quantitatively determines the atom loss from the trap.

Due to the rotational symmetry of the CP outlined in Sec. 4.1, calculations can be made in the two dimensions perpendicular to the long axis of the nanofiber. The situation to be discussed is sketched in Fig. 4.3 (a). An atom of mass m moves in the two-dimensional central field $V(r)$ with initial speed v (i.e. far away from the central potential) and impact parameter b. The potential representing the CP force is assumed to be of the form $V(r) = -C_\kappa/r^\kappa$, i.e. for $\kappa = 1$, this is the Kepler

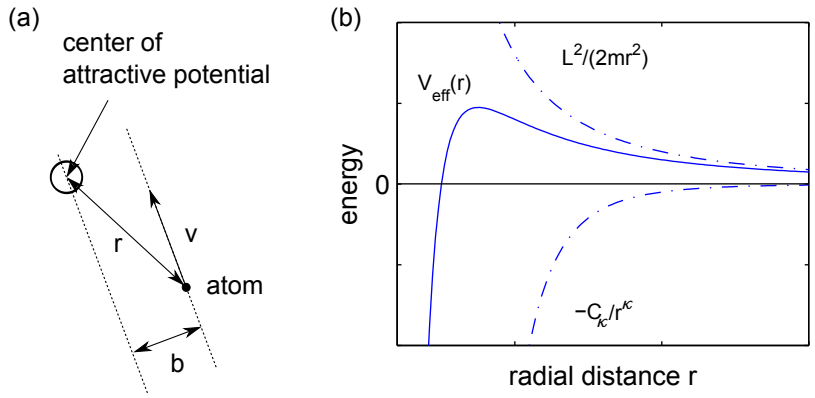

Figure 4.3: Atom capture in an attractive central potential. The situation is sketched in (a), showing an atom of initial speed v and mass m. It is propagating under an impact parameter b with respect to the potential center. It has to be emphasized that v refers to the speed of the atoms at large distances r between the central potential origin and the atom. In (b), the attractive central potential, the centrifugal energy (both shown as dash-dotted blue lines), and the resulting effective potential $V_{\text{eff}}(r)$ (solid blue line) are shown.

problem [Lan81]. However, in the following, only the cases $\kappa \geq 3$ are discussed. The actual value of κ can make a difference as, for example, there are no stable orbits for the atom for $\kappa > 2$ in contrast to the existence of stability regions for $\kappa < 2$ [Lan81, Den98]. Using two-dimensional polar coordinates $x = r\cos\varphi$ and $y = r\sin\varphi$, the sum of kinetic and potential energy of the atom can be written as

$$E = \frac{1}{2}m\dot{r}^2 + \frac{1}{2}mr^2\dot{\varphi}^2 + V(r) \tag{4.2}$$

$$= \frac{1}{2}m\dot{r}^2 + \underbrace{\frac{L^2}{2mr^2} + V(r)}_{V_{\text{eff}}(r)} \tag{4.3}$$

with $L = mvb = mr^2\dot{\varphi}$ being the angular momentum of the atom with respect to the potential center. The effective potential $V_{\text{eff}}(r)$ is shown schematically in Fig. 4.3 (b) as solid blue line. This function has a local maximum which is relevant for the atom capture. Considering $V(r) = -C_\kappa/r^\kappa$, its respective position and value are found to be

$$r_{\max} = \left(\frac{\kappa C_\kappa m}{L^2}\right)^{\frac{1}{\kappa-2}} \tag{4.4}$$

$$V_{\text{eff}}(r_{\max}) = \frac{1}{2}C_\kappa(\kappa-2)\left(\frac{L^2}{\kappa C_\kappa m}\right)^{\frac{\kappa}{\kappa-2}}. \tag{4.5}$$

When the initial kinetic energy of the atoms (i.e. for $r \to \infty$) is sufficient to overcome the effective potential energy barrier, atoms approaching the central potential are pulled into it. The CP potential of the nanofiber will lead to an acceleration of atoms until they reach the nanofiber surface. Atoms colliding with the latter can

experience at least two phenomena. It can be assumed that the atom's spin state is changed during the collision. In addition, the atom will be subject to a large momentum transfer from the comparably hot nanofiber. Both mechanisms lead to atom loss from the magnetic trapping potential. Furthermore, the atoms can be, in principle, adsorbed by the nanofiber which also leads to losses from the magnetic trap. Thus, it is instructive to calculate the nanofiber's capture radius for atoms at initial speed v. Setting

$$V_{\text{eff}}(r_{\max}) = \frac{1}{2}mv^2 \tag{4.6}$$

and substituting $L = mvb_c$, the critical impact parameter b_c is found to be

$$b_c = \left(\frac{A_\kappa}{v}\right)^{\frac{2}{\kappa}} \quad \text{for } \kappa > 2 \text{ with} \tag{4.7}$$

$$A_\kappa = \sqrt{\frac{C_\kappa}{m}(\kappa-2)}\left(\frac{\kappa}{\kappa-2}\right)^{\frac{\kappa}{4}}. \tag{4.8}$$

If an atom with initial speed v approaches the central potential at an impact parameter $b < b_c$, it is captured and falls into the center of the potential. Otherwise, i.e. for $b > b_c$, the atom is elastically scattered.

For the capturing of atoms by the nanofiber, this means that the effective totally inelastic scattering radius is the sum of the geometric (cylinder) radius and the capture radius due to the attractive CP potential. The effective scattering radius, hence, depends on the speed of the atom and is given by

$$R(v) = R_0 + \left(\frac{A_\kappa}{v}\right)^{\frac{2}{\kappa}} \quad \text{for } \kappa > 2 \tag{4.9}$$

with R_0 being the geometric radius. Solving Eq. 4.9 for v gives the capture velocity v_{cap} at R:

$$v_{\text{cap}}(R) = \frac{A_\kappa}{(R-R_0)^{\kappa/2}}. \tag{4.10}$$

Atoms at R with initial velocity $v < v_{\text{cap}}$ will be pulled into the potential whereas the atoms with $v > v_{\text{cap}}$ are elastically scattered.

4.3.2 Effective Radius and Capture Rate

To model the thermal cloud experimental data, a classical approach is used describing the atomic losses by a continuous flow of atoms onto the nanofiber surface. The starting point for the derivation is the phase-space-density $\rho(\vec{r}, \vec{v})$ of a Boltzmann distributed thermal gas in a 3D harmonic trap (located at (0, 0, d)) at temperature

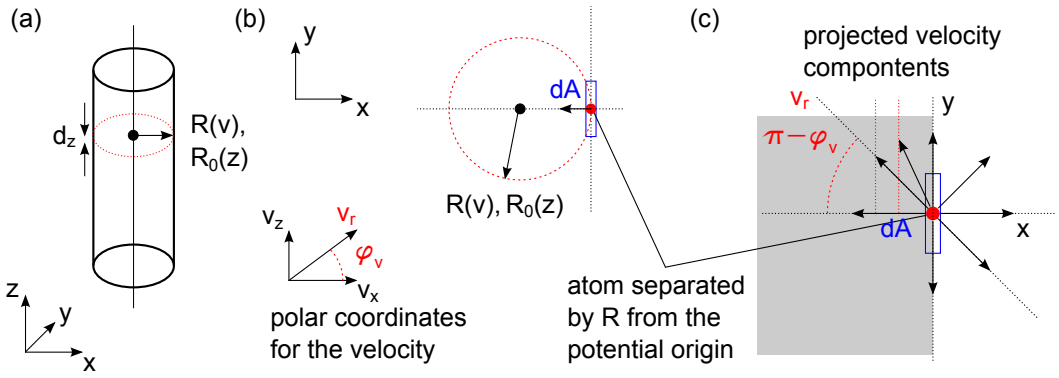

Figure 4.4: Illustrations supporting the derivation of the connection between the measured totally inelastic scattering rate and the C_κ coefficient of the nanofiber. Subfigure (a) introduces the coordinate system for the derivation, the relevant radii, and the surface element $2\pi R\, d_z$. In (b), the polar decomposition of the velocity vector is shown as well as the surface element dA. Subfigure Fig. (c) is to support the calculation of the net flow of atoms through a surface, accounting for an isotropic atom velocity distribution.

T and total atom number N [Lan80]:

$$\rho(\vec{r},\vec{v}) = \frac{N}{(2\pi)^3\sigma_x\sigma_y\sigma_z\sigma_v^3}\exp\left(-\frac{x^2}{2\sigma_x^2}-\frac{y^2}{2\sigma_y^2}-\frac{(z-d)^2}{2\sigma_z^2}-\frac{v_x^2+v_y^2+v_z^2}{2\sigma_v^2}\right) \tag{4.11}$$

with d being the separation of the cloud from the chip surface as used in chapter 3 and

$$\sigma_i = \sqrt{\frac{k_B T}{m\omega_i^2}} \quad \text{for} \quad (i = x, y, z) \tag{4.12}$$

$$\sigma_v = \sqrt{\frac{k_B T}{m}}. \tag{4.13}$$

Generally, the infinitesimal single-velocity particle flow through a surface element $d\vec{A}$ at $\vec{r}$ is given by

$$d^5\Phi = \rho(\vec{r},\vec{v})\ |\vec{v}\cdot d\vec{A}|\ dv_x dv_y dv_z \tag{4.14}$$

with $\vec{v}\cdot d\vec{A} = |\vec{v}|\cdot|d\vec{A}|\cdot\cos\measuredangle(\vec{v}, d\vec{A})$ the scalar product between the velocity vector and the surface normal. This accounts for the fact that only the atomic velocity perpendicular to the surface contributes to the flow.

The further calculation uses the coordinate system shown in Fig. 4.4 (a). Atomic velocity components along the z-direction (i.e. along the long axis of the nanofiber) will not contribute to the flow onto the nanofiber. The v_z velocity component in Eq. 4.11 can, thus, be integrated out. For the infinitesimal number of atoms in the

phase space volume element $d\vec{r}d\vec{v}$, it follows

$$\rho(\vec{r},\vec{v})\; d\vec{r}d\vec{v} = n(\vec{r})d\vec{r}\frac{1}{(2\pi)^{3/2}\sigma_v^3}\exp\left(-\frac{v_x^2+v_y^2+v_z^2}{2\sigma_v^2}\right)dv_xdv_ydv_z \tag{4.15}$$

$$\rho(\vec{r},v_x,v_y)\; d\vec{r}\,dv_xdv_y = n(\vec{r})d\vec{r}\;\frac{1}{2\pi\sigma_v^2}\exp\left(-\frac{v_x^2+v_y^2}{2\sigma_v^2}\right)dv_xdv_y. \tag{4.16}$$

The quantity $n(\vec{r})$ is the density distribution for a thermal cloud in a harmonic trap [Lan81, Wac05]. It is given by

$$n(\vec{r}) = \iiint \rho(\vec{r},\vec{v})\; dv_xdv_ydv_z \tag{4.17}$$

$$= \frac{N}{(2\pi)^{3/2}\;\sigma_x\sigma_y\sigma_z}\;\exp\left(-\frac{x^2}{2\sigma_x^2}-\frac{y^2}{2\sigma_y^2}-\frac{(z-d)^2}{2\sigma_z^2}\right). \tag{4.18}$$

The remaining velocity components v_x and v_y in Eq. 4.16 are transformed into polar coordinates (see Fig. 4.4 (b)) in the following way

$$v_x = v_r\cos\varphi_v \tag{4.19}$$

$$v_y = v_r\sin\varphi_v \tag{4.20}$$

$$v_r^2 = v_x^2+v_y^2. \tag{4.21}$$

It should be emphasized that v_r is not the radial component of the velocity but the vector sum of the Cartesian velocity components v_x and v_y. The coordinate transformation leads to the following expression for the fraction of atoms in the infinitesimal phase space element $\rho d\vec{r}dv_rd\varphi_v$:

$$\rho(\vec{r},v_r,\varphi_v)\; d\vec{r}\,dv_rd\varphi_v = n(\vec{r})d\vec{r}\;\frac{1}{2\pi\sigma_v^2}\exp\left(-\frac{v_r^2}{2\sigma_v^2}\right)v_rdv_rd\varphi_v. \tag{4.22}$$

Using this distribution, the particle flow through a surface element $d\vec{A}$ at $\vec{r}$ can be derived using Eq. 4.14. For the evaluation of the scalar product, the orientation of the surface element $d\vec{A}$ in the latter equation is important. It is given by the surface normal $d\vec{A}/|d\vec{A}|$. As the velocity distribution is isotropic, the velocity with absolute value v_r can have any orientation in the x-y-plane. In Fig. 4.4 (b) and (c), the calculation of the velocity contribution perpendicular to a surface element $d\vec{A}$ is illustrated. From the total magnitude v_r, only the fraction $v_r\cos(\pi-\varphi_v)$ contributes to the flow onto $d\vec{A}$, the term $(\pi-\varphi_v)$ being the angle between the flow velocity vector and the surface normal (see Fig. 4.4 (c)). Using the phase-space density from Eq. 4.22 and the equation for the flow 4.14 with $|\vec{v}\cdot d\vec{A}| = v_r|d\vec{A}|\cos(\pi-\varphi_v)$, the

flow through $d\vec{A}$ located at $\vec{r}$ results to

$$d^4\Phi = n(\vec{r})\ dA\ \frac{v_r^2}{2\pi\sigma_v^2} \exp\left(-\frac{v_r^2}{2\sigma_v^2}\right)\ dv_r d\varphi_v \tag{4.23}$$

$$d^3\Phi = n(\vec{r})\ dA\ \frac{v_r^2}{2\pi\sigma_v^2} \exp\left(-\frac{v_r^2}{2\sigma_v^2}\right)\ dv_r \underbrace{\int_{\pi/2}^{3/2\pi} \cos(\pi-\varphi_v) d\varphi_v}_{2} \tag{4.24}$$

$$d^3\Phi = n(\vec{r})\ dA\ \frac{v_r^2}{\pi\sigma_v^2} \exp\left(-\frac{v_r^2}{2\sigma_v^2}\right)\ dv_r \tag{4.25}$$

$$|d\vec{A}| = dA. \tag{4.26}$$

By choosing the respective surface element dA, Eq. 4.25 allows to calculate both the atom flow onto the geometric nanofiber surface and the loss of atoms due to an additional attractive central potential. In the following calculation of the atom flow, the atomic density $n(\vec{r})$ will be assumed to be constant in the x-y-plane proximity of the nanofiber, i.e. $n(\vec{r}) = n(0,0,z)$. For the integration over the geometric nanofiber surface, this assumption is well justified as the nanofiber diameter is typically much smaller than the x-y-plane extent of the cloud. As shown in Eq. 4.9, the capture radius for the flow of atoms onto the nanofiber can be effectively increased due to CP forces. The validity of the local density approximation also for the effective radius will be discussed at the end of the derivation.

Using Eq. 4.25, first, the atom flow towards the nanofiber in the absence of attractive CP forces is discussed. The geometry-related atom flow $d\Phi_{\mathrm{geo}}(z)$ through a girthed area of circumference $2\pi R_0(z)$ and height dz can be obtained by integrating Eq. 4.25 with dA chosen to be $R_0(z)d\varphi dz$. For the flow $d\Phi_{\mathrm{geo}}(z)$ it follows

$$d\Phi_{\mathrm{geo}}(z) = n(z)\ dz\ \frac{R_0(z)}{\pi\sigma_v^2} \int_0^{2\pi} \underbrace{\int_0^{\infty} v_r^2 \exp\left(-\frac{v_r^2}{2\sigma_v^2}\right)\ dv_r}_{\sqrt{\frac{\pi}{2}}\sigma_v^3}\ d\varphi \tag{4.27}$$

$$= n(z)\ dz\ \sqrt{2\pi}\ R_0(z)\ \sigma_v. \tag{4.28}$$

In the calculation above, at each element $R_0(z)d\varphi dz$, the local flow of atoms to the nanofiber is calculated and integrated over the surface $2\pi R_0 dz$. When integrated over z, Eq. 4.28 describes the total flow of a harmonically trapped thermal cloud onto a rotationally symmetric object with a geometry described by $R_0(z)$.

The method applied to calculate the purely geometry-related flow can be adapted for the calculation of the flow to the nanofiber surface due to attractive CP forces. The second summand in Eq. 4.9 describes the effective additional nanofiber radius, i.e. $(A_\kappa/v_r)^{2/\kappa}$, for atoms of velocity v_r. The latter is the initial atomic velocity. Using Eq. 4.25, the velocity-dependence of the effective nanofiber radius leads to a different integrand for the integral over dv_r compared to the geometric case. With the surface element chosen to be $dA = dz(A_\kappa/v_r)^{2/\kappa}d\varphi$, the CP-related flow

$d\Phi_{\mathrm{CP}}(z)\,dz$ is given by

$$d\Phi_{\mathrm{CP}}(z) = \int_0^{2\pi}\int_0^{\infty} n(z)dz\,\frac{1}{\pi\sigma_v^2}\left(\frac{A_\kappa}{v_r}\right)^{2/\kappa} v_r^2 \exp\left(-\frac{v_r^2}{2\sigma_v^2}\right)\,dv_r d\varphi \tag{4.29}$$

$$= n(z)dz\,\frac{2\pi}{\pi\sigma_v^2}\,(A_\kappa)^{2/\kappa}\underbrace{\int_0^{\infty} v_r^{2-2/\kappa}\exp\left(-\frac{v_r^2}{2\sigma_v^2}\right)\,dv_r}_{2^{1/2-1/\kappa}\,\sigma_v^{3-2/\kappa}\,\Gamma\left(3/2-1/\kappa\right)} \tag{4.30}$$

$$= n(z)dz\,(A_\kappa)^{2/\kappa}\,2^{3/2-1/\kappa}\,\sigma_v^{1-2/\kappa}\,\Gamma\left(3/2-1/\kappa\right) \tag{4.31}$$

with Γ being the Gamma function. The latter equation connects the flow $d\Phi_{\mathrm{CP}}(z)$ with the coefficient A_κ. This means, Eq. 4.31 quantitatively relates the atom loss on the nanofiber to the strength of the CP potential of the nanofiber. As $A_\kappa \propto \sqrt{C_\kappa}$, the flow $d\Phi_{\mathrm{CP}}$ is proportional to $\sqrt[\kappa]{C_\kappa}$. Moreover, $d\Phi_{\mathrm{CP}}$ and also the non-infinitesimal flow Φ_{CP} are related to the speed σ_v and the temperature T as

$$\Phi_{\mathrm{CP}} \propto \sigma_v^{1-2/\kappa} \tag{4.32}$$

$$\Phi_{\mathrm{CP}} \propto T^{1/2-1/\kappa}. \tag{4.33}$$

This results, for example, for $\kappa = 5$ in the dependencies $\Phi_{\mathrm{CP}} \propto \sigma_v^{3/5}$ and $\Phi_{\mathrm{CP}} \propto T^{3/10}$.

The expression in Eq. 4.31 has been obtained under the assumption of a locally constant atomic density. The validity of this simplification is discussed in the following. In Eq. 4.31, for each v_r, there is a corresponding radius at which this velocity class is captured by the attractive CP potential. As seen from Eq. 4.10, the number of captured velocity classes rapidly decreases with the distance R between the atom and the origin of the attractive potential. The captured fraction of atoms Θ due to CP forces can be calculated using the velocity distribution of v_r. For Θ, it follows

$$\Theta(R) = \int_0^{v_{\mathrm{cap}}(R)} \frac{1}{\sigma_v^2} v_r \exp\left(-\frac{v_r^2}{2\sigma_v^2}\right)\,dv_r \tag{4.34}$$

$$\text{with the normalization}\quad 1 = \int_0^{\infty} \frac{1}{\sigma_v^2} v_r \exp\left(-\frac{v_r^2}{2\sigma_v^2}\right)\,dv_r. \tag{4.35}$$

The resulting dependence is shown in Fig. 4.5. The calculation has been made for typical parameters, i.e. a cloud temperature of 100 nK and $C_5 = 1 \times 10^{-65}\,\mathrm{Jm}^5$. For these conditions, in a distance of 1 μm, only $\approx 8 \times 10^{-5}$ atoms from the total distribution will be pulled into the CP potential. The extent of the cloud at 100 nK for typical trap frequencies results to cloud extents σ_i (see Eq. 4.12) on the order of several to several ten micrometers. Consequently, the comparatively rapid decay in the number of captured atoms with the distance to the origin of the attractive potential justifies the local density approximation made at the beginning of the derivation of the atomic flow Φ. At distances R where the assumption of a constant cloud density losses its validity, the contributions to the CP-enhanced flow of atoms to the nanofiber are negligible.

To obtain the total (non-differential) flow Φ onto the nanofiber, the geometric and

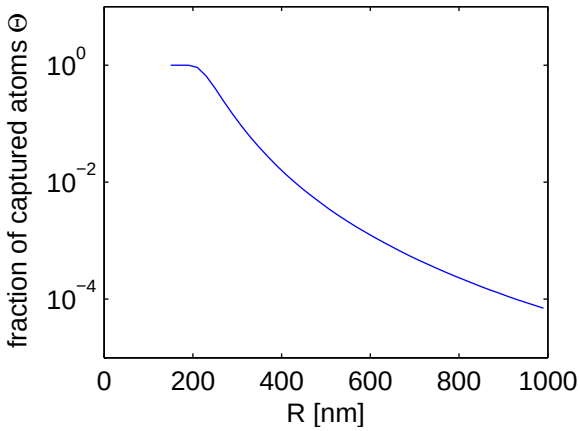

Figure 4.5: The fraction of CP-captured atoms is shown against the radial position R of the considered atoms with respect to the origin of the attractive CP potential. The calculation is done for a cloud temperature $T = 100\,\mathrm{nK}$ and $C_5 = 1 \times 10^{-65}\,\mathrm{Jm}^5$. For R smaller $\approx 200\,\mathrm{nm}$, all atoms are captured. Otherwise, the fraction of captured atoms decreases rapidly to about 8×10^{-5} at $R = 1\,\mu\mathrm{m}$.

the CP contribution have to be added and integrated along the long axis of the nanofiber z. If the height of the nanofiber is h_{NF}, it follows that Φ and the respective change $-\dot{N}$ of the number of atoms in the trap are given by

$$\Phi = -\dot{N} = \int_0^{h_{\mathrm{NF}}} \left(\Phi_{\mathrm{geo}}(z) + \Phi_{\mathrm{CP}}(z)\right)\, dz. \tag{4.36}$$

In both summands, the cloud density $n(z)$ appears which is proportional to the total atom number N. Thus, the total flow Φ has the same proportionality. The differential equation 4.36 for $\dot{N}$ is simply solved by a single-exponential decay, yielding the single-particle decay rate $\gamma = \Phi/N$. This description is valid as long as the distributions σ_v and σ_i do not change during the considered atom loss. In particular, the model is applicable when the cloud temperature and the trap frequencies are constant during the observed nanofiber-cloud interaction.

Formula 4.36 describes the loss of atoms from a magnetic trap due to a flow of atoms to an immersed nanofiber (or any other object with rotational symmetry). If the cloud properties as well as the geometry of the nanofiber are known, the Casimir-Polder potential of the fiber in the $-C_\kappa/r^\kappa$ approximation can quantitatively be derived from the measurements. The height as well as the radius $R_0(z)$ of the nanofiber in dependence of the position along the long nanofiber axis are precisely known from SEM images as outlined in Sec. 3.1. The theory is limited to small density variations of the cloud over the nanofiber diameter and negligible quantum reflection of atoms on the central potential. The result in Eq. 4.36 is applied in the following.

4.3.3 Thermal Loss Data and Nanofiber Casimir-Polder Potential

To connect the thermal cloud decay data and the dispersive properties of the nanofiber, the rates γ_2 from Sec. 3.2 act as a starting point. The results for γ_2 are shown in Fig. 3.7 and potted as blue crosses in case of the reference measurement. The red circles represent the measurement over the nanofiber. The latter rates account for the combined loss of atoms from the trap due to both the nanofiber and the substrate, on which the nanofiber stands. To apply the theory derived in Sec. 4.3.2, this combined scattering rate is subtracted by the γ_2 reference value, measured above the plain substrate to yield the pure, nanofiber-limited loss. This subtraction is justified as the rates are obtained for equal temperatures of the cloud, equal trap-surface separations d, and equal trap frequencies. In particular, this means the measurements are taken for equal distributions σ_v and σ_i (see Sec. 4.3.2).

The resulting difference rates $\gamma_{2,\,\mathrm{diff}}$ are plotted over the trap-surface separation d in Fig. 4.6 as green triangles. As the overlap between the nanofiber and the ultracold thermal cloud increases with decreasing d, an increase in $\gamma_{2,\,\mathrm{diff}}$ is expected. The $\gamma_{2,\,\mathrm{diff}}$ data confirms this and provides a basis to conclude dispersive properties of the nanofiber from the measurements. It shall be recalled that the cloud temperature for this measurement is around 100 nK and below (for values, see Fig. 3.6). According to Eq. 4.13, this corresponds to typical atom velocities of $\approx 3\,\mathrm{mm/s}$. At these velocities, the quantum reflection probability of atoms on the nanofiber potential is much below 1% [Jud10a]. The axial and radial extent of the cloud (σ_a and σ_r) is much larger than the diameter of the nanofiber (see Secs. 3.2 and 3.1). The restriction of the analysis to the γ_2-dominated part of the atomic decay ensures an approximately constant cloud temperature during the considered nanofiber-cloud interaction. These are necessary criteria for the application of the model from Sec. 4.3.2.

The nanofiber's geometric as well as dispersive contributions to the decay in the atom number can be studied individually. Using the detailed geometry data provided in Fig. 3.3 and the temperatures plotted in Fig. 3.6, the geometry-related loss rates can be calculated with Eq. 4.36 setting A_κ in Φ_{CP} to zero. Thus, the atom loss due to attractive CP forces is neglected in the formula and only the geometric cross section of the nanofiber contributes to the loss. The resulting geometric rate is plotted as solid black line in Fig. 4.6. A comparison of the geometric model and the measurement clearly reveals a "super-geometric" decay in the experimental data.

As discussed, the atom loss can be enhanced due to attractive CP forces from the nanofiber. Using the full form of Eq. 4.36 with $\kappa = 5$ in Eq. 4.31, the data is fitted and dispersive properties are extracted from the measurements. Using the temperatures from Fig. 3.6, a least-squares minimization varying C_5 results in the solid green fit. The curve resembles the data much better than the geometric fit. The obtained C_5 coefficient is found to be $6 \times 10^{-65}\,\mathrm{Jm}^5$. Using a similar error estimation as outlined in Sec. 3.2 for the error of γ_2, bounds on the value of C_5 have been estimated. Within the framework of the model, it results $4 \times 10^{-66}\,\mathrm{Jm}^5 < C_5 < 6 \times 10^{-64}\,\mathrm{Jm}^5$. The fit curves corresponding to the error bounds are shown in Fig. 4.6 as dash-dotted green lines. The upper one corresponds to the $C_5 = 6 \times 10^{-64}\,\mathrm{Jm}^5$ bound, the lower one to a C_5 of $4 \times 10^{-66}\,\mathrm{Jm}^5$.

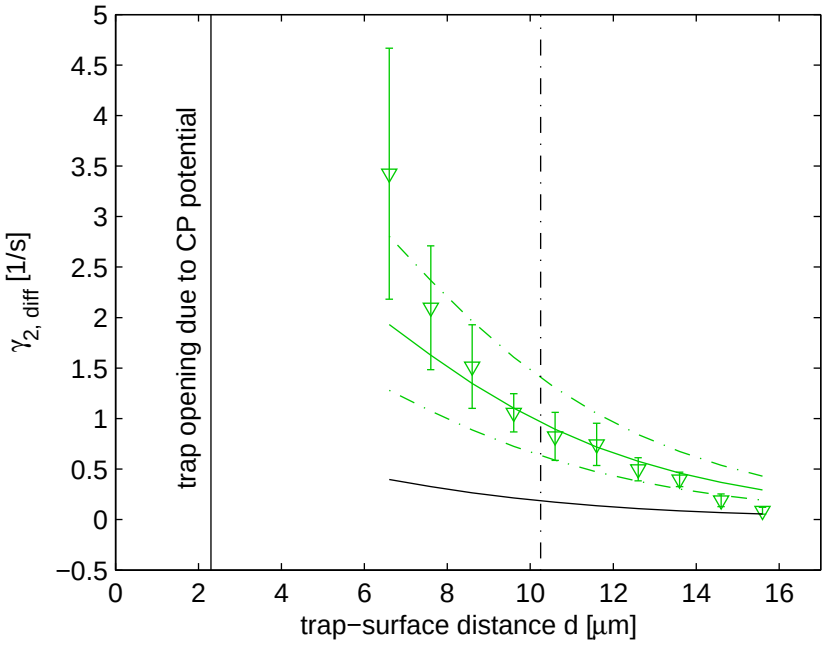

Figure 4.6: Nanofiber-limited loss rates $\gamma_{2,\,\mathrm{diff}}$ against trap-surface separation d. The dash-dotted vertical black line indicates the height of the nanofiber. The magnetic trap opening due to CP forces from the substrate is indicated with the solid vertical black line. Rates as derived from the experimental data from Sec. 3.2 are plotted as green triangles. For decreasing d, the overlap of the thermal cloud and the nanofiber increases, which leads to increasing rates $\gamma_{2,\,\mathrm{diff}}$. The black curve is a fit of the data, neglecting CP effects. The lines plotted in green include CP effects to account for the clearly "super-geometric" experimental losses. The solid green fit is a result of optimizing C_5 from Eq. 4.36 to approximate the experimental data. The two dash-dotted green lines indicate the resulting CP fits for the upper and lower error bound values of C_5.

4.4 Loss of BEC Atoms on a Nanofiber: Theory and Application to Data

After the discussion of the thermal atom loss on a nanofiber, this section evaluates the experimentally obtained BEC decay data. Modeling the decay of a Bose-Einstein condensate due to a partial overlap with an atom-absorbing nanofiber requires the calculation of the time-evolution of the BEC's wavefunction. This has to be done in the combined potential of the magnetic trap and the nanofiber, including the corresponding nanofiber CP potential.

4.4.1 Atom Loss on a Nanofiber using the Gross-Pitaevskii Equation

If the s-wave scattering length is much smaller than the average distance between the atoms and the number of atoms is much larger than one, a Bose-Einstein condensate can be described by the time-dependent Gross-Pitaevskii equation (GPE) [Dal99]. In general, the GPE is given by

$$i\hbar\frac{\partial}{\partial t}\Psi(\vec{r},t) = \left(-\frac{\hbar^2\nabla^2}{2m} + V_{\text{ext}}(\vec{r}) + g|\Psi(\vec{r},t)|^2\right)\Psi(\vec{r},t) \tag{4.37}$$

$$g = \frac{4\pi\hbar^2 a}{m} \tag{4.38}$$

with a being the s-wave scattering length, g the coupling constant, and m the mass of one atom. For ^{87}Rb, a is 5.77 nm [Dal99] and $m = 1.443 \times 10^{-25}$ kg [Ste09]. The GPE describes the dynamics of the condensate wavefunction $\Psi(\vec{r},t)$ in a given external potential $V_{\text{ext}}(\vec{r})$. The normalization of $\Psi(\vec{r},t)$ connects the wave function to the total atom number N in the condensate. To describe the atom-absorbing nanofiber immersed in the BEC, the potential V_{ext} can contain a complex-valued part. This is present in addition to the real part of V_{ext} which accounts for the combined magnetic-CP potential (with the CP potential e.g. in the form suggested in Eq. 4.1). The complex component of V_{ext} damps the condensate wave function and, thus, can be used to simulate the loss of atoms from the BEC. Another option to model the BEC decay is a conditioned renormalization of the wave function.

Modeling the BEC scattering problem with the GPE is a powerful method. However, it is quite involved: The numerical effort to solve the GPE in three dimensions with high temporal and spatial resolution makes it hard to deal with the intrinsic inverse nature of every fitting procedure: to approximate the data, a (complex) external potential $V_{\text{ext}}(\vec{r})$ needs to be assumed first, then the GPE has to be solved and, finally, the resulting time dependence of the BEC atom number in the trap has to be compared with the experimental findings. Thus, the potential can iteratively be optimized to make the simulated decay matching the measured one. However, each iteration requires a time-consuming simulation. Moreover, while the choice of the real part of V_{ext} is clear (the sum of the magnetic trapping and the CP potential), the construction and physical interpretation of the complex part of the external potential is non-trivial [Mug04]. When a renormalization of the wave function is used, a criterion has to be found to determine by how much the atom number is reduced per unit time.

Application of the GPE to the Nanofiber Problem

A simplified example calculation for one time-resolved BEC atom loss due to an immersed nanofiber has been provided by Prof. Th. Judd, Institute of Physics, University of Tübingen. The nanofiber completely sticks through the BEC, and the initial atom number is set to be 7590. These values correspond to one experimen-

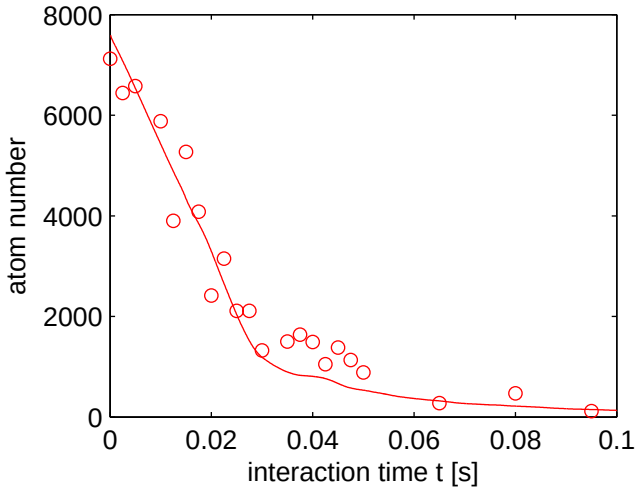

Figure 4.7: GPE simulation of the decay dynamics of a BEC overlapping with a nanofiber. The experimental trap-surface distance d is 7.65 μm. For the latter value of d, the nanofiber is completely sticking through the BEC. The numerical solution of the GPE approximates well the experimental data. The curvature of the simulated decay $N(t)$, interestingly, is not monotonous, indicating a complex decay dynamics.

tally obtained dataset. To limit the numerical effort for the calculation, the trap frequencies in the directions radial to the long axis of the nanofiber have been set equal. In contrast to 80 Hz and 17 Hz, a geometrical average, resulting to 37 Hz is assumed in both directions. The CP potential is chosen to be described by a C_5 coefficient of 5×10^{-63} Jm^5. Concentric to the cylindrically symmetric CP potential, there is a "cutoff cylinder" with a radius of 300 nm assumed for the calculations. The wave function is renormalized according to the fraction of the wave function which has propagated beyond the cutoff due to the CP attraction. This accounts for the fact that atoms from the cloud are lost before they can propagate into the nanofiber volume.

The results of the GPE simulation are shown in Fig. 4.7, plotting the number of atoms against interaction time. The loss curve obtained from the GPE approximates well the experimental data (red circles). Nonetheless, these results have to be considered preliminary as the implementation of the cutoff does not yet represent the exact nanofiber geometry. In the simulation results, the number of atoms is monotonically decreasing. However, the curvature of $N(t)$ is not monotonous, i.e. at $t \approx 0.04$ s, the steepness of the decay decreases and, then, increases again.

This behavior can be understood considering the time-evolution of the density distribution of the BEC. A snapshot of the simulated BEC dynamics has been taken for $t = 24$ ms and is shown in Fig. 4.8. The nanofiber symmetrically sticks though the atomic cloud. The density of the BEC is zero at the position of the nanofiber. This is because the BEC cannot propagate into the volume occupied by the latter. In addition, the nanofiber "impurity" causes density waves, which travel through the condensate over time. As a consequence, the density in the very proximity

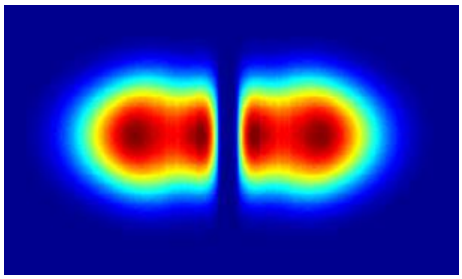

Figure 4.8: Snapshot of the BEC dynamics from Fig. 4.7 taken at $t = 24\,\mathrm{ms}$. The nanofiber symmetrically sticks though the quantum-degenerate gas. The latter shows a complex motion: the presence of the nanofiber causes density waves traveling inside the BEC. They are the reason for the varying curvature of the BEC decay $N(t)$.

of the nanofiber surface can decrease and increase again, which explains the non-monotonous curvature of atomic decay visible in Fig. 4.7.

The GPE simulations further show that the attractive CP potential locally causes a drag of BEC atoms towards the nanofiber. An estimate proportional to this drag is given by the gradient of the BEC's phase $S(\vec{r},t)$, i.e. the potential flow velocity v_{pot} [Dal99, Kur07]

$$\Psi(\vec{r},t) = \sqrt{n(\vec{r},t)}\exp(iS(\vec{r},t)) \tag{4.39}$$

$$v_{\mathrm{pot}}(\vec{r},t) = \frac{\hbar}{m}\nabla S(\vec{r},t) \tag{4.40}$$

$$= \frac{\hbar(\Psi^*(\vec{r},t)\nabla\Psi(\vec{r},t) - (\nabla\Psi^*(\vec{r},t))\Psi(\vec{r},t))}{2mi|\Psi(\vec{r},t)|^2}. \tag{4.41}$$

Here, $n(\vec{r},t) = |\Psi(\vec{r},t)|^2$ is the local density of the condensate. It is important to note that v_{pot} is different from the speed of sound v_s of the BEC which is given by

$$v_s(\vec{r},t) = \sqrt{\frac{gn(\vec{r},t)}{m}} \tag{4.42}$$

$$\bar{v}_s = \sqrt{\frac{gn_{\max}}{2m}}. \tag{4.43}$$

The (generally spatially dependent) speed of sound describes, how fast small density perturbations propagate within the BEC. The averaged speed of sound $\bar{v}_s$ is common in the literature [Ket99]. The potential flow velocity has a hydrodynamic character and is connected to a net mass flow of the condensate. Interestingly, when $v_{\mathrm{pot}} > v_s$, a "sonic horizon" can be formed in the Bose-Einstein condensate, having analogies to horizons in the context of black holes in astrophysics [Gar00, Gar01, Leo03, Kur07, Bar07].

4.4.2 Flow of a BEC onto a Nanofiber

The decay of the BEC due to the interaction with an immersed nanofiber must be a result of a net flow Φ of atoms onto the nanofiber surface. Consequently, it is

$$\dot{N}(t) = -\Phi(t). \tag{4.44}$$

As seen in Sec. 4.3.2, the calculation of a flow Φ requires the knowledge of the atomic density distribution, the velocity distribution, and the relevant surface for the integration. GPE simulation results show that already the density distribution of the atomic cloud in the presence of an immersed nanofiber can be non-trivial as depicted in Fig. 4.8.

For a BEC in an undisturbed (i.e. without nanofiber) harmonic potential, a simple analytic form for the density distribution of the BEC can be derived from the stationary GPE [Dal99]. If the kinetic energy term can be neglected, as it is the case for the present experimental situation, the density of the BEC is described by the Thomas-Fermi approximation. It is given by [Ket99]

$$n(\vec{r}) = \max\left(\frac{\mu - V_{\text{ext}}}{4\pi\hbar^2 a/m}, 0\right) \tag{4.45}$$

$$= \frac{15}{8\pi}\frac{N}{\prod_i r_{\text{TF, i}}} \max\left(1 - \sum_{i=1}^{3}\frac{x_i^2}{r_{\text{TF, i}}^2},\ 0\right) \tag{4.46}$$

$$r_{\text{TF, i}} = \sqrt{\frac{2\mu}{m\omega_i^2}} \quad \text{for } i = (x, y, z) \tag{4.47}$$

with $r_{\text{TF, i}}$ being the Thomas-Fermi radii and μ the chemical potential. The latter is defined as [Ket99]

$$\mu = \frac{1}{2}\left(15\hbar^2 m^{1/2} N \bar{\omega}^3 a\right)^{2/5} \tag{4.48}$$

$$\bar{\omega} = \left(\prod_i \omega_i\right)^{1/3}. \tag{4.49}$$

The density distribution given in Eq. 4.45 could serve as a first approximation in a simplified calculation of the flow Φ onto the nanofiber. However, the Thomas-Fermi approximated density distribution neglects a possible reshaping of the BEC due to the presence of the nanofiber. The latter has been seen in Fig. 4.8. For the magnitude and sign of a BEC density camber due to the presence of the nanofiber, no closed analytical description is known. The effect is theoretically discussed for an attractive point (zero-dimension) impurity in a BEC [Bru08]. The latter reference, however, points out that the degree of BEC deformation strongly varies with system dimensionality as well as impurity-BEC interaction strength.

Recalling the discussion of the time-dependent GPE, the velocity relevant for the calculation of the flow Φ could be a potential flow velocity. A stronger attractive

potential of the nanofiber should lead to an increased drag of atoms towards the surface. However, Zipkes et al. [Zip10] argue that, in a similar context, "the characteristic speed at which the condensate density re-adjusts is the speed of sound". The latter statement is, by itself, unquestioned. However, this approach makes no connection to the coupling strength of the impurity to the BEC, i.e. the CP force in case of the nanofiber. The latter negligence needs, then, to be accounted for by a (CP modified) density distribution of the BEC and/or an effective integration surface (as it is done in Ref. [Zip10]). The latter approach is similar to the CP-enhanced effective capture radius discussed for a thermal cloud (see Sec. 4.3.2).

For very cold clouds, in principle, quantum reflection of atoms in the CP potential can take place. As CP potentials are very steep, the k vector of the ultracold cloud has to be very small for quantum reflection to be significant. According to Ref. [Jud10a], reflection on a nanofiber gets important for atom velocities smaller than 1 mm/s. A significant quantum reflection probability would result in an effectively reduced flux. The reflection of atoms on Casimir-Polder potential tails of a wall has been studied in detail in Ref. [Fri02]. It is shown that in the limit of small k, the reflection coefficient exponentially goes to one. For curved surfaces as it is the case for the nanofiber, the behavior can generally be more complicated [Arn07].

Despite open questions concerning the particular form of the individual contributions to the flow Φ, such a model provides an intuitive approach to understand the decay of the BEC due to the interaction with a nanofiber. In particular, a known or assumed expressions for the density, the atomic velocity, and the integration surface would allow to study the dependence of the loss dynamics on the overlap between BEC and nanofiber. In awareness of the discussion above, the experimental data presented in the following is approximated by a basic flow model.

4.4.3 BEC Loss Data and Casimir-Polder-Enhanced Nanofiber Capture Radius

The basis for the evaluation of geometric and CP effects of the nanofiber on the BEC decay are the single-exponential loss rates obtained in Sec. 3.3. Even if the effect of the substrate is negligible for most distances d, also for the BEC measurement, it is reasonable to subtract the rates γ obtained for the nanofiber and for the reference measurement (see Fig. 3.9). In analogy to the treatment from Sec. 4.3, the subtracted rates are denoted by γ_{diff}. The results of the subtraction are shown as green triangles in Fig. 4.9 and represent the purely nanofiber-limited loss. The data can be qualitatively interpreted in a similar way as in Fig. 3.9 for the non-subtracted BEC rates: The loss rate increases with increasing BEC-nanofiber overlap (i.e. for decreasing d).

The black crosses in Fig. 4.9 are the result of an approach to model the BEC loss analytically. To calculate a flow Φ, the Thomas-Fermi density distribution (Eq. 4.45) and the averaged speed of sound (Eq. 4.43) of the BEC have been integrated over the geometric surface of the nanofiber. As discussed in Sec. 4.4.2, this can be a non-negligible simplification to the problem. In Fig. 4.9, the resulting geometric

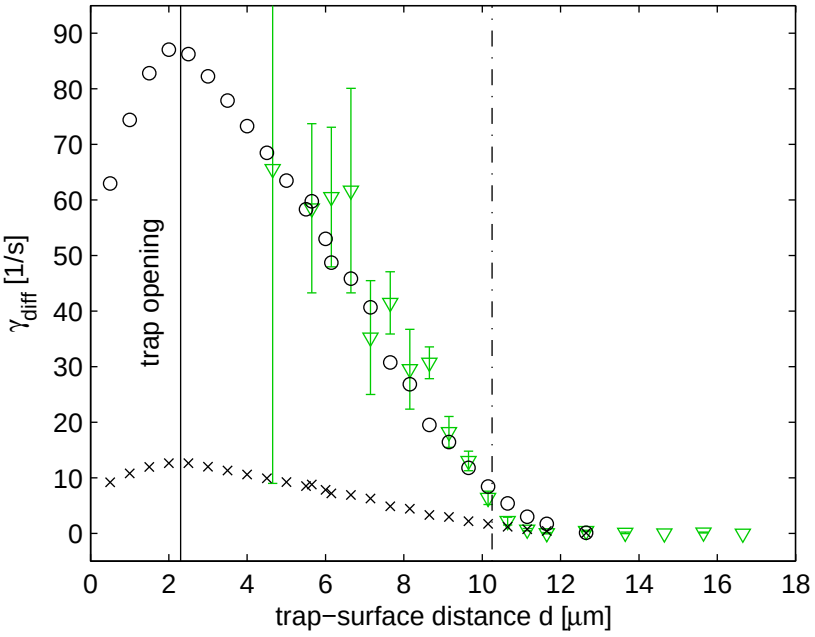

Figure 4.9: The experimentally obtained, purely nanofiber-limited decay rates of the Bose-Einstein condensate are shown as green triangles. A dash-dotted vertical black line indicates the height of the nanofiber. The magnetic trap opening due to CP forces from the substrate is indicated with the solid vertical black line. The substrate does not play a role for the rates γ_{diff}. However, the trap opening is indicated as it ultimately limits the experimentally accessible values of d. As expected, with increasing nanofiber-cloud overlap (i.e. for smaller d), γ_{diff} increases. The black crosses show the expected loss $\Phi/N(t = 0)$ using a simple model. The latter takes the speed of sound (Eq. 4.43), the Thomas-Fermi density distribution (Eq. 4.45), and the geometric nanofiber shape into account. The black circles indicate the expected loss due to a CP-enhanced scattering radius of the nanofiber.

flow divided by the initial atom number Φ/N is plotted. It is not obvious from the theory that this quantity is directly comparable with the single-exponential decay rate. However, the time-resolved measurements suggest a decay behavior close to single-exponential. The obtained loss from the geometric Thomas-Fermi calculation takes the nanofiber-cloud overlap correctly into account and increase with decreasing d as qualitatively expected. However, compared to the measured loss rates, the calculated rates are about a factor of seven to small.

To find a better approximation for the data, a CP-enhanced radius of the nanofiber can be assumed. The results of the calculation are shown as black circles in Fig. 4.9. Taking CP effects into account, the experimental data is approximated much better compared to the geometric fit. In the following, the underlying calculation is briefly outlined. In Ref. [Ebe09], the CP potential of a perfectly conducting cylindrical wire is discussed. In the limit of a wire radius R_0 being small compared to the distance between the atom and the wire surface, the CP potential scales as R_0^2. This means, the CP potential of a cylinder increases with increasing amount of "dispersion-force-generating" material as long as the exact curvature of the cylinder is not resolved

by the atom. This can be also assumed for the CP potential of the nanofiber. The dependence of the CP-enhanced (capture) radius for a given potential is not known for BEC atoms. In the $-C_\kappa/r^\kappa$ approximation, the capture radius was found to scale as $\sqrt[\kappa]{C_\kappa}$ for thermal atoms (see Eq. 4.9). The application of this result to the BEC has at least two problems: First, the capture radius has been derived for point particles and not for a matter wave as it is the case for the BEC. Thus, possible quantum interference effects are ignored. Second, the BEC resolves the different regimes of CP potential scaling along the long axis of the nanofiber much better than the thermal cloud due to its stronger localization. Consequently, changes in the power law exponent as discussed in Sec. 4.1 (for example at the tip of the fiber) are less averaged out as in the thermal case. In summary, the capture radius R_{cap} for the BEC will depend in an - for the present experimental situation - unknown way $R_{\mathrm{cap}}(R_0)$ on the the geometric radius R_0 of the nanofiber.

Even if the analytic form of $R_{\mathrm{cap}}(R_0)$ is not known, the capture radius $R_{\mathrm{cap}}(R_0)$ can be formally power-expanded around $R_0 = 50\,\mathrm{nm}$, which is the approximate geometric radius of the nanofiber in the middle of the measured interval of d (trap-surface distance). The expansion to first order results to

$$R_{\mathrm{cap}}(R_0)|_{50\,\mathrm{nm}} = R_{\mathrm{cap}}(50\,\mathrm{nm}) + K_1 \cdot (R_0 - 50\,\mathrm{nm}). \tag{4.50}$$

An expansion to higher orders can be made. However, with each order, another parameter arises and the problem - in terms of available data - rapidly becomes underdetermined. The parameters $R_{\mathrm{cap}}(50\,\mathrm{nm})$ and K_1 have been optimized to match the experimental scattering data, yielding $R_{\mathrm{cap}}(50\,\mathrm{nm}) = 250\,\mathrm{nm}$ and $K_1 = 7.8$. To achieve the latter, Φ/N is calculated using the sound velocity, the TF density distribution, and an area for the integration calculated using the CP-enhanced capture radius $R_{\mathrm{cap}}(R_0)$. The result of this analysis are the black circles plotted in Fig. 4.9. They are in very good agreement with the experimentally obtained loss rates (given as green triangles in Fig. 4.9).

Both calculations, the geometric and the CP-enhanced one, show that for very small trap-surface distances, the loss rate starts to decrease[3]. This is because the bottom of the nanofiber is located at a trap-surface distance of zero. As the purely nanofiber-limited loss is considered, the overlap between the cloud and the nanofiber decreases for small d. The loss rates are not symmetric to half the height of the nanofiber as the radius of the nanofiber at the bottom is larger than the radius at the top (see Fig. 3.3).

4.5 Discussion of Thermal and BEC Results

In the present thesis, Casimir-Polder effects of a single, free-standing nanofiber have evidently been observed by means of ultracold atoms. Two independent experiments, one with an ultracold thermal cloud and one with a Bose-Einstein conden-

[3]As the nanofiber in the experiment stands on a substrate, it is clear that this regime is not experimentally accessible.

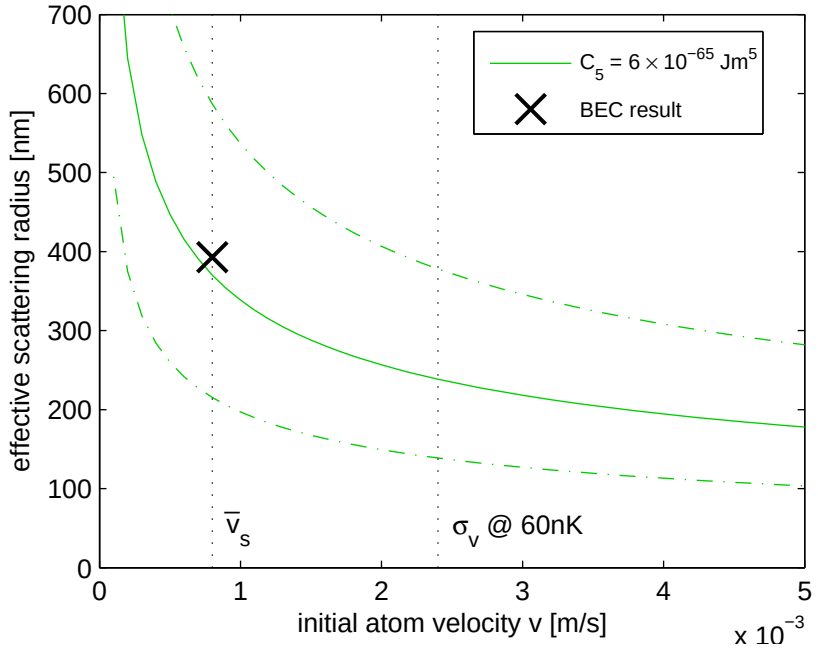

Figure 4.10: Velocity-dependent scattering behavior of the nanofiber as derived from the measurements. Using the C_5 coefficient $6 \times 10^{-65}\,\mathrm{Jm}^5$ as obtained from the thermal cloud data, the corresponding velocity-dependent scattering radius is shown as solid green line. The radii resulting from the corresponding error bounds are shown as dash-dotted green curves. For the BEC, only one data point (marked with a large black $\times$) is obtained, using the results presented in Sec. 4.4. As visible from the plot, the two independent measurements of the CP potential of the nanofiber are consistent with each other. Characteristic velocities, σ_v for the thermal cloud and the speed of sound $\bar{v}_s$ for the BEC, are given as vertical, dotted lines. The geometric nanofiber radius is not contained in the plot.

sate, have investigated the loss of atoms from a magnetic trap due to the absorptive interaction with a nanofiber. The decay of the atomic clouds has been studied in dependence of the degree of nanofiber-cloud overlap and interaction time. In both the thermal cloud and the BEC case, the measured losses are clearly "super-geometric", i.e. not explicable by solely considering the geometric volume of the nanofiber.

For the further evaluation of the experimental findings, CP effects of the nanofiber are taken into account. In case of the thermal cloud, the theory developed in Sec. 4.3.2 has been applied. Using a CP potential scaling of $\kappa = 5$ (see Sec. 4.1), a fit of the data from Sec. 4.3 has resulted in a CP coefficient C_5 of $6 \times 10^{-65}\,\mathrm{Jm}^5$. From this C_5 result, an effective scattering radius of the nanofiber can be calculated using Eq. 4.9. This quantity is velocity-dependent and shown in Fig. 4.10 as solid green line. The resulting effective scattering radii for the error bound C_5 values (see Sec. 4.3) are plotted as dash-dotted green lines. As expected, the capture radius decreases with increasing initial atom velocity. The characteristic atomic velocity σ_v for a typical cloud temperature (60 nK) is shown as vertical, dotted black line. An overview of all relevant temperatures of the measurement is given in Fig. 3.6. At σ_v, the capture radius of the nanofiber is found to be 240 nm, the lower bound

is 140 nm, and the upper bound results to 380 nm.

The capture radius measured with the BEC is calculated from the fit result shown as black circles in Fig. 4.9. It has been found that the atom loss can be approximated by taking the TF distribution of the BEC, the speed of sound ($\bar{v}_s = 0.8\,\mathrm{mm/s}$), and a CP-enhanced radius R_{cap} of the nanofiber into account. However, it should be noted that this model is of preliminary character (see discussion in Sec. 4.4.2). The enhancement of the scattering radius is assumed to be dependent on the geometric radius R_0 of the nanofiber. Using the obtained fit parameters for $R_{\mathrm{cap}}(R_0)$, the capture radius in dependence of R_0 can be calculated in the framework of the approximations. For every position along the long axis of the nanofiber, the geometric nanofiber radius is known from the SEM images and summarized in Fig. 3.3. The typical extent of the BEC is given by the Thomas-Fermi radius, which is 3.2 μm for the experimental conditions. The mean capture radius $\bar{R}_{\mathrm{cap}}$ for a BEC overlapping with the nanofiber is calculated by averaging $R_{\mathrm{cap}}(R_0)$, starting from the tip of the nanofiber towards the bottom over an interval of two times the TF radius. This result is the effective scattering radius of the nanofiber for a BEC just in complete overlap with the nanofiber. The averaging results to an effective radius of 393 nm. The latter is the radius at a typical velocity, i.e. the speed of sound. This result is shown in Fig. 4.10 as a large black $\times$ symbol.

In two independent measurements, a clearly "super-geometric" loss of ultracold atoms on a single, absorptive nanofiber has been observed. This behavior can be explained by the nanofiber's CP potential. Considering a CP potential of the form $-C_5/r^5$, the dispersive interaction of the nanofiber with thermal atoms has been quantified. The resulting value $C_5 = 6 \times 10^{-65}\,\mathrm{Jm}^5$ is the first nanofiber CP coefficient obtained with ultracold atoms. The lower error bound on this C_5 is around one order of magnitude smaller than the best-fit value, the upper bound approximately one order of magnitude larger (see Sec. 4.4). The reason for the large error of C_5 is the very weak scaling of this coefficient with the loss rate. Consequently, observing the decay behavior of ultracold thermal atoms on an immersed nanofiber might be not the optimal approach to do high precision measurements of the CP coefficient.

In addition to the measurement of the nanofiber's CP potential with an ultracold atomic cloud, analogue measurements have been performed with a BEC. Using a preliminary model, an effective scattering radius of the nanofiber has been obtained. This radius is in very good agreement with velocity-dependent scattering radius derived from the thermal results. The BEC value clearly lies within the errors of the thermal cloud data. The consistency of the two independent measurements emphasizes the high control of nanofiber-cloud interaction achieved in the present experiment and supports the theoretical approaches used to describe the experimental findings.

Chapter 5

Summary and Outlook

Summary

Within the framework of this thesis, techniques have been developed to combine ultracold atom physics and nanoscience. For the first time, an ultracold thermal gas as well as a Bose-Einstein condensate have been brought into controlled overlap with an individual, free-standing carbon nanofiber. The sub-micron positioning accuracy and the second-scale interaction time in the experiment have facilitated the quantification of the Casimir-Polder potential of the nanofiber by observing the decay of the interacting ultracold cloud. The individually obtained thermal and BEC results are consistent with each other.

To interpret the results of the measurements, a theory has been developed for the loss of ultracold thermal atoms captured by an immersed nanofiber. The obtained relations generally connect the decay rates of a thermal cloud with geometric and dispersive (Casimir-Polder) properties of a rotationally symmetric nanoobject. For the quantum degenerate gas, theoretical approaches to model the cloud decay due to the interaction with a nanofiber have been discussed and methodical challenges have been identified.

The technology and methods presented in this thesis pave the way for further experiments involving ultracold (quantum degenerate) atomic ensembles and nanostructures. Central questions concerning the absolute positioning of atom clouds as well as the deceleration of the in-trap center-of-mass motion have been addressed. For the design of future experiments, the Casimir-Polder force in general and in particular its scaling in the vicinity of nanostructured objects plays a crucial role. The present thesis has theoretically investigated the effect of a dispersive, rotationally-symmetric nanoobject on an ultracold cloud. Furthermore, and as a central achievement of the present thesis, the Casimir-Polder potential of a single, free-standing carbon nanofiber has been measured using ultracold atoms. For further research in the interdisciplinary field of nano-atomoptics, the dispersive properties of nanoobjects will be a central figure for both, theoretical and experimental research.

Outlook

A clear trend within ultracold atom research is to gain even more control over atomic ensembles and, ultimately, over individual atoms. Nanotechnology can make great contributions in this context by creating smaller and steeper traps using current-carrying nanowires [Pea05, Pet09, Sal10]. Alternatively, or as an extension to electromagnetic atom storage, traps formed by permanently magnetic (nano)domains have been suggested [All06, Fer08]. Further proposals on nano-scaled traps and, thus, few-atom experiments, e.g. include electro-optical traps [Mur09], optical nanofibers [Vet10], and illuminated metallic nanotips [Cha09]. Atom traps as tiny as a few nanometers would, for example, facilitate the investigation of effects in close proximity to a surface including the cross-over region between van-der-Waals force and Casimir-Polder force. Moreover, the quantum friction on moving atoms within a CP potential can possibly be measured [Sch09]. Testing the existence of a non-Newtonian gravitational force at small length scales [Dim03] would allow to investigate questions from cosmology in the lab. In addition, the investigation of the actual existence of temperature on the nanoscale [Har04] might become experimentally accessible. Finally, nanoelements allow to create completely new potential topographies for atom clouds. Extremely steep potential wells, decaying on the scale of the healing length of a BEC or below, could, for example, be a physical implementation of the box potential model system.

In addition to few-atom trapping and cooling, nano-fabricated atom-optical elements can improve atom detection. On the single-atom level, the latter is a non-trivial process which is, for example, implemented via photo-ionization and subsequent detection of the ion with a channeltron [GÖ9, Sti10]. Another approach involves cavities, which change their transmission as an atom is propagating through the resonator [MÖ9b, Geh10]. The drawback of these optical detection schemes is their poor scalability as well as their limitation to the wavelength of the light in terms of spatial resolution. Using charged carbon nanotubes and their enormous electrical field enhancement capabilities, atoms can be ionized by static electric fields and detected with standard methods [Grü09, Goo10]. Such a detector is perfectly scalable using individually contacted nanofibers and has a spatial resolution down to a few nanometers. Thus, for example, the investigation of correlation functions of ultracold thermal gases and BECs becomes experimentally accessible. Moreover, the use of individual charged nanotube might allow the observation of quantized conductance of neutral atoms [Ris05]. The application of carbon nanotube-based atom detection as (commercial) gas sensors [Mod03], however, might be controversial as the pathogenicity of nanostructures is not yet clarified [Pol08].

If the number of atoms comprising the nanoobject is on the order of the number of trapped atoms (which is the case for single-wall carbon nanotubes), a back-action of the atoms onto the object becomes important [Hun10]. Assuming sufficient coupling, e.g. by the magnetic fields generated from a current-carrying nanowire, this might allow cooling the nanowire by the atomic ensemble. Ultimately, respective schemes aim to approach the nanowire's vibrational ground state and, possibly,

the entanglement of the two systems [Ham09]. Ground state cooling was recently achieved with a cryogenicly cooled aluminum-nitrate resonator [O'C10]. The latter scientific milestone illustrates the tremendous technological control in the research of cooled micro- and nanoobjects. Thus, hybrid quantum systems composed of quantum solid state objects and ultracold atomic ensembles appear to be increasingly experimentally accessible.

Appendix A

A.1 Electric Dipole Forces from Adhered Rubidium

A.1.1 Principle

When working with ultracold atoms close to solid objects, atoms will get lost from the trap in the proximity of the macroscopic body's surface. It is likely that at least a fraction of these atoms will stick to the surface. Depending on the electronegativities of the bond constituents, the bond can have ionic character or be dominated by van-der-Waals forces.

In the ionic case, the electronic structure of the adhered atom is strongly modified by the solid state object. The situation is sketched in Fig. A.1 (a). The lowest lying P and S levels of ground state alkali atoms of the valence electron will interact with the energy bands of the macroscopic material[1]. If the renormalized atomic levels fall below the Fermi energy, the valence electron of the adhered atom will reside partially within the macroscopic body. This net charge transfer can be regarded as the formation of a charge and its image charge in the material, separated by a few Ångström. This dipole creates an electric field which can affect an ultracold cloud in a nearby magnetic trap. The potential originating from the electric field of adhered atoms on a surface is called patch potential [McG04].

The electric fields of adhered ^{87}Rb atoms on the carbon nanofiber should be discussed in more detail. As the scattering measurements on the nanofiber rely on the subtraction of a reference scattering signal from a plane substrate (i.e. without nanofiber), possible effects from ^{87}Rb adhered to the substrate are canceled out. The deposition of ^{87}Rb on the nanofiber surface can, in principle, arise from two processes: first, the adhesion of background gas atoms and second, the deposition of atoms released from the (overlapping) magnetic trap. Considering the number of

[1] In the context of patch potentials, the term *macroscopic* is used to describe solid state objects which are large compared to a single atom. This applies in particular to the nanofiber. The latter is still sufficiently large to define solid state object properties as e.g. a work function.

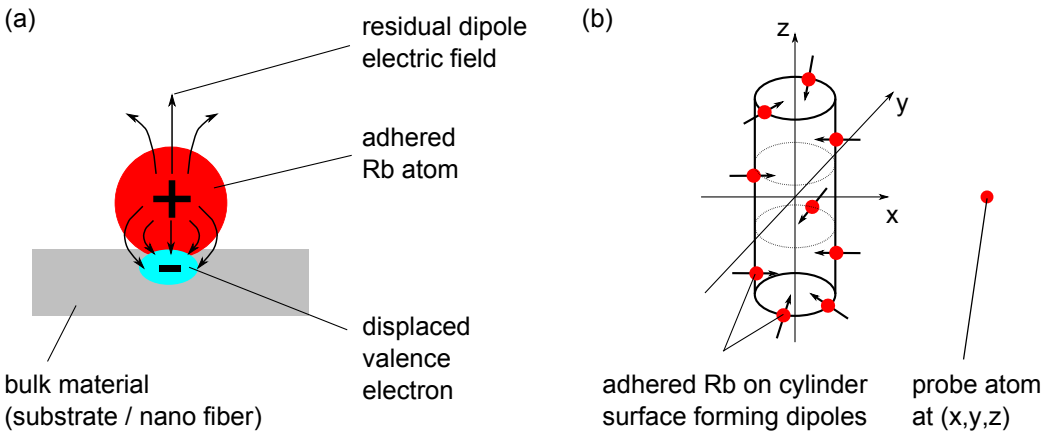

Figure A.1: Adhered atoms can form a bond of ionic character due to partial charge transfer to the surface (a). The two separated charges create a dipole, orientated perpendicular to the surface. In (b), a nanocylinder homogeneously covered with electric dipoles creates an electric field which is probed by an atom at $\vec{r} = (x, y, z)$.

rubidium atoms released from the dispenser at each experimental cycle[2] as well as the solid angle under which the nanofiber is hit, per run, less than hundred atoms hit the surface of the fiber. Only an unknown fraction of these atoms will adhere to the nanofiber surface. An effectively increased scattering nanofiber cross-section due to CP forces as discussed in chapter 4 can be neglected for the hot atoms from the dispenser. Following Ref. [McG04], the amount of adatoms coming directly from the dispenser to the nanofiber is assumed to be negligible. In turn, the main source for ^{87}Rb deposition on the nanofiber is atom release from the magnetic trap in proximity of the nanofiber.

A.1.2 Experimental Investigation of Adhered Dipoles

To experimentally investigate the effect of electric fields from adhered dipoles, first, the nanochip including the nanofiber undergoes a cleaning procedure. According to Ref. [Obr07b], the electric fields from patch potentials decay over time because of diffusion of adatoms over the surface. The electric field decay time τ at a substrate temperature T is given by

$$\tau(T) = \gamma_0^{-1} \exp\left(\frac{E_A}{k_b T}\right) \tag{A.1}$$

with the attempt rate γ_0 and the activation energy E_A (dependent on material properties). The effect depends exponentially on the substrate temperature. Consequently, to clean the surface, it is recommendable to heat the sample.

[2]The number of released atoms from the dispenser is calculated from the following quantities: the number of trapped atoms in the MOT (300×10^6), the MOT trap depth (2 K), and the shape of the Maxwell-Boltzmann distribution for atoms released from a 500 °C dispenser.

For cleaning, the setup is operated over three days without dispenser but with MOT- and transfer coils as well as the Ioffe wire driven as described in Sec. 2.3.1. In contrast to the normal experimental cycle, for the preparation of this measurement, the Peltier cooling of the vacuum interior is switched off (see Sec. 2.2.2). Consequently, the chamber interior is heating up because of ohmic power dissipation. The peak temperature of the transfer coils, which also hold the carrier chip, is approximately 70 °C as measured by the resistance change of the coil wires. While the gold wires on the carrier chip are in operation, they also dissipate heat. Their resistance change indicates a temperature increase of additional 65 °C, which, however, is not kept over the full experimental cycle. In total, the nanochip is expected to have an average temperature of around 70 °C with temperature peaks up to over 100 °C. For these temperatures, Ref. [Obr07b] indicates typical decay times of the adatom electric fields on the order of a few hours, assuming similar values for E_A and γ_0 like in the reference. Consequently, the applied nanochip cleaning procedure should reduce the patch potentials by several orders of magnitude.

To investigate the effect of atom adhesion on the nanofiber, an atom cloud is brought into partial overlap with the cleaned nanofiber and held for 200 ms. Overlap and interaction time are chosen such that there is a significant loss of atoms induced by the nanofiber. In turn, atoms from the trap have the chance to adhere to the fiber, as they pass the fiber several times during their oscillation within the magnetic trap. Moreover, the loss of atoms from the trap is mainly dominated by the fiber and not by the substrate (in comparable trap-substrate distances, only a low atom loss is measured when held over the plain substrate). After the cleaning procedure, the atom loss in the trap is monitored, starting with the very first ultracold cloud interacting with the cleaned nanofiber. There are no measurements needed for preparation because suitable parameters for this measurement are known from previous experiments. The cloud temperature is set to 80 nK, the atom number before interaction with the surface is approximately 2×10^5 . An identical physical situation in terms of cloud-nanofiber overlap and interaction time is then resembled for many experimental cycles. Thus, a possible change in the measured signal (number of atoms in the trap after 200 ms of interaction time) can only be due to patch potentials of gradually adhered ^{87}Rb atoms.

The results of this measurement are shown in Fig. A.2 (a). Importantly, starting from the very first measured point (first cloud interacting with the nanofiber after cleaning), the atom number stays constant within the shot-to-shot fluctuation level of the experimental apparatus. Consequently, there is no measurable effect on the number of remaining atoms in the trap arising from possible patch potentials of a few deposited clouds (a few 10^5 to 10^6 atoms).

In addition, more than 50 measurements of the type outlined in Sec. 3.2 (number of trapped atoms in dependence of interaction time for given overlap with the nanofiber) have been evaluated. The three points[3] measured at zero seconds interaction time are analyzed in terms of a possible correlation between the first point

[3]The three relevant data points include the actual data point (1) being part of the scattering measurement data set as well as two points (2,3) measured after all other recorded interaction times for reference purposes.

compared to the average of the data points two and three. Intermediate to the measurement of the points 1 and (2,3), a total of 30 to 40 clouds is driven towards the nanofiber. In the case of a measurable adatom effect, the mean value of the differential number of remaining atoms in the trap $N_{\text{diff}} = N_1 - \text{mean}(N_2, N_3)$ evaluated for many scattering measurements would deviate from zero[4]. For example, for an additional loss of atoms from the trap due to patch potentials, it would follow that $N_{\text{diff}} > 0$. However, an analysis of the measurements from Sec. 3.2 shows $N_{\text{diff}} = 0$ within the shot-to-shot fluctuations of the setup. In conclusion, there is no measurable effect on the trapped atom number due to a possible nanofiber patch potential of several ten deposited clouds.

The acquisition of a complete scattering measurement dataset takes one or two complete days, depending on the number of points per trap-surface distance d and the number of measured distances d. Typically, on the first day, approximately 10 distances d in a comparatively coarse sampling (e.g. $1 - 2\,\mu$m) are measured to estimate interesting parameter regions. On the second day, the distances d are sampled with higher resolution e.g. $0.5\,\mu$m. If, for example, d is chosen on the first day to be 5, 6, 7, $8\,\mu$m, typical values for the second day of measurements would be 5.5, 6.5, 7.5, $8.5\,\mu$m (here, for four distances d per day). While measuring ten values of d, several hundred atom clouds are released at the nanofiber. As the measured signals (atom number decay rates) show no correlation with the day of measurement, consequently also several hundred atom clouds deposited at the nanofiber do not have a measurable effect on the atom number in the magnetic trap.

The absence of a measurable effect of a few up to a few hundred deposited clouds on the atom number in the trap leaves three possible conclusions concerning the role of adatoms in the present experiment: either there are no adatoms at the nanofiber or atoms adhered to the nanofiber have no effect on the scattering measurement or there is a constant effect. The latter would necessarily require, first, a very long (more than a week) adatom electric field decay time even at an increased temperature of the chamber interior. This can not be excluded as the decay time exponentially depends on the activation energy E_A in Eq. A.1. The latter is not known for the nanofiber in the experiment[5]. Second, the effect necessarily needs to be saturated, such that additional atomic ensembles deposited onto the nanofiber do not further increase the effect.

A.1.3 Electric Field of Atoms Adhered to a Cylinder Surface

To quantitatively estimate the possible effect of patch potentials on the ultracold cloud, a model calculation for the system sketched in Fig. A.1 (b) is performed.

[4] In principle, also a drift of the setup can cause such a behavior. However, long-term measurements, e.g. in the Ioffe trap, show no drift behavior over a day.

[5] In fact, the diffusion of charges from a nanotube to a substrate is more involved than the situation sketched in Ref. [Obr07b]. For increased substrate temperatures, the activation energy E_a for the diffusion process can change. In Ref. [He09], E_a increases by more than a factor of two above a critical temperature of 150 °C.

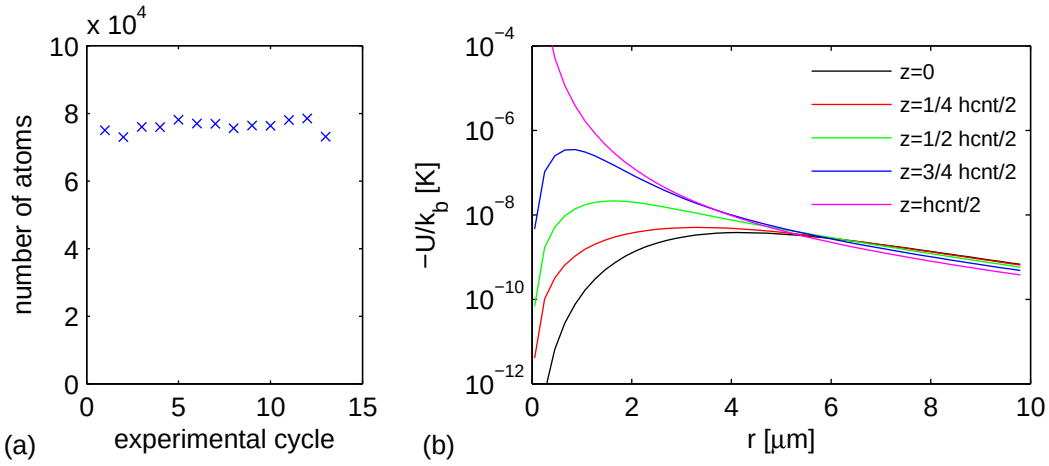

Figure A.2: After several days of thermal surface cleaning, the effect of possibly adhered ^{87}Rb atoms on the number of remaining atoms in the magnetic trap is measured (a). The first data point (cycle 1) corresponds to the first cloud interacting with the nanofiber after the cleaning process. Within the shot-to-shot fluctuations of the setup, there is no measurable effect on trapped atoms from the first 15 deposited clouds. In (b), the resulting electrostatic potential of the model calculation sketched in Fig. A.1 (b) is shown for different z positions of the probe atom (see legend and compare to Fig. A.1 (b)). The radial distance r is measured from the center of the cylinder. To account for the orders of magnitude scaling of the attractive potential (i.e. $U < 0$), $-U$ is plotted logarithmically.

Electric dipoles are homogeneously distributed on the surface of a long, thin cylinder (radius 75 nm, height $h_{\mathrm{NF}} = 10.25\,\mu$m). Each dipole with dipole moment $\vec{p}$ is aligned perpendicular to the surface, pointing into the cylinder. The electric field at the position $\vec{r} = (x, y, z)$ of a probe atom is given by the superposition of all individual electric fields at $\vec{r}$ from the dipoles on the surface. The electric field at $\vec{r}$ from a single dipole located at $\vec{r}_s$ is given by

$$\vec{E}(\vec{r}) = \frac{1}{4\pi\varepsilon_0}\left(\frac{3(\vec{p}\cdot\vec{\varrho})\vec{\varrho} - \vec{p}}{\varrho^3}\right) \qquad \vec{\varrho} = \vec{r} - \vec{r}_s. \tag{A.2}$$

The resulting superposed electric field obtained from integrating $\vec{r}_s$ in Eq. A.2 over the cylinder surface is the relevant field for the patch potential. In cylinder coordinates, the integral can be analytically solved first either for the azimuth angle θ or the height z. The successive integral over the remaining variable seems to have no analytical result. Therefore, this integration is done numerically. The obtained electric field $\vec{E}$ at $\vec{r}$ creates the potential [McG04]

$$U(\vec{r}) = -\frac{\alpha}{2}|\vec{E}(\vec{r})|^2 \tag{A.3}$$

for a probe atom of polarizability α at $\vec{r}$. In the case of ^{87}Rb, the static polarizability

is $5.25 \times 10^{-39}\,\mathrm{Fm}^2$ [Lid07].

The calculation of electric fields from the cylinder involves two crucial quantities, first, the number of adhered ^{87}Rb atoms on the surface and, second, the dipole moment per adatom $\vec{p}$. For the estimation of atoms on the surface, a single graphene layer covering the nanofiber is considered. SEM images of the nanofiber (see discussion in Sec. 3.1) suggest that a truncated cone is a reasonable approximation of the nanofiber's geometry. For the nanofiber used in the present experiment, the surface is estimated to be $5 \times 10^{-12}\,\mathrm{m}^2$. The carbon-carbon bond length a_{c-c} in the hexagonal graphene lattices is 142 pm [Dre01]. This allows to calculate the area per hexagon to

$$A_{\mathrm{hexa}} = \frac{3}{2} a_{c-c}^2 \sqrt{3} = 5.24 \times 10^{-20} m^2. \tag{A.4}$$

Thus, the nanofiber is covered by $\approx 9.6 \times 10^7$ lattices. As neighboring hexagons share each carbon atom to a third, there are only $1/3 \cdot 6 = 2$ atoms per hexagon. The graphene layer on the nanofiber, hence, contains $\approx 1.92 \times 10^8$ carbon atoms. According to Ref. [Ben08], there is a maximum intercalation ratio of 1/8 for alkali atoms doping graphite. This upper bound for the doping of the nanofiber might be generally a possible explanation for a saturation behavior. The ratio of 1/8 is used to calculate the maximum number of ^{87}Rb atoms on the nanofiber surface which amounts to $\approx 2.4 \times 10^7$.

In addition to the surface coverage, the dipole moment $|\vec{p}|$ per adatom has to be estimated. The magnitude of the arising electric field per adatom is connected to the charge transfer from the atom. This process depends on the ionization energy of the ^{87}Rb atoms (4.18 eV [Ste09]) and the work function of the macroscopic object. For the nanofiber, the latter can vary over a large range depending on the exact atomic structure. Calculations and summarized measurements in Ref. [Zha02] suggest a value for the nanofiber work function of ≈ 5 eV. In addition, the work function of a nanofiber is decreasing with increasing intercalation density of alkali atoms in the tube [Zha02]. This complicates the estimation of the nanofiber work function further. However, a value of 5 eV is in the range of the ionization energy of ^{87}Rb. Thus, a bond with ionic character is to be expected. Intuitively, the dipole moment of one adhered ^{87}Rb atom on a solid body should be larger for a larger ratio of work function W_a over ionization energy E_i. In contrast to this intuitive picture, as shown in Ref. [Obr07b], for the same adatom species (i.e. the same ionization energy E_i), the adatom dipole moment is *not* always larger for a larger work function. In general, the dipole moment per adhered ^{87}Rb atom seems to be larger on metallic than on insulating substrates. As no reliable information of the dipole moment $\vec{p}$ of a single ^{87}Rb atom adhered on a nanofiber is available, for the model calculation, a dipole moment of 3 Debye is chosen. This is the value obtained in Ref. [McG04] for ^{87}Rb on Silicon and on Titanium. However, the choice of this value for the nanofiber is somewhat speculative. For example, ^{87}Rb on gold shows a dipole moment of 10 Debye [Tau10] per adatom. Even higher values are found in Ref. [Obr07b] for yttrium, i.e. $|\vec{p}| = 35$ Debye.

For a homogeneous surface coverage of $\approx 2.4 \times 10^7$ and a dipole moment of 3 Debye per adatom, the resulting potential $U(r, z)$ is shown in Fig. A.2 (b). This is the outcome of the application of Eq. A.3 to the superposed electric field of all adatoms. The calculated patch potentials are attractive (i.e. $U < 0$) and vary over several orders of magnitude. Therefore, the plot displays $-U$ with semi-logarithmic scaling. The calculation is repeated for different z positions of the probe atom (probe atom shifts along the long nanofiber axis, see Fig. A.2 (b)). The black curve in the plot shows $U(r)$ for $z = 0$, i.e. on a line symmetric to the two ends of the cylinder. The potential $U(r, z = 0)$ shows a local minimum at 4.2 μm which has a depth of 3.7 nK. For asymmetric values of z (in the plot, $1/4 \cdot h_{\mathrm{NF}}/2$, $1/2 \cdot h_{\mathrm{NF}}/2$, and $3/4 \cdot h_{\mathrm{NF}}/2$ shown in red, green, and blue, respectively), the local minimum gets deeper and moves towards the center of the nanofiber. At $z = h_{\mathrm{NF}}/2$ (magenta curve), the minimum vanishes, and the electric field (and so, the potential) seems to diverge. However, a truly infinite potential is unphysical and, at the latest, prevented e.g. by the repulsive atom-atom (e.g. Lennard-Jones) potential.

As visible from Fig. A.2 (b), the influence of patch potentials can be very large, e.g. the maximum potential depth for $z = 3/4 \cdot h_{\mathrm{NF}}/2$ is already ≈ 400 nK. The magnitude of the patch potentials scale quadratically with the product of the dipole moment per atom and the areal dipole density on the nanofiber surface, $|\vec{p}| \cdot n_{\mathrm{dipole}}$. As both quantities are only known with a large uncertainty, the magnitude of the patch potentials can strongly differ from the results in Fig. A.2 (b). For example for a dipole moment of 35 Debye as measured for ^{87}Rb on yttrium, the potentials would be approximately 100 times as deep as in the present calculation. In addition, the distribution function of adatoms on the nanofiber surface has an influence on the electric field around the fiber. Depending on the exact atom deposition process, alternative distribution functions compared to the homogeneous case discussed here are conceivable but, at this point, not further considered.

Concluding the observations from the measurements and the simulation results of the patch potentials, it is very likely that adhered ^{87}Rb atoms on the nanofiber do not play a role for the present scattering experiment. The strong potentials obtained from the calculations summarized in Fig. A.2 (b) for $|\vec{p}| = 3$ Debye would certainly lead to a loss of atoms in the magnetic trap strongly visible in different measurement. In particular, in the case of μK-deep patch potentials, the measurements of the surface topography outlined in Ref. [Gie10] would show significant deviation from the behavior expected from SEM images. The effect would be even more dominant for larger $\vec{p}$. As the surface topography measurements with the atoms match very well the SEM results, not a constant but no measurable patch potential is expected for the present experiment.

A.2 Shutters

A shutter has been developed for the experiment, excelling in simple construction, high reliability, and fast repair in the case of failure. The technical drawings in 1 : 2 scaling are shown in Figs. A.3 and A.4, including the correct measures needed for manufacturing. In the focus of a lens, switching times of the shutter are less than $10\,\mu$s, the standard deviation of the delay is around $15\,\mu$s. However, after several thousand cycles, the delay jitter increases as the shutter micro-mechanics gets more and more loose. The cheap switching part can be exchanged in one minute, making the shutter fully operational, again. The recommended current pulses for opening and closing the shutter are 8 ms, respectively.

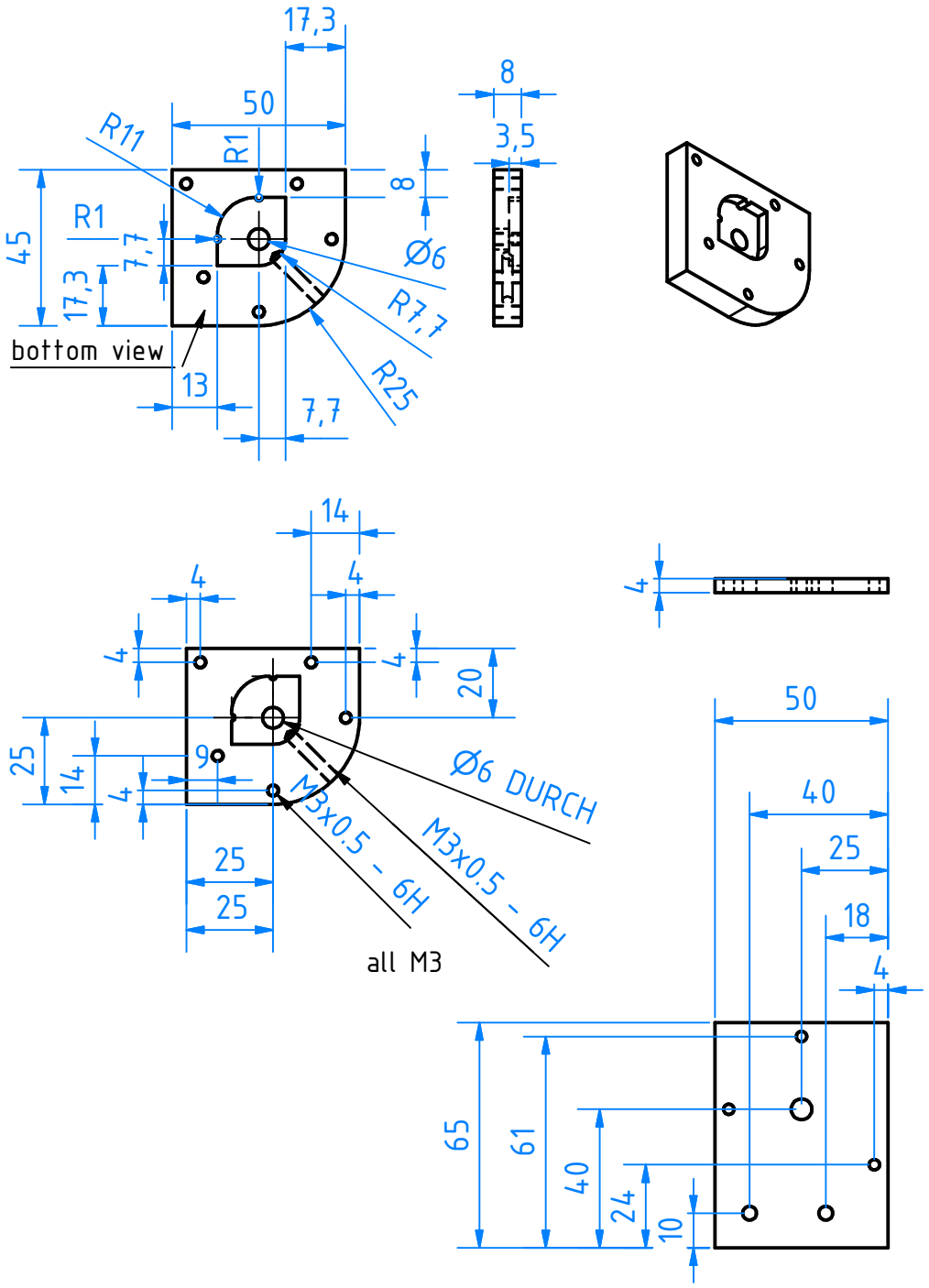

Figure A.3: Technical drawing of the central shutter holder and the back plane (1 : 2 scale).

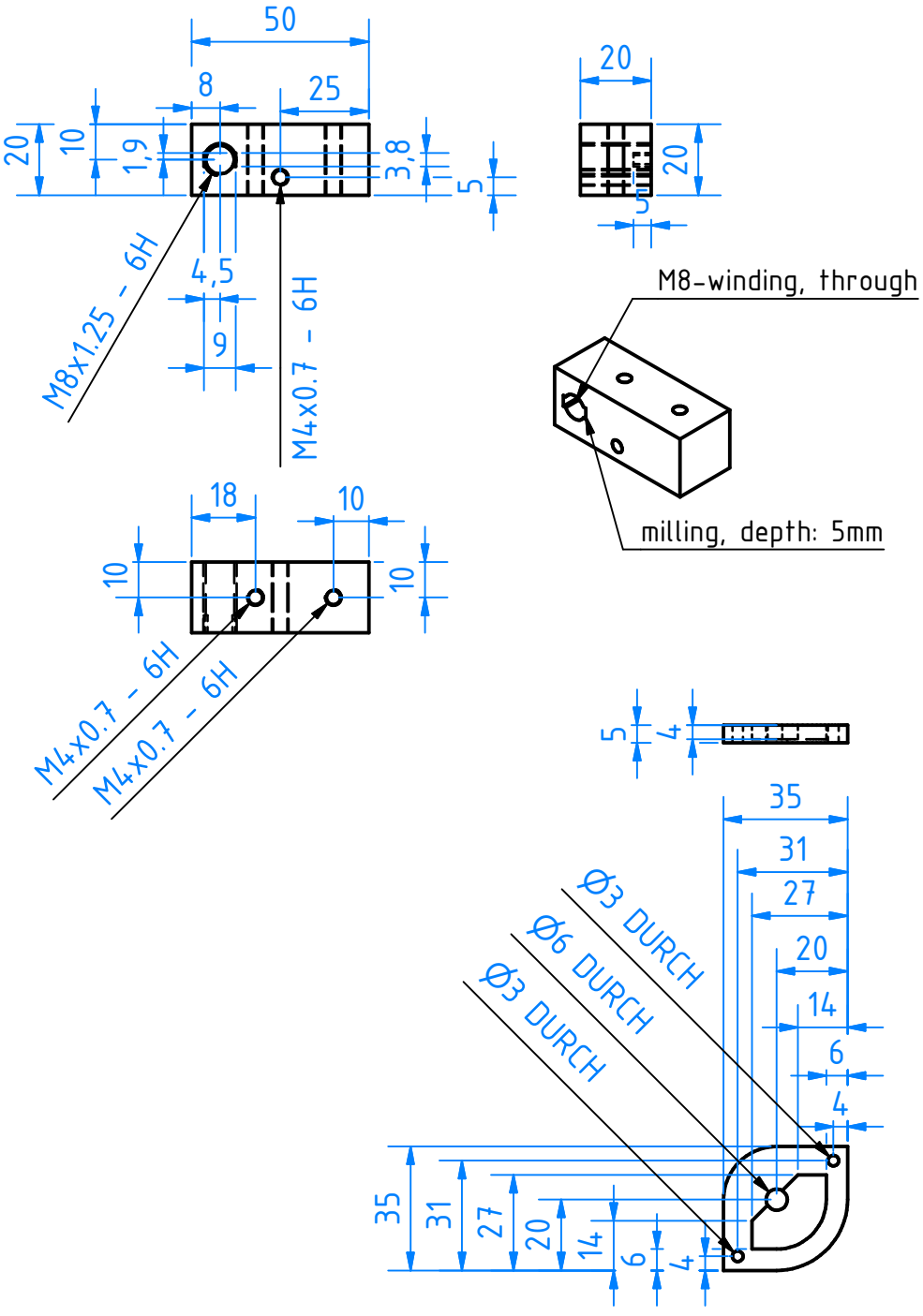

Figure A.4: Technical drawing of the foot and the cap, the latter fixing the shutter unit ($1:2$ scale).

Bibliography

[All06] D. A. Allwood, T. Schrefl, G. Hrkac, I. G. Hughes and C. S. Adams, *Mobile atom traps using magnetic nanowires*, Appl. Phys. Lett. **89**, 014102 (2006).

[Ana95] A. Anandarajah and J. Chen, *Single Correction Function for Computing Retarded van der Waals Attraction*, J. Colloid Interface Sci. **176**, 293 (1995).

[And88] A. Anderson, S. Haroche, E. A. Hinds, W. Jhe and D. Meschede, *Measuring the van der Waals forces between a Rydberg atom and a metallic surface*, Phys. Rev. A **37**, 3594 (1988).

[And95] M. H. Anderson, J. R. Ensher, M. R. Matthews, C. E. Wieman and E. A. Cornell, *Observation of Bose-Einstein Condensation in a Dilute Atomic Vapor*, Science **269**, 198 (1995).

[Ant04] M. Antezza, L. P. Pitaevskii and S. Stringari, *Effect of the Casimir-Polder force on the collective oscillations of a trapped Bose-Einstein condensate*, Phys. Rev. A **70**, 053619 (2004).

[Arn07] F. Arnecke, H. Friedrich and J. Madronero, *Quantum effects in collisions of ultracold atoms with walls and nanostructures*, J. Phys. Conf. Ser. **88**, 012041 (2007).

[Bar75] Yu. S. Barash and V. F. Ginzburg, *Electromagnetic Fluctuations in Matter and Molecular (van der Waals) Forces Between Them*, Sov. Phys. Usp. **18**, 305 (1975).

[Bar89] Yu. S. Barash and A. A. Kyasov, Sov. Phys. JETP **68**, 39 (1989).

[Bar07] C. Barceló, A. Cano, L. J. Garay and G. Jannes, *Quasinormal mode analysis in BEC acoustic black holes*, Phys. Rev. D **75**, 084024 (2007).

[Ben95] L. X. Benedict, S. G. Louie and M. L. Cohen, *Static polarizabilities of single-wall carbon nanotubes*, Phys. Rev. B **52**, 8541 (1995).

[Ben08] N. Bendiab, A. M. Saitta, R. Aznar, J. L. Sauvajol, R. Almairac, I. Mirebeau and G. Andre, *Rubidium localization in single-walled carbon nanotube bundles: Structural study*, Phys. Rev. B **78**, 104108 (2008).

[Ben10] H. Bender, Ph. W. Courteille, C. Marzok, C. Zimmermann and S. Slama, *Direct Measurement of Intermediate-Range Casimir-Polder Potentials*, Phys. Rev. Lett. **104**, 083201 (2010).

[Bhu04] edited by B. Bhushan, *Handbook of Nanotechnology*, (Springer, 2004).

[Bla05] E. V. Blagov, G. L. Klimchitskaya and V. M. Mostepanenko, *Van der Waals interaction between microparticle and uniaxial crystal with application to hydrogen atoms and multiwall carbon nanotubes*, Phys. Rev. B **71**, 235401 (2005).

[Blo99] I. Bloch, T. W. Hänsch and T. Esslinger, *Atom Laser with a cw Output Coupler*, Phys. Rev. Lett. **82**, 3008 (1999).

[Boe10] M. P. de Boer, A. D. Corwin, F. W. DelRio and W. R. Ashurst, in *Friction and Wear in Micro- and Nanomachines*, edited by B. Bhushan, (Springer Press, 2010).

[Bou02] M. Boustimi, J. Baudon, P. Candori and J. Robert, *van der Waals interaction between an atom and a metallic nanowire*, Phys. Rev. B **65**, 155402 (2002).

[Bru08] M. Bruderer, W. Bao and D. Jaksch, *Self-trapping of impurities in Bose-Einstein condensates: Strong attractive and repulsive coupling*, Europhys. Lett. **82**, 30004 (2008).

[Buh08] S. Y. Buhmann and S. Scheel, *Thermal Casimir versus Casimir-Polder Forces: Equilibrium and Nonequilibrium Forces*, Phys. Rev. Lett. **100**, 253201 (2008).

[Buh10] S. Yo. Buhmann, S. Scheel and J. Babington, *Universal Scaling Laws for Dispersion Interactions*, Phys. Rev. Lett. **104**, 070404 (2010).

[Bur97] E. A. Burt, R. W. Ghrist, C. J. Myatt, M. J. Holland, E. A. Cornell and C. E. Wieman, *Coherence, Correlations, and Collisions: What One Learns about Bose-Einstein Condensates from Their Decay*, Phys. Rev. Lett. **79**, 337 (1997).

[Cas48a] H. B. G. Casimir, *On the attraction between two perfectly conducting plates*, Proc. of the Royal Netherlands Acad. of Arts and Sciences **51**, 793 (1948).

[Cas48b] H. B. G. Casimir and D. Polder, *The Influence of Retardation on the London-van der Waals Forces*, Phys. Rev. **73**, 360 (1948).

[Cha09] D. E. Chang, J. D. Thompson, H. Park, V. Vuletic, A. S. Zibrov, P. Zoller and M. D. Lukin, *Trapping and Manipulation of Isolated Atoms Using Nanoscale Plasmonic Structures*, Phys. Rev. Lett. **103**, 123004 (2009).

[Cou96] J.-Y. Courtois, J.-M. Courty and J. C. Mertz, *Internal dynamics of multilevel atoms near a vacuum-dielectric interface*, Phys. Rev. A **53**, 1862 (1996).

[Cra07] G. E. Cragg and A. K. Kerman, *Coherent Decay of Bose-Einstein Condensates*, Phys. Rev. Lett. **98**, 080405 (2007).

[Dal89] J. Dalibard and C. Cohen-Tannoudji, *Laser cooling below the Doppler limit by polarization gradients: Simple theoretical models*, J. Opt. Soc. Am. B **6**, 2023 (1989).

[Dal99] F. Dalfovo, S. Giorgini, L. P. Pitaevskii and S. Stringari, *Theory of Bose-Einstein condensation in trapped gases*, Rev. Mod. Phys. **71**, 463 (1999).

[Dal08] D. A. R. Dalvit, P. A. Maia Neto, A. Lambrecht and S. Reynaud, *Probing Quantum-Vacuum Geometrical Effects with Cold Atoms*, Phys. Rev. Lett. **100**, 040405 (2008).

[Dav95a] K. B. Davis, M. O. Mewes, M. R. Andrews, N. J. van Druten, D. S. Durfee, D. M. Kurn and W. Ketterle, *Bose-Einstein Condensation in a Gas of Sodium Atoms*, Phys. Rev. Lett. **75**, 3969 (1995).

[Dav95b] K. B. Davis, M.-O. Mewes and W. Ketterle, *An analytical model for evaporative cooling of atoms*, Appl. Phys. B **60**, 155 (1995).

[DeB36] J. H. DeBoer, Trans. Faraday Soc. **32**, 10 (1936).

[Dem03] W. Demtröder, *Laser Spectroscopy*, (Springer Press, 2003) 3rd edition.

[Den98] J. Denschlag, G. Umshaus and J. Schmiedmayer, *Probing a Singular Potential with Cold Atoms: A Neutral Atom and a Charged Wire*, Phys. Rev. Lett. **81**, 737 (1998).

[Den99] J. Denschlag, D. Cassettari, A. Chenet, S. Schneider and J. Schmiedmayer, *A neutral atom and a wire: towards mesoscopic atom optics*, Appl. Phys. B **69**, 291 (1999).

[Der57] B. V. Derjaguin and I. I. Abrikosova, *Direct Measurement of the Molecular Attraction of Solid Bodies*, Sov. Phys. JETP **3**, 819 (1957).

[DeR81] L. L. DeRaad and K. A. Milton, *Casimir self-stress on a perfectly conducting cylindrical shell*, Annals of Physics **136**, 229 (1981).

[Der99] A. Derevianko, W. R. Johnson, M. S. Safronova and J. F. Babb, *High-Precision Calculations of Dispersion Coefficients, Static Dipole Polarizabilities, and Atom-Wall Interaction Constants for Alkali-Metal Atoms*, Phys. Rev. Lett. **82**, 3589 (1999).

[Dim03] A. A. Dimopoulos, S.and Geraci, *Probing submicron forces by interferometry of Bose-Einstein condensed atoms*, Phys. Rev. D **68**, 124021 (2003).

[Dre01] edited by M.S. Dresselhaus, G. Dresselhaus and Ph. Avouris, *Carbon Nanotubes*, (Springer, 2001).

[Dzy61] I. E. Dzyaloshinskii, E. M. Lifshitz and L. P. Pitaevskii, *The general theory of van der Waals forces 1*, Adv. Phys. **10**, 165 (1961).

[Ebe07] C. Eberlein and R. Zietal, *Force on a neutral atom near conducting microstructures*, Phys. Rev. A **75**, 032516 (2007).

[Ebe09] C. Eberlein and R. Zietal, *Retarded Casimir-Polder force on an atom near reflecting microstructures*, Phys. Rev. A **80**, 012504 (2009).

[Ell10] S. Å. Ellingsen, I. Brevik and K. A. Milton, *Casimir effect at nonzero temperature for wedges and cylinders*, Phys. Rev. D **81**, 065031 (2010).

[Fag07] J. A. Fagan, J. R. Simpson, B. J. Landi, L. J. Richter, I. Mandelbaum, V. Bajpai, D. L. Ho, R. Raffaelle, A. R. Hight Walker, B. J. Bauer and

E. K. Hobbie, *Dielectric Response of Aligned Semiconducting Single-Wall Nanotubes*, Phys. Rev. Lett. **98**, 147402 (2007).

[Fer07] R. Fermani, S. Scheel and P. L. Knight, *Trapping cold atoms near carbon nanotubes: Thermal spin flips and Casimir-Polder potential*, Phys. Rev. A **75**, 062905 (2007).

[Fer08] T. Fernholz, R. Gerritsma, S. Whitlock, I. Barb and R. J. C. Spreeuw, *Fully permanent magnet atom chip for Bose-Einstein condensation*, Phys. Rev. A **77**, 033409 (2008).

[Fin10] M. Fink, A. Naranjo, F. Arnecke, J. Eiglsperger, H. Friedrich, J. Madroñero, P. Raab and A. Wirzba, *s-wave scattering of a polarizable atom by an absorbing nanowire*, Phys. Rev. A **81**, 062714 (2010).

[Fol02] R. Folman, P. Krüger, J. Schmiedmayer, J. Denschlag and C. Henkel, *Microscopic atom optics: From wires to an atom chip*, **48**, 263 (2002).

[For98] J. Fortágh, A. Grossmann, C. Zimmermann and T. W. Hänsch, *Miniaturized Wire Trap for Neutral Atoms*, Phys. Rev. Lett. **81**, 5310 (1998).

[For02] J. Fortágh, H. Ott, S. Kraft, A. Günther and C. Zimmermann, *Surface effects in magnetic microtraps*, Phys. Rev. A **66**, 041604 (2002).

[For03a] J. Fortágh, *Bose-Einstein-Kondensate in Magnetischen Mikrofallen*, PhD thesis Universität Tübingen 2003.

[For03b] J. Fortágh, H. Ott, S. Kraft, A. Günther and C. Zimmermann, *Bose-Einstein condensates in magnetic waveguides*, Appl. Phys. B **76**, 157 (2003).

[For07] J. Fortágh and C. Zimmermann, *Magnetic microtraps for ultracold atoms*, Rev. Mod. Phys. **79**, 235 (2007).

[Fri02] H. Friedrich, G. Jacoby and C. G. Meister, *Quantum reflection by Casimir–van der Waals potential tails*, Phys. Rev. A **65**, 032902 (2002).

[GÖ5] A. Günther, M. Kemmler, S. Kraft, C. J. Vale, C. Zimmermann and J. Fortágh, *Combined chips for atom optics*, Phys. Rev. A **71**, 063619 (2005).

[GÖ9] A. Günther, H. Bender, A. Stibor, J. Fortágh and C. Zimmermann, *Observing quantum gases in real time: Single-atom detection on a chip*, Phys. Rev. A **80**, 011604 (2009).

[Gar00] L. J. Garay, J. R. Anglin, J. I. Cirac and P. Zoller, *Sonic Analog of Gravitational Black Holes in Bose-Einstein Condensates*, Phys. Rev. Lett. **85**, 4643 (2000).

[Gar01] L. J. Garay, J. R. Anglin, J. I. Cirac and P. Zoller, *Sonic black holes in dilute Bose-Einstein condensates*, Phys. Rev. A **63**, 023611 (2001).

[Geh10] R. Gehr, J. Volz, G. Dubois, T. Steinmetz, Y. Colombe, B. L. Lev, R. Long, J. Estève and J. Reichel, *Cavity-Based Single Atom Preparation and High-Fidelity Hyperfine State Readout*, Phys. Rev. Lett. **104**, 203602 (2010).

[Gie10] M. Gierling, *Working Title: Measuring the Topography of a Nanostructured Surface with Ultracold Atoms*, PhD thesis Universität Tübingen 2010.

[Gün03] A. Günther, *Integrierter Atom-Chip für ultrakalte Atome*, Master's thesis Universität Tübingen 2003.

[Goo10] A. Goodsell, T. Ristroph, J. A. Golovchenko and L. V. Hau, *Field Ionization of Cold Atoms near the Wall of a Single Carbon Nanotube*, Phys. Rev. Lett. **104**, 133002 (2010).

[Gor06] M.-P. Gorza and M. Ducloy, *Van der Waals interactions between atoms and dispersive surfaces at finite temperature*, Eur. Phys. J. D **40**, 343 (2006).

[Gos98] P. Gosdzinsky and A. Romeo, *Energy of the vacuum with a perfectly conducting and infinite cylindrical surface*, Phys. Lett. B **441**, 265 (1998).

[Grü09] B. Grüner, M. Jag, A. Stibor, G. Visanescu, M. Häffner, D. Kern, A. Günther and J. Fortágh, *Integrated atom detector based on field ionization near carbon nanotubes*, Phys. Rev. A **80**, 063422 (2009).

[Gri00] R. Grimm, M. Weidemuller and Y. B. Ovchinnikov, *Optical dipole traps for neutral atoms*, Adv. At. Mol. Opt. Phys. **42**, 95 (2000).

[Gu99] Y. Gu and D. Li, *The van der Waals Interaction between a Spherical Particle and a Cylinder*, J. Colloid Interface Sci. **217**, 60 (1999).

[HÖ1] W. Hänsel, J. Reichel, P. Hommelhoff and T. W. Hänsch, *Magnetic Conveyor Belt for Transporting and Merging Trapped Atom Clouds*, Phys. Rev. Lett. **86**, 608 (2001).

[Hai05] S. A. Haine and J. J. Hope, *Outcoupling from a Bose-Einstein condensate with squeezed light to produce entangled-atom laser beams*, Phys. Rev. A **72**, 033601 (2005).

[Ham37] H. C. Hamaker, Physica **4**, 1058 (1937).

[Ham09] K. Hammerer, M. Aspelmeyer, E. S. Polzik and P. Zoller, *Establishing Einstein-Poldosky-Rosen Channels between Nanomechanics and Atomic Ensembles*, Phys. Rev. Lett. **102**, 020501 (2009).

[Har03] D. M. Harber, J. M. McGuirk, J. M. Obrecht and E. A. Cornell, *Thermally induced losses in ultra-cold atoms magnetically trapped near room-temperature surfaces*, J. Low Temp. Phys. **133**, 229 (2003).

[Har04] M. Hartmann, G. Mahler and O. Hess, *Existence of Temperature on the Nanoscale*, Phys. Rev. Lett. **93**, 080402 (2004).

[Har05] D. M. Harber, J. M. Obrecht, J. M. McGuirk and E. A. Cornell, *Measurement of the Casimir-Polder force through center-of-mass oscillations of a Bose-Einstein condensate*, Phys. Rev. A **72**, 033610 (2005).

[He09] Y. He, H. G. Ong, Y. Zhao, S. He, L.-J. Li and J. Wang, *Study of Charge Diffusion at the Carbon Nanotube-SiO2 Interface by Electrostatic Force*

Microscopy, J. Phys. Chem. C **113**, 15476 (2009).

[Hen99] C. Henkel, S. Potting and M. Wilkens, *Loss and heating of particles in small and noisy traps*, Appl. Phys. B **69**, 379 (1999).

[Hän75] T.W. Hänsch and A.L. Schawlow, *Cooling of gases by laser radiation*, Opt. Commun. **13**, 68 (1975).

[Hän01] W. Hänsel, P. Hommelhoff, T. W. Hänsch and J. Reichel, *Bose-Einstein condensation on a microelectronic chip*, Nature **413**, 498 (2001).

[Hol96] M. Holland, K. Burnett, C. Gardiner, J. I. Cirac and P. Zoller, *Theory of an atom laser*, Phys. Rev. A **54**, R1757 (1996).

[Hom05] P. Hommelhoff, W. Hänsel, T. Steinmetz, T. W. Hänsch and J. Reichel, *Transporting, splitting and merging of atomic ensembles in a chip trap*, New J. Phys. **7**, 3 (2005).

[Hun10] D. Hunger, S. Camerer, T. W. Hänsch, D. König, J. P. Kotthaus, J. Reichel and P. Treutlein, *Resonant Coupling of a Bose-Einstein Condensate to a Micromechanical Oscillator*, Phys. Rev. Lett. **104**, 143002 (2010).

[Jac62] J. D. Jackson, *Classical Electrodynamics*, (John Wiley and Sons, Inc., 1962).

[Jud10a] T. E. Judd, *Personal Communication*, (2010).

[Jud10b] T. E. Judd, *Working title: Van-der-Waals Potentials for Realistic Nanostructures*, (2010).

[Kap06] J.I. Kapusta and C. Gale, *Finite Temperature Field Theory*, (Cambridge University Press, 2006).

[Kas10] B. Kasch, H. Hattermann, D. Cano, T. E. Judd, S. Scheel, C. Zimmermann, R. Kleiner, D. Koelle and J. Fortágh, *Cold atoms near superconductors: atomic spin coherence beyond the Johnson noise limit*, New J. Phys. **12**, 065024 (2010).

[Ket96] W. Ketterle and N.J. Van Druten, *Evaporative Cooling of Trapped Atoms*, Adv. At. Mol. Opt. Phys. **37**, 181 (1996).

[Ket99] W. Ketterle, D. S. Durfee and D. M. Stamper-Kurn, *Making, Probing and Understanding Bose-Einstein Condensates*, Proceedings of the International School of Physics Enrico Fermi page 67 (1999).

[Kli09] G. L. Klimchitskaya, U. Mohideen and V. M. Mostepanenko, *The Casimir force between real materials: Experiment and theory*, Rev. Mod. Phys. **81**, 1827 (2009).

[Koz06] B. Kozinsky and N. Marzari, *Static Dielectric Properties of Carbon Nanotubes from First Principles*, Phys. Rev. Lett. **96**, 166801 (2006).

[Kri98] A. Krishnan, E. Dujardin, T. W. Ebbesen, P. N. Yianilos and M. M. J. Treacy, *Young's modulus of single-walled nanotubes*, Phys. Rev. B **58**, 14013 (1998).

[Kur07] Y. Kurita and T. Morinari, *Formation of a sonic horizon in isotropically*

expanding Bose-Einstein condensates, Phys. Rev. A **76**, 053603 (2007).

[Lan80] L. D. Landau and E. M. Lifshitz, *Statistical Physics*, (Pergamon Press, 1980) 3rd edition.

[Lan81] L. D. Landau and E. M. Lifshitz, *Mechanics*, (Butterworth-Heinemann, 1981) 3rd edition.

[Leo03] U. Leonhardt, T. Kiss and P. Öhberg, *Theory of elementary excitations in unstable Bose-Einstein condensates and the instability of sonic horizons*, Phys. Rev. A **67**, 033602 (2003).

[Let88] P. D. Lett, R. N. Watts, C. I. Westbrook, W. D. Phillips, P. L. Gould and H. J. Metcalf, *Observation of Atoms Laser Cooled below the Doppler Limit*, Phys. Rev. Lett. **61**, 169 (1988).

[Lid07] edited by David R. Lide, *CRC Handbook of Chemistry and Physics*, (Taylor and Francis, 2007) 87 edition.

[Lif56] E. M. Lifshitz, *The Theory of Molecular Attractive Forces Between Solids*, Sov. Phys. JETP **2**, 73 (1956).

[Lin04] Y. Lin, I. Teper, C. Chin and V. Vuletic, *Impact of the Casimir-Polder Potential and Johnson Noise on Bose-Einstein Condensate Stability Near Surfaces*, Phys. Rev. Lett. **92**, 050404 (2004).

[Lon30] F. London, *Zur Theorie und Systematik der Molekularkräfte*, Zeitschrift für Physik **63**, 245 (1930).

[Lui96] O. J. Luiten, M. W. Reynolds and J. T. M. Walraven, *Kinetic theory of the evaporative cooling of a trapped gas*, Phys. Rev. A **53**, 381 (1996).

[M99a] D. Müller, D. Z. Anderson, R. J. Grow, P. D. D. Schwindt and E. A. Cornell, *Guiding Neutral Atoms Around Curves with Lithographically Patterned Current-Carrying Wires*, Phys. Rev. Lett. **83**, 5194 (1999).

[M99b] P. Münstermann, T. Fischer, P. Maunz, P. W. H. Pinkse and G. Rempe, *Dynamics of Single-Atom Motion Observed in a High-Finesse Cavity*, Phys. Rev. Lett. **82**, 3791 (1999).

[Mar82] A. M. Marvin and F. Toigo, *van der Waals interaction between a point particle and a metallic surface. I. Theory*, Phys. Rev. A **25**, 782 (1982).

[Mar94] M. Marinescu, H. R. Sadeghpour and A. Dalgarno, *Dynamic dipole polarizabilities of rubidium*, Phys. Rev. A **49**, 5103 (1994).

[McG04] J. M. McGuirk, D. M. Harber, J. M. Obrecht and E. A. Cornell, *Alkali-metal adsorbate polarization on conducting and insulating surfaces probed with Bose-Einstein condensates*, Phys. Rev. A **69**, 062905 (2004).

[Mer00] V. I. Merkulov, D. H. Lowndes, Y. Y. Wei, G. Eres and E. Voelkl, *Patterned growth of individual and multiple vertically aligned carbon nanofibers*, Appl. Phys. Lett. **76**, 3555 (2000).

[Mil94] P.W. Milonni, *The Quantum Vacuum - An Introduction to Quantum Electrodynamics*, (Academic Press, 1994).

[Mod03] A. Modi, N. l. Koratkar, E. Lass, B. Wei and P. M. Ajayan, *Miniaturized gas ionization sensors using carbon nanotubes*, Nature **424**, 171 (2003).

[Mon00] S. W. Montgomery, M. A. Franchek and V. W. Goldschmidt, *Analytical Dispersion Force Calculations for Nontraditional Geometries*, J. Colloid Interface Sci. **227**, 567 (2000).

[Mug04] J.G. Muga, J.P. Palao, B. Navarro and I.L. Egusquiza, *Complex absorbing potentials*, Physics Reports **395**, 357 (2004).

[Mur09] B. Murphy and L. V. Hau, *Electro-Optical Nanotraps for Neutral Atoms*, Phys. Rev. Lett. **102**, 033003 (2009).

[New70] D. M. Newns, *Dielectric Response of a Semi-Infinite Degenerate Electron Gas*, Phys. Rev. B **1**, 3304 (1970).

[Obr07a] J. M. Obrecht, R. J. Wild, M. Antezza, L. P. Pitaevskii, S. Stringari and E. A. Cornell, *Measurement of the Temperature Dependence of the Casimir-Polder Force*, Phys. Rev. Lett. **98**, 063201 (2007).

[Obr07b] J. M. Obrecht, R. J. Wild and E. A. Cornell, *Measuring electric fields from surface contaminants with neutral atoms*, Phys. Rev. A **75**, 062903 (2007).

[O'C10] A. D. O'Connell, M. Hofheinz, M. Ansmann, Radoslaw C. Bialczak, M. Lenander, Erik Lucero, M. Neeley, D. Sank, H. Wang, M. Weides, J. Wenner, John M. Martinis and A. N. Cleland, *Quantum ground state and single-phonon control of a mechanical resonator*, Nature **464**, 697 (2010).

[Ott01] H. Ott, J. Fortágh, G. Schlotterbeck, A. Grossmann and C. Zimmermann, *Bose-Einstein Condensation in a Surface Microtrap*, Phys. Rev. Lett. **87**, 230401 (2001).

[Ott03a] H. Ott, *Dynamik von Bose-Einstein-Kondensaten in anharmonischen Wellenleitern*, PhD thesis Universität Tübingen 2003.

[Ott03b] H. Ott, J. Fortágh, S. Kraft, A. Günther, D. Komma and C. Zimmermann, *Nonlinear Dynamics of a Bose-Einstein Condensate in a Magnetic Waveguide*, Phys. Rev. Lett. **91**, 040402 (2003).

[Par06] V. A. Parsegian, *A Handbook for Biologists, Chemists, Engineers, and Physicists*, (Cambridge Univ. Press, 2006).

[Pas04] T. A. Pasquini, Y. Shin, C. Sanner, M. Saba, A. Schirotzek, D. E. Pritchard and W. Ketterle, *Quantum Reflection from a Solid Surface at Normal Incidence*, Phys. Rev. Lett. **93**, 223201 (2004).

[Pea05] V. Peano, M. Thorwart, A. Kasper and R. Egger, *Nanoscale atomic waveguides with suspended carbon nanotubes*, Appl. Phys. B **81**, 1075 (2005).

[Pet09] P. G. Petrov, S. Machluf, S. Younis, R. Macaluso, T. David, B. Hadad, Y. Japha, M. Keil, E. Joselevich and R. Folman, *Trapping cold atoms using surface-grown carbon nanotubes*, Phys. Rev. A **79**, 043403 (2009).

[Pol08] C. A. Poland, R. Duffin, I. Kinloch, A. Maynard, W. A. H. Wallace, A. Seaton, V.i Stone, S. Brown, W. MacNee and K. Donaldson, *Carbon nanotubes introduced into the abdominal cavity of mice show asbestos-like pathogenicity in a pilot study*, Nat. Nanotechnol. **3**, 423 (2008).

[Pow93] E. A. Power and T. Thirunamachandran, *Casimir-Polder potential as an interaction between induced dipoles*, Phys. Rev. A **48**, 4761 (1993).

[Pre92] W. H. Press, B. P. Flannery, S. A. Teukolsky and W. T. Vetterling, *Numerical Recipes in C: The Art of Scientific Computing*, (Cambridge Univ. Press, 1992).

[Raa87] E. L. Raab, M. Prentiss, Alex Cable, Steven Chu and D. E. Pritchard, *Trapping of Neutral Sodium Atoms with Radiation Pressure*, Phys. Rev. Lett. **59**, 2631 (1987).

[Rei99] J. Reichel, W. Hänsel and T. W. Hänsch, *Atomic Micromanipulation with Magnetic Surface Traps*, Phys. Rev. Lett. **83**, 3398 (1999).

[Rek04] P. K. Rekdal, S. Scheel, P. L. Knight and E. A. Hinds, *Thermal spin flips in atom chips*, Phys. Rev. A **70**, 013811 (2004).

[Ren99] Z. F. Ren, Z. P. Huang, D. Z. Wang, J. G. Wen, J. W. Xu, J. H. Wang, L. E. Calvet, J. Chen, J. F. Klemic and M. A. Reed, *Growth of a single freestanding multiwall carbon nanotube on each nanonickel dot*, Appl. Phys. Lett. **75**, 1086 (1999).

[Ric95] L. Ricci, M. Weidemüller, T. Esslinger, A. Hemmerich, C. Zimmermann, V. Vuletic, W. König and T. W. Hänsch, *A compact grating-stabilized diode laser system for atomic physics*, Opt. Comm. **117**, 541 (1995).

[Ris05] T. Ristroph, A. Goodsell, J. A. Golovchenko and L. V. Hau, *Detection and Quantized Conductance of Neutral Atoms Near a Charged Carbon Nanotube*, Phys. Rev. Lett. **94**, 066102 (2005).

[Sal10] R. Salem, Y. Japha, J. Chabé, B. Hadad, M. Keil, K. A. Milton and R. Folman, *Nanowire atomchip traps for sub-micron atom-surface distances*, New J. Phys. **12**, 023039 (2010).

[Sch78] J. Schwinger, L. L. DeRaad and K. A. Milton, *Casimir Effect in Dielectrics*, Ann. Phys. **115**, 1 (1978).

[Sch99] S. Scheel, L. Knöll and D.-G. Welsch, *Spontaneous decay of an excited atom in an absorbing dielectric*, Phys. Rev. A **60**, 4094 (1999).

[Sch03] S. Schneider, A. Kasper, Ch. vom Hagen, M. Bartenstein, B. Engeser, T. Schumm, I. Bar-Joseph, R. Folman, L. Feenstra and J. Schmiedmayer, *Bose-Einstein condensation in a simple microtrap*, Phys. Rev. A **67**, 023612 (2003).

[Sch05] S. Scheel, P. K. Rekdal, P. L. Knight and E. A. Hinds, *Atomic spin decoherence near conducting and superconducting films*, Phys. Rev. A **72**, 042901 (2005).

[Sch08] S. Scheel and S. Y. Buhmann, *Macroscopic Quantum Electrodynamics -*

Concepts and Applications, Acta Physica Slovaca **58**, 675 (2008).

[Sch09] Stefan Scheel and Stefan Yoshi Buhmann, *Casimir-Polder forces on moving atoms*, Phys. Rev. A **80**, 042902 (2009).

[Shi75] A. Shih and V. A. Parsegian, *Van der Waals forces between heavy alkali atoms and gold surfaces: Comparison of measured and predicted values*, Phys. Rev. A **12**, 835 (1975).

[Sin99] S. B. Sinnott, R. Andrews, D. Qian, A. M. Rao, Z. Mao, E. C. Dickey and F. Derbyshire, *Model of carbon nanotube growth through chemical vapor deposition*, Chem. Phys. Lett. **315**, 25 (1999).

[Ste09] D. A. Steck, *Rubidium 87 D Line Data*, http://steck.us/alkalidata (2009).

[Sti10] A. Stibor, H. Bender, S. Kühnhold, J. Fortágh, C. Zimmermann and A. Günther, *Single-atom detection on a chip: from realization to application*, New J. Phys. **12**, 065034 (2010).

[Suk93] C. I. Sukenik, M. G. Boshier, D. Cho, V. Sandoghdar and E. A. Hinds, *Measurement of the Casimir-Polder force*, Phys. Rev. Lett. **70**, 560 (1993).

[Suk97] C. V. Sukumar and D. M. Brink, *Spin-flip transitions in a magnetic trap*, Phys. Rev. A **56**, 2451 (1997).

[Tau10] A. Tauschinsky, R. M. T. Thijssen, S. Whitlock, H. B. van Linden van den Heuvell and R. J. C. Spreeuw, *Spatially resolved excitation of Rydberg atoms and surface effects on an atom chip*, Phys. Rev. A **81**, 063411 (2010).

[Ven75] H. Venghaus, *Redetermination of the Dielectric Function of Graphite*, physica status solidi (b) **71**, 609 (1975).

[Ver84] B. J. Verhaar, J. P. H. W. van den Eijnde, M. A. J. Voermans and M. M. J. Schaffrath, *Scattering length and effective range in two dimensions: application to adsorbed hydrogen atoms*, J. Phys. A: Math. Gen. **17**, 595 (1984).

[Vet10] E. Vetsch, D. Reitz, G. Sagué, R. Schmidt, S. T. Dawkins and A. Rauschenbeutel, *Optical Interface Created by Laser-Cooled Atoms Trapped in the Evanescent Field Surrounding an Optical Nanofiber*, Phys. Rev. Lett. **104**, 203603 (2010).

[Vis10] G. Visanescu, *Working Title: Fabrication and Characterization of Vertically-Aligned Carbon Nanofibers*, PhD thesis Universität Tübingen 2010.

[Vog06] W. Vogel, D.-G. Welsch and S. Wallentowitz, *Quantum Optics*, (Wiley-VCH, 2006).

[Vul98] V. Vuletic, T. Fischer, M. Praeger, T. W. Hänsch and C. Zimmermann, *Microscopic Magnetic Quadrupole Trap for Neutral Atoms with Extreme Adiabatic Compression*, Phys. Rev. Lett. **80**, 1634 (1998).

[Wac05] A. Wachter and H. Hoeber, *Repetitorium Theoretische Physik*, (Springer

Press, 2005) 2nd edition.

[Wie76] C. Wieman and T. W. Hänsch, *Doppler-Free Laser Polarization Spectroscopy*, Phys. Rev. Lett. **36**, 1170 (1976).

[Wil06] S. Wildermuth, S. Hofferberth, I. Lesanovsky, S. Groth, P. Krüger, J. Schmiedmayer and I. Bar-Joseph, *Sensing electric and magnetic fields with Bose-Einstein condensates*, Applied Physics Letters **88**, 264103 (2006).

[Win84] W. H. Wing, *On neutral particle trapping in quasistatic electromagnetic fields*, Prog. Quantum Electron. **8**, 181 (1984).

[Wol04] E. L. Wolf, *Nanophysics and Nanotechnology: An Introduction to Modern Concepts in Nanoscience*, (Wiley-VCH, 2004).

[Zel35] Ya. B. Zeldovich, Zh. Eksp. Teor. Fiz. **5**, 22 (1935).

[Zha02] J. Zhao, J. Han and J. P. Lu, *Work functions of pristine and alkali-metal intercalated carbon nanotubes and bundles*, Phys. Rev. B **65**, 193401 (2002).

[Zip10] C. Zipkes, S. Palzer, C. Sias and M. Köhl, *A trapped single ion inside a Bose-Einstein condensate*, Nature **464**, 388 (2010).

Acknowledgements

I would like to thank all people who supported me during my time as a doctoral student and who contributed to the successful completion of this thesis. In particular, I like to express my gratitude to the following people:

In the first place, I would very much like to thank Prof. Dr. József Fortágh who initiated the nanotube experiment and who continues to successfully lead the project. Thanks to the generous funding, getting any desired equipment for the lab was never a problem. And thanks to his scientific guidance and experience, all the electronics and optics could finally be put together to make the experiments presented in this thesis.

In addition, I am very grateful to Dr. Andreas Günther, who also supervises the nanotube project. His vast experience in the lab, in particular concerning the carrier chip that he developed, was a great help. Moreover, he was a valuable partner for discussions about the underlying physics of many measured phenomena, in particular, the ultracold scattering. Furthermore, I am grateful for his support in many details of the data evaluation and for critically reviewing my work.

Prof. Dr. Thomas Judd helped me in many different respects: Discussions of the physics of surface gauging, Casimir-Polder forces, and BEC scattering were very insightful and helped me to better understand the experimental findings. Moreover, his simulations contributed much to comprehend what was going on in the measurements. Finally, I owe him a lot for his persistence in proof-reading the present thesis.

In my entire time as a PhD student, I shared the lab with Michael Gierling. This was a very pleasant and productive cooperation, in particular I value his direct and effective approach to solve problems. I am particularly grateful that we endured the nerve-racking problems and setbacks of the (nano)chip assembly together. Moreover, I am very happy that he volunteered the entire time to work the early shifts. In addition, I would like to thank Hannah Schefzyk and Saskia Kühnhold for their good cooperation while they did their diploma thesis on the nano-setup. Furthermore, I would like to thank our very talented and motivated (former) Hiwi students.

I am also very grateful to Gabriela Visanescu for having managed the challenging production of the nanochips and for the uncountable SEM pictures she took to characterize the samples. She luckily also kept going after I destroyed one of her best samples while mounting. Moreover, I thank Prof. Dr. Dieter Kern and, in particular, his co-workers Michael Häffner and Peter Federsel for their great support

in the nanochip production.

The mechanics workshop of Mr. Brodbeck, Mr. Stockmaier, and co-workers as well as the colleagues from the electronics workshop around Mr. Schreyer were an invaluable support for the experiment. Without their professional help, experiments would probably not have been made until the present day.

I also thank all my colleagues from D5 for uncountable practical tips in the lab, many stimulating discussions and, in general, the good atmosphere. I am particularly grateful to my (former) office mates Daniel Cano, Brian Kasch, Florian Jessen and Florian Karlewski who were always valuable partners for discussions.

Finally, I would like to express my particular gratitude to my family and my friends who supported me not only in the time of my PhD but throughout my entire studies.